EÖTVÖS LORÁND UNIVERSITY
FACULTY OF SCIENCES

Origin and formation of carbonate minerals related to natural CO_2 occurrences

by

Dóra Magdolna Cseresznyés

Ph.D. thesis

DOI: 10.15476/ELTE.2023.042

Ph.D. program for Environmental Earth Sciences at Doctoral School of Environmental Sciences, Faculty of Science, Eötvös Loránd University

Head of the doctorate school: Tamás Turányi, D.Sc.
Program director: Zoltán Szalai, Ph.D.

Supervisors

György Falus, Ph.D.
head of division

Division of Geology
Directorate of Geology
Supervisory Authority for Regulatory Affairs

György Czuppon, Ph. D.
senior research fellow

Institute for Geological and Geochemical Research,
Research Centre for Astronomy and Earth Sciences,
Eötvös Loránd Research Network

Consultants

Csaba Szabó, Ph.D.
associate professor

Lithosphere Fluid Research Lab,
Eötvös Loránd University

Csilla Király, Ph. D.
research fellow

Geographical Institute,
Research Centre for Astronomy and Earth Sciences,
Eötvös Loránd Research Network

Budapest
2023

Content

Figures

Tables

1. Introduction and aims

The constant increase in the atmospheric carbon-dioxide (CO_2) concentrations, related to anthropogenic emissions, gains special importance with respect to global climate change. 'Carbon-dioxide capture and storage' (CCS) is widely believed to be capable of attenuating the effect of human CO_2 emissions, while relying on fossil fuels for energy production until alternative sources of energy are developed (IPCC, 2005; 2022).

Mineral storage of carbon-dioxide is one of the most promising ways of storing CO_2 safely underground. Several different host rocks such as basalts and ultramafic rocks (Matter et al., 2016; Pogge von Strandmann et al., 2019; Snæbjörnsdóttir et al., 2020), sandstones (Worden, 2006) and carbonates (Stevens and Tye, 2007) have been studied for this purpose. Although these results may be adapted to the long-term storage of CO_2, upscaling of these experiments to the industrial level (Gt CO_2 injection/annum) faces difficulties. The study of natural CO_2 reservoirs helps to understand and predict what processes are likely to take place when storing anthropogenic CO_2 underground over geological times (e.g., Baker et al., 1995; Forray et al., 2021; Gao et al., 2009; Gilfillan et al., 2009; Király et al., 2016a; Pearce et al., 1996; Qu et al., 2022). When a large amount of CO_2 floods a sandstone reservoir, the dynamic equilibrium between porewater and rocks is likely to be shifted. Firstly, CO_2 will be trapped in the pores via structural trapping then it will dissolve in the porewater (solubility trapping) (Bachu et al., 2007; Bickle et al., 2013; Oelkers et al., 2008), which will cause the drop of the reservoir fluid pH. As a result, carbonates and alumosilicates will start dissolving, other carbonates and clay minerals will (re)precipitate. Most laboratory experiments (e.g., Cheng et al., 2022; Hellevang et al, 2005) and geochemical models on sandstone reservoirs and CO_2 injection fields predict precipitation of common carbonate minerals (e.g., calcite, dolomite, siderite, magnesite) as well as the formation of a rare carbonate, dawsonite [$NaAlCO_3(OH)_2$] (e.g., Gaus et al., 2005; Lu et al., 2022; Szabó et al., 2016; Xu et al., 2003, 2005). Dawsonite is believed to be one of the carbon-dioxide "incorporating" minerals in CCS, therefore it is necessary to understand its stability, precipitation and dissolution in the reservoirs over time.

Dawsonite mainly crystallizes as a result of high partial pressure of CO_2. It is widespread in deep saline or sedimentary reservoirs naturally flooded by CO_2, which generally has magmatic origin (e.g., Baker et al., 1995; Cseresznyés et al., 2021; Gao et

al., 2009; Király et al., 2016a; Liu et al., 2011; Li and Li, 2017; Worden, 2006; Yu et al., 2014; Zhao et al., 2018; Zhou et al., 2014). Additionally, dawsonite can also be found in other geological environments, i.e., in coal (Loughnan and See, 1967), oil shale (Ming et al., 2017), volcanoclastic rock (Comerio et al., 2014), vitric tuff (Zalba et al., 2011) and in zeolitic weathered soil profile (Hay, 1966) as well. It can also appear in fluid (e.g., Aradi et al., 2019; Coveney and Kelly, 1971) and melt inclusions (Fei and Liu, 2022), and rarely in surface occurrences as well (e.g., Smith and Milton, 1966). Despite its relatively large abundance in the subsurface environment, dawsonite appears on the surface only in a few localities e.g., USA (Smith and Milton, 1966), Japan (Aikawa, 1972) and Argentina (Zalba et al., 2011).

Stable isotope geochemistry of C and O in carbonate minerals has been widely used to determine the origin of fluids. Most of the studies related to CCS used the carbonate stable isotope composition inferred from the bulk rock measurements (e.g. Liu et al., 2011; Zhao et al., 2018) to evaluate the processes that take place both in natural CO_2 reservoirs (Baker et al., 1995; Gao et al., 2009; Liu et al., 2011; Zhao et al., 2018) and during CO_2 injections (Higgs et al., 2015; Stevens and Tye, 2007; Worden, 2006).

The main aim of this research was to shed light on the formation process of carbon-dioxide fixing minerals, and to develop a protocol that can clearly distinguish between carbonates that are related to diagenesis from those who's formation is related to CO_2-floodingand to determine the origin of the formation fluid of the latter. In order to achieve these goals three different areas, two from deep saline reservoirs in the Little Hungarian Plain (Ölbő, Mihályi-Répcelak fields, Hungary) and one from a surface occurrence in the Eastern Carpathians (Covasna, Transylvania, Romania) were studied. The common feature of these localities is the natural presence of large amount of CO_2.

To reveal the precipitation properties and environments of dawsonite (and other cogenetic carbonates), beside detailed petrographic and geochemical studies, stable isotope analyses were conducted. To understand the meaning of the stable isotope data of carbonates, experimental work was also carried out in this study. Additionally, to carbon and oxygen isotopes, hydrogen isotope composition of dawsonite was measured for the first time worldwide. This might be a new promising tool, which helps to constrain the conditions of the dawsonite formation.

Finally, to better understand the chemical processes, taking place during a CO_2 injection project, geochemical modelling was also applied. The novelty in the modelling part of the thesis is that it could be validated with data acquired from natural rock samples.

The sandstone samples, which were not flooded naturally by CO_2 (Ölbő) were used as initial starting material, which represent the stage before CO_2 injection in the rock. The well-known and already described sandstones of Mihályi-Répcelak represented the final stage, millions of years after CO_2 flooded the reservoir. Hence, the dissolution and precipitation of minerals in the modelling results could be validated.

2. Geological background of natural CO_2 occurrences

Three areas, where large amount of CO_2 is naturally present, were selected for this work: 1) Mihályi-Répcelak area is well-known as a natural CO_2 occurrence in the Little Hungarian Plain (Hungary) where the CO_2 trapped (and is produced nowadays) in a sandstone formation. 2) Ölbő area, located close to the Mihályi-Répcelak field, where CO_2 is produced from Miocene limestone reservoir. However, in this study the focus is not on the limestone reservoir, it is on the overlying sandstone formation, identical to those, which contain CO_2 in the Mihályi-Répcelak area. The third area is found in Covasna along a creek of Hankó Valley (Eastern Carpathians) and it is well-known of the continuous CO_2 emanations (CO_2 mofettas) and the occurrence of rare mineral assemblages.

2.1. Mihályi-Répcelak and Ölbő areas

The Mihályi-Répcelak and Ölbő areas are located in Central Europe (Fig. 1A), in the western part of the Pannonian Basin (Hungary; Fig. 1B). The study site is on the Mihályi-high, bordered by the Csapod Trough from the west, and the Rába tectonic line from the east (Fig. 1C). Mihályi, Répcelak and Ölbő sites are located ~20-27 km far from each other (Fig. 1C).

Carbon-dioxide at the Mihályi-high has been explored since 1930s with various geophysical (both gravity and seismic) methods, but the detailed examination of natural gas reserves started only in the 1960s (Mészáros et al., 1979; Kőrössy, 1987; Palkó and Deák, 1974). The Mihályi-Répcelak fields consist of 26 CO_2 reservoirs in Alföldi and Dunántúli Formation Group (earlier named as Lower and Upper Pannonian) sediments (Late Miocene; Szamosfalvi, 2014). The Pannonian sandstone bodies are interbedded with clayey/siltstone layers that have prevented CO_2 migration to the surface (Király et al., 2016b and references therein). Conglomerate bodies also stratigraphically underlay these CO_2-flooded sandstone reservoirs (Forray et al., 2021). The studied CO_2 reservoirs in Mihályi are found at ~1200-1650 m depth, meanwhile the Répcelak reservoirs are

around ~1150-1450 m deep. The hydraulic connection of the two parts (Mihályi and Répcelak) is still under debate (Palcsu et al., 2014). The gas naturally present in the CO_2 reservoirs consists of 95 v/v% CO_2, 1.3 v/v% nitrogen and 3.3 v/v% hydrocarbons (Mészáros et al. 1979).

The Ölbő area was also flooded by large amount of CO_2, however, it trapped here mostly in the Middle Miocene (Serravallian-Upper Badenian) *Lithothamnium*-bearing limestone at ~1700-1900 m depth. Only minor part of the CO_2 is trapped in the Paleozoic metamorphites underlying the limestones. These two lithologic formations (limestone and metamorphites) form a single CO_2 reservoir. The natural gas found in Ölbő consists of 96.2 v/v% CO_2, 1.3 v/v% nitrogen and 2.4 v/v% hydrocarbons (Selmeczi, 2018), similar in composition to Mihályi-Répcelak gas. The Sarmatian clay marl overlying the limestone likely is acting as impermeable caprocks in Ölbő (Palkó and Deák, 1974). In addition, this clay marl sequence is also preventing the sandstones located in higher stratigraphic level (~1490-1690 m depth) to be flooded by CO_2. Indeed, sandstones of both Alföldi and Dunántúli Formation Group are gas-free in the Ölbő area. The sandstone of the Alföldi Formation Group is the same formation as the CO_2 reservoirs located in Mihályi-Répcelak area. Thus, the Ölbő area gives an excellent opportunity to study the same sandstone formation, which was not flooded naturally by large amount of CO_2, and compare with the flooded one in Mihályi-Répcelak area to better understand the potential chemical processes (e.g., mineral dissolution and precipitation) in a sandstone reservoir before CO_2 injection and after millions of years of interaction with CO_2.

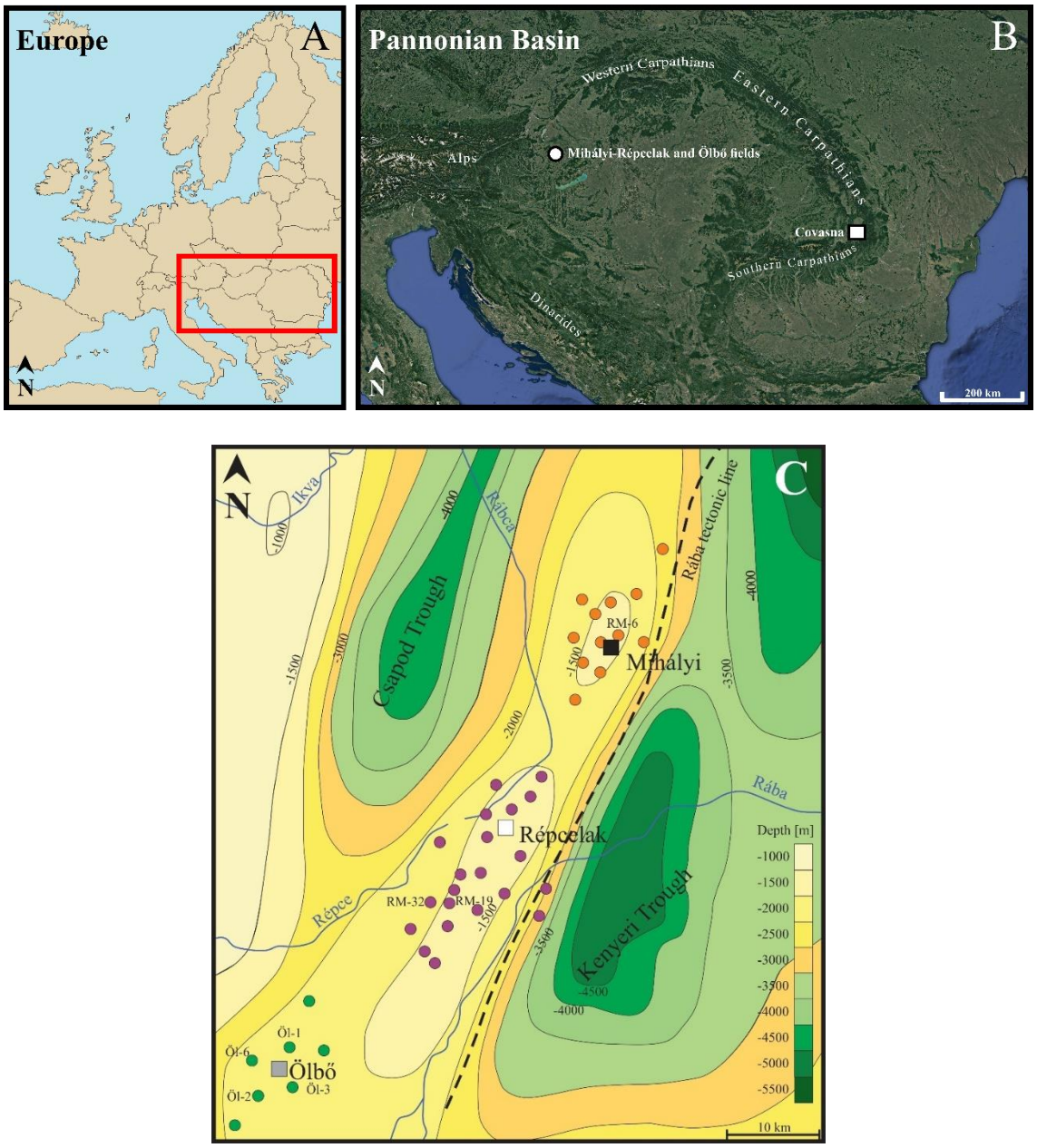

Fig. 1: Location of the study areas in Europe (A), in the Pannonian Basin (B), and the Mihályi-Répcelak and Ölbő fields showing the studied boreholes (Mihályi: RM6, Répcelak: RM-32, RM-19, Ölbő: Öl-1, Öl-2, Öl-3, Öl-6) in the area (C). The pre-Cenozoic depth contour map (C) was redrawn after Zilahi-Sebes (2013).

2.1.1. Evolution of the Little Hungarian Plain

The Pannonian Basin is filled up mostly by Neogene sediments, covering the basement rocks of the ALCAPA (from the Africa-microplate) and the Tisza-Dacia units (from the Eurasia-microplate) (Csontos et al., 1992). The basement of the Little Hungarian Plain is built up by medium grade metapelites, originated from the Lower Austroalpine nappes, and low grade metapelites of the Upper Austroalpine nappe units (Tari and Horváth, 2010). These are called as the “Rábamenti” Metamorphites, which

compose the Mihályi-high (+1000-1200 m elevation from the basement level) in the NE-SW direction in the Little Hungarian Plain (Fülöp, 1990). The basement is built up by Devonian para-metamorphic and sedimentary rocks with high carbonate contents. The Lower Devonian formations consist of dolomitic chlorite shale, coarse-grained sandstone shale lenses, sericite shale and limestone (Palkó and Deák 1964). The upper parts of the Devonian are represented by dolomite.

During the Alpine orogenic cycle, the emerging Eurasian Mountain range divided the Tethys Ocean. As a consequence, the Paratethys was formed and as a sub-basin, the Pannonian Basin was developed (Nagymarosy and Müller, 1988; Sacchi and Horváth, 2002). During the Oligocene and the Early Miocene, the Paratethys had connection periodically with the world ocean, therefore formation of marine sediments characterized the whole Pannonian Basin. In the Little Hungarian Plain during the Karpatian (Early-Middle Miocene, Burdigalian-Langhian), fine-grained sediments were deposited in the middle of the basin, meanwhile terrestrial and alluvial coarse-grained detrital rocks were typically deposited on the margins of the basin (Hámor, 1995; Nagymarosy and Hámor, 2012). Fine-grained sediments accumulated during the Early Badenian (Middle Miocene, Langhian-Serravallian) in the Karpatian grabens, furthermore abrasion-derived basal conglomerates formed close to the coastal zones. Due to the sea level rise during the Late Badenian, Badenian sediments form the largest marine formations in the Little Hungarian Plain (Kovaĉ et al., 2007). The Badenian Leitha limestone represents a reef facies in the peripheral zone, which is distributed on the western and eastern part of the basin edges and on the Mihályi-high (Kovaĉ et al., 2007). Among the marine sediments, tuff layers occur, which are present in the Pásztori, Szany and Tét volcanic areas (Balázs and Nusszer, 1987). The Badenian formations vary in thickness and are extremely heterogeneous lithologically. Based on the variable but small thickness of the Badenian sediments, an uneven, slow subsidence was proposed. This tendency prevailed during the following geological ages as well (Palkó and Deák 1964).

The Sarmatian formations (Middle-Late Miocene, Serravallian-Tortonian) formed in a low/reduced-salinity water environment compared to the normal salinity waters of the Badenian. In the shallow coastal regions, the formation of carbonates and calcareous sands continued, whereas in the deeper part of the basin a marl sequence formed. Based on the evolution of the basin, the Mihályi-high unroofed before the sediments of the Alföldi Formation Group were formed, therefore the erosion affected these sediments (Mészáros et al., 1979). By the end of the Sarmatian (Upper Serravallian-Lower

Tortonian), the basin lost direct connectivity to the world seas, consequently the Pannonian Lake formed. The salinity of the Pannonian Lake started to decrease, and a new endemic fauna developed (Magyar et al., 1999).

During the continuous uplift and erosion of the surrounding Alpine-Carpathian Mountain belts, significant amount of sediments were transported to the basin by the high-yielding rivers from NW direction (Pogácsás, 1984; Vakarcs et al., 1994; Juhász, 1994, 1998; Magyar et al., 1999, 2013). Since the deposition rate exceeded the space created by the thermal subsidence of the basin, the Pannonian Lake started to be filled up by a prograding delta system. This prograding delta system formed a several kilometers thick fluvial sedimentary sequence from the Sarmatian (Juhász, 1992). The rate of the deposition was extremely fast: the first shelf-margin slope appeared in the Little Hungarian Plain nearly 10 million years ago and in the following 1 million years the basin was filled up completely (Magyar et al., 2013).

The Alföldi Formation Group sequence is characterized by alternating marl and clay marl sediments (Endrőd Formation), which is followed by a turbiditic sandstone (Szolnok Formation) and by siltstone layers (Algyő Formation) with sandstone interbeddings (Szamosfalvi, 2014). The Dunántúli Formation Group sequences composed of alternating siltstone, sandstone, and claystone (Újfalu and Zagyva Formations) (Mészáros et al., 1979).

Based on petrologic and geochemical studies, two phases of volcanic activity occurred in the vicinity of the study area, along the Rába tectonic line (Kőrössy, 1987): the Pásztori volcano (12-10 Ma) and the Kemenesalja volcanoes (6 Ma) (Harangi et al., 1995; Jugovics, 1970; Tari, 1994). According to the K/Ar and $^{40}Ar/^{39}Ar$ ages, the Kemenesalja volcanoes formed between 5.5. to 4.2 Ma (Balogh et al. 1982, 1986; Wijbrans et al., 2007).

2.1.2. Petrography of the studied rock formation

The Mihályi-Répcelak caprock, reservoir and conglomerate samples were described by Király et al. (2016b, 2017) and Forray et al. (2021). Dawsonite in Mihályi-Répcelak area occurs in the clayey caprock and in the sandstone reservoir. Additionally, dawsonite appears also in kaolinitic clasts of conglomerates in Mihályi-Répcelak, but its appearance is limited compared to the overlying sandstones (Forray et al., 2021). The samples contain 72-74 v/v% quartz (Q), 2-6 v/v% feldspar (F) and 15-25 v/v% lithoclast (L). Based on the McBride (1963) QFL classification the samples are sublitharenites. One

of the most spectacular petrographic features of the sandstone is its complex carbonate association such as calcite, dawsonite, dolomite, ankerite and siderite. In the samples where dawsonite is present around 8-16 m/m% (Table 1), the ankerite rims occur in two generations. The generations differ in their Fe+Mn contents with ~10 m/m% and ~18 m/m%, respectively (Fig. 2 A-B). Late generation ankerite can be found along the cracks of the early ankerite and dolomite (Fig. 2A). Based on the petrographic observations, dawsonite and late generation of ankerite (i.e., the outer rims) are in close textural relationship (Fig. 2C). Calcite grains (RM6-7R1, RM6-7R2, RM6-7R3, RM32-5R2) are rare and occur in the pores of the sandstones and often show signs of dissolution (Fig. 2D). Siderite appears as a pore filling, fine grained carbonate and as a pseudomorph of silicates (probably biotite, Fig. 2B). Siderite also appears in iron rich clayey clast (RM6-7R3) and as thin layers in ~200 μm patches in the dawsonite-bearing sandstones (RM6-9R, Fig. 2C) (Cseresznyés et al., 2021). Siderite can also intermix with fibrous dawsonite (Fig. 2D). Only sample of RM32-5R2 does not contain siderite (Table 1). Dawsonite occurs as a fibrous, pore filling mineral. Dawsonite is present in close textural relation with ankerite, kaolinite and quartz overgrowths (Fig. 2E). Dawsonite is replacing the partially dissolved albite (Fig. 2F).

Table 1. Mineral composition of dawsonite-bearing sandstones. Ankerite+siderite is redefined with per point counting (Király, 2017). Values are expressed in m/m%. 1 sigma uncertainty is 1 %. ND: not detected. *sample does not contain siderite.

Area	Sample	Calcite	Dawsonite	Dolomite	Ankerite + Siderite	Quartz	Muscovite +Illite	Kaolinite	K-feldspar
Mihályi	RM6-9R	ND	16	7	21	36	15	3	2
	RM6-7R3	8	4	9	13	43	15	7	1
	RM6-7R2	8	3	6	15	43	16	6	3
	RM6-7R1	10	3	11	10	42	14	9	1
Répcelak	RM32-5R2	<1	8	8	27*	45	8	3	1
	RM19-6R	ND	3	10	9	52	12	12	2

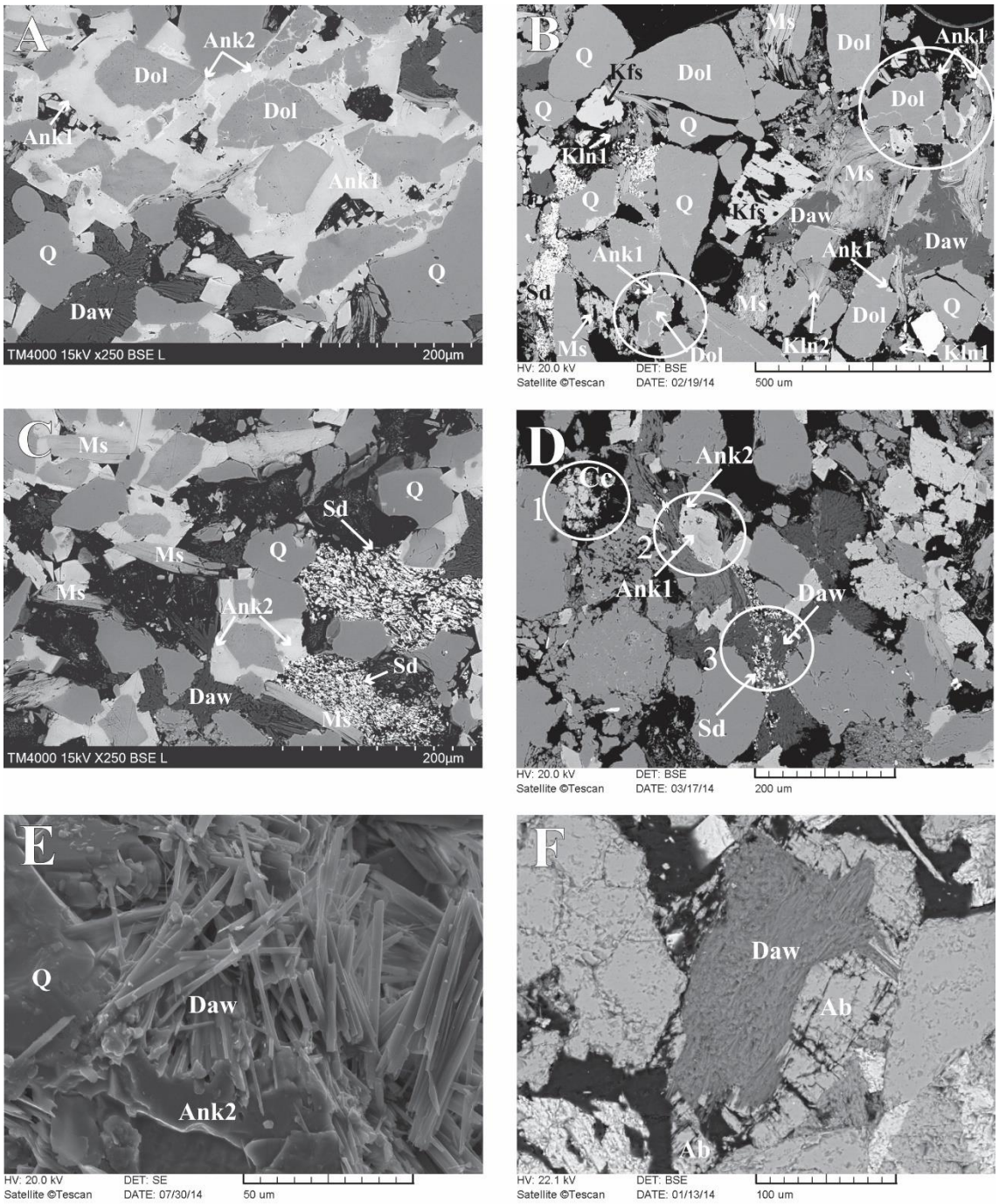

Fig. 2. Backscattered (A-D and F) and secondary (E) electron images of dawsonite-bearing sandstones from the Mihályi-Répcelak area (Cseresznyés et al., 2021; Király, 2017). A: Ankerite is present in two-generation rims Ank1 (early) and Ank2 (late) around dolomite (Dol). B: Ank1 shows rudimentary features on dolomite. C: Ank2 in close textural relation with dawsonite (Daw), siderite (Sd) forms large patches. D: Area-1 indicates dissolution of calcite (Cc). Area-2 shows the relationship of early (Ank1) and late (Ank2) as generations of zoned ankerite cement. Area-3 shows the textural relationships of simultaneously forming siderite (Sd) and dawsonite (Daw). E: Assemblage of dawsonite (Daw), quartz (Q) and ankerite (Ank2), suggesting coeval formation. F: Albite (Ab) dissolution and dawsonite (Daw) precipitation. Abbreviations: Ank1: ankerite with low Fe + Mn content, Ank2: ankerite with high Fe + Mn content, Daw: dawsonite, Dol: dolomite, Sd: siderite, Ab: albite, Kfs: K-feldspar, Kln1: early generation of kaolinite, Kln2: late generation of kaolinite, Ms: muscovite, Q: quartz.

In the area of Ölbő, Neogene formations are located directly above the Devonian formation (Palkó and Deák 1964). Most of the Miocene formations consist of the sediments of the Badenian, which is mainly composed of *Lithothamnium*-bearing limestone and calcareous marl (Palkó and Deák 1964). Above the Badenian, the Sarmatian clay marl is present, but only scarcely due to the destructive effect of uneven subsidence or erosion (Palkó and Deák 1964). The Alföldi Formation Group is characterized by the varying marl, fined-grained clay marl and sandstone. The Upper Pannonian consists of siltstone, sandstone, and claystone layers. The Ölbő area was mainly investigated for hydrocarbon production purposes, therefore the detailed petrography of the investigated Ölbő samples is not available. This work fills this *hiatus* especially focusing on the same sandstone formation, which can be found in Mihály-Répcelak area.

2.1.3. Origin of gases

The basin of the Little Hungarian Plain entered the oil window during the Late Miocene (8-7 Ma), oil traces and gas (mostly CH_4) accummulations have been found in the area (Mészáros et al., 1979). The genetic link between oil and CH_4 has been established by stable isotope study (Koncz and Etler, 1994). A mixture of CH_4-N_2 migrated to the Pannonian Formations from the Silurian metasediments (Csizmeg et al., 2012; Vető et al., 2014). Most of the CH_4 has been exploited for industrial purposes and the reserves were considered as depleted (Vető et al., 2014). According to recent research (Palcsu et al., 2014, Vető et al., 2014), the CO_2 inflow occurred during the Late Miocen/Early Pliocene in Mihályi-Répcelak.

The origin of the accumulated CO_2 in the Mihályi-Répcelak area has been a matter of debate. Koncz (1983) assumed metamorphic or volcanic/magmatic origin for CO_2 based on measured $\delta^{13}C_{CO2}$ values (range between –7.0 ‰ and –4.0 ‰). Cornides et al. (1986) measured carbon and helium isotope ratios ($\delta^{13}C_{CO2}$ = -6.5 ‰ to -5.2 ‰, $^3He/^4He_{max}$ = 3.93 R_A, where R_A is the atmospheric ratio of 1.399 x 10^{-6}, Mamyrin et al., 1970). It was suggested that the CO_2 probably has mantle origin, which is in line with typical magmatic derived isotopic ratio ranges (-8 ‰ - -4 ‰) (Ohmoto and Rye, 1979; Györe et al., 2015). Additionally, the CO_2 measurements of Nádor (2002) ($\delta^{13}C_{CO2}$ = -5.5 - -3.1 ‰) also agree with this assumption.

A comprehensive stable and noble gas isotope study from the Mihályi-Répcelak field also confirmed that most of the CO_2 has mantle origin (Palcsu et al., 2014). In

addition, the observed $\delta^{13}C_{CO2}$ values agree well with those proposed for the European Subcontinental Lithospheric Mantle (SCLM) (– 3.9 ‰ - –2.1 ‰) (Weinlich et al., 1999). Palcsu et al. (2014) and Vető et al. (2014) concluded that the CO_2 originates from degassing melts ascending from the asthenosphere. The CO_2 probably migrated along the Rába tectonic line towards the Mihályi-Répcelak area, where it has accumulated in the Pannonian sediments (Kőrössy, 1987).

The latest study (Györe et al., 2022) in the area raised the possibility of different sources for the CO_2 in the Mihályi and Répcelak counterparts. Based on noble gas analysis, $^{20}Ne/^{22}Ne$ and $^{21}Ne/^{22}Ne$ ratios show that gas in the Répcelak exhibits a mixing between air derived gases and magmatic gases trapped in the crust, consistent with the proposed Miocene age of the CO_2. In contrast, these neon isotope measurements of Mihályi gases lie on the air-European SCLM mixing line showing a complete lack of nucleogenic or crust components (Györe et al., 2022). This finding suggests a direct mixing between magmatic and air derived gases in case of Mihályi and indicates significantly younger age (Györe et al., 2022). In case of Ölbő, the CO_2 field is entirely separated from the Mihályi-Répcelak occurrence both from geographic and probably in hydraulic points of view. The origin of CO_2 in Ölbő has not been studied before.

2.2. Covasna - Eastern Carpathians

Area of Covasna is located in the boundary of Târgu Secuiesc Basin and outer Moldavides, Eastern Carpathians (Fig. 1). The study area is composed of three Carpathian nappes: Tarcău, Macla-Zagon and Audia nappes which are partly covered by different fluvial deposits (Fig. 3A). The Tarcău nappe outcrops in Covasna (Melinte-Dobrinescu et al., 2011). The area lies on a complex fault system where two large faults appear in NE-SW and SE-NW directions (Fig. 3A; Dumitrescu et al., 1970).

Two main tectonic events affected the Carpathian Bend in the Pliocene-Quaternary: slab-pull, steepening of the Vrancea slab and upwelling in the asthenosphere; and inversion tectonics (Matenco et al., 2007; Seghedi et al., 2011). During the inversion (from the late Pliocene), as a result of asthenospheric upwelling Na-alkalic magma rose to the surface, most likely along crustal faults (Seghedi et al., 2011).

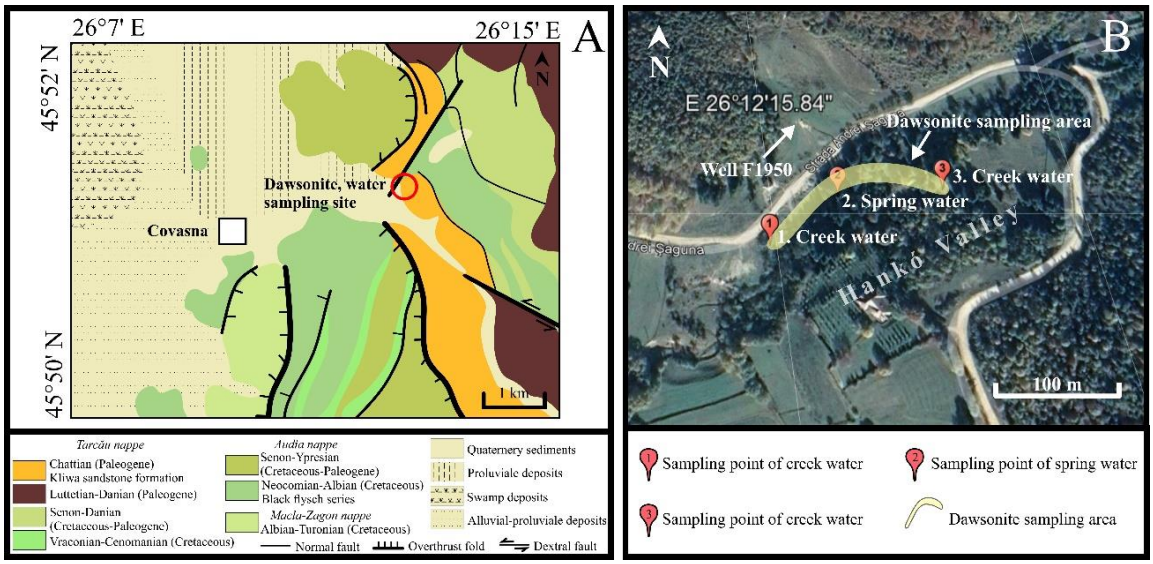

Fig. 3. Geological map of Covasna (A), dawsonite and water sampling points (B).

The area of the Târgu Secuiesc Basin and the Eastern Carpathians is well-known for its CO_2 emanations (mofettes) and thousands of CO_2-rich mineral water springs (Szakács, 2010). The CO_2 emanations in the Eastern Carpathians (from the Kelemen until Harghita) are likely related to the Neogene volcanic and seismic activity in the region (Incze et al., 2016) and is assumed as post-volcanic activity (Szakács, 2010). In contrast, the springs found in the Târgu Secuiesc Basin are linked to metamorphic reaction (Vaselli et al., 2002). In the centre of Covasna, a 'mud volcano or bath' called Balta Dracului (Devil's Pond) erupted several times in the past (noted from 1837), the last recorded eruption was in 1984 (Dénes, 2005; Pálfy, 1905; Róth, 2001; Wanek 2006). These eruptions are still active in the Covasna area, a CO_2-rich water eruption was recently observed in the Hankó Valley in 2019 by Lange et al. (2022). The CO_2-rich water erupted from an uncovered old well (F1950, drilled in 1950, Georgescu et al., 1978) close to the creek of Hankó Valley (Fig 3B), in irregular intervals.

In the study area the Tarcău nappe (Kliwa sandstone formation) and the Audia nappe (Black flysch) meet along the NE-SW directed fault (Fig. 3A) and outcrop mainly the Cretaceous and Paleogene flysch (Néda et al., 2008). Bitumenous shale also appears in the flysch (Wanek, 2000). Gas emanations caused extensive mineral formation in the Audia Beds of the Internal Flysch areas. These emanations can be connected to the deep fractures related to the Neogene-Quaternary volcanic rocks of the region (Laczkó et al., 2007). As a result of the intensive gas emanation in the studied area (Hankó Valley, Covasna), carbonates, sulphides and sulphates were observed in the rocks of the Audia-nappe (marls, sandstones, breccias) along the creek of Hankó Valley (Laczkó et al., 2007).

The creek of Hankó Valley reveals a calcite-aragonite-orpiment-realgar-pyrite-marcasite mineral association in the fine-grained black flysch (sandstones, breccias) of the Audia nappe, which is characteristic for the whole area (Hauer 1860; Koch 1885, Bányai 1933, Dénes et al. 2005; Papucs, 2000). Hauer (1860) and Bányai (1957) described sulphur in the carbonate deposits of spring water. Arsenic sulphide assemblages (mostly realgar) are cropping out in the sedimentary formations of the flysch belt as a result of low temperature, post-volcanic activity (Kristály et al., 2006). Pararealgar, pharmacolite and arsenolite were also determined and described as an alteration product of realgar (Kristály et al., 2006). Orpiment was mentioned together with realgar, aragonite and calcite (Koch, 1885; Bányai 1957), but after the re-investigation of the area, Kristály et al. (2006) concluded that the orange and red phases are realgar and pararealgar, and orpiment is not a common mineral in the area. Carbonates (i.e., aragonite, calcite and siderite) are characteristic for spring-water deposits, which usually occur in the flysch zone (Bielz, 1889; Jakab 1998). Papucs (2000) described an additional carbonate mineral, dawsonite [$NaAlCO_3(OH)_2$] along the creek of Hankó Valley, which was the first documented occurrence of dawsonite in the Eastern Carpathian region. Dawsonite was described as white powdery or fine fibrous aggregates with silky lustre in the cracks of the sandstones (Papucs, 2000).

The genesis of the mineral assemblage is still under debate, hydrothermal activity, recent precipitation from the creek post-volcanic fluid migration along tectonic lines were all proposed (Dénes et al., 2005). As a source for arsenic and sulphur, the underlying Cretaceous-Paleogene flysch sequence was suggested (Dénes et al., 2005). Based on recent results of the mineral deposits of Covasna (Kristály et al., 2006), Papucs (2016) reconsidered the mineral association and distinguished marcasite-pyrite and aragonite-calcite-realgar-pararealgar-pharmacolite associations. According to Papucs (2004), the formation of the mineral association is related to the Neogene volcanism assuming that the precipitation of the arsenic minerals in Hankó Valley could be a process of the fumarole activity (Dénes et al., 2005; Papucs, 2004).

3. Determination of stable C and O isotopes of carbonates – Sequential acid extraction (SAE) method

Carbonates in geological systems are very sensitive to the presence and partial pressure of CO_2. To understand the carbonate dissolution and crystallization processes in a rock formation with complex carbonate mineralogy, requires precise determination of carbonates stable isotope composition, being a sensitive measure of formation conditions. Moreover, most of the CCS related studies invoked isotope techniques, like sequential acid extraction (SAE) method to reveal the origin of fluids during carbonate formation (e.g., Baker et al., 1995; Gao et al., 2009; Liu et al., 2011). This is crucial, especially for dawsonite formation which is reported in several basins worldwide in different geological systems (Table S1). The Mihályi-Répcelak and Ölbő sandstone samples contain various carbonates such as calcite, dawsonite, dolomite, ankerite and siderite; therefore, the method proposed to analyse these kind of samples for stable isotopes are crucial. However, the stable carbon and oxygen isotope analysis of carbonate minerals are not straightforward when the different carbonates cannot be physically separated. To minimize potential cross-contamination, selective acid extraction method is often utilized to determine the isotopic composition of the samples with multiple carbonates in them (Al-Aasm et al., 1990; Epstein et al, 1964).

The above mentioned CCS related studies used phosphoric acid to dissolve carbonate minerals for isotopic analysis according to McCrea (1950). Al-Aasm et al. (1990) published a SAE method to determine the stable isotope composition of samples containing multiple carbonate phases. Al-Aasm et al. (1990) used pure calcite, dolomite, siderite, and magnesite, which were dissolved in 100 % phosphoric acid at 25 °C and 50 °C. For the pure minerals at 25 °C, 2 h reaction time was determined for calcite, 24 h dissolution time for dolomite, at 50 °C 4 h was enough for dolomite, and 72 h reaction time was needed for siderite. Baker et al. (1995) reacted dawsonite with 100 % orthophosphoric acid at 25 °C for 24 h to extract CO_2 for C and O isotope analysis. They suggest based on the work of Boussaroque et al. (1975), that this technique allows to measure the isotopic composition of the CO_3^{2-} of dawsonite, without interference from the OH^- in it.

Liu et al. (2011) reacted whole sandstone samples (containing calcite, dawsonite, ankerite) with 100 % orthophosphoric acid at 25 °C for 6 h, 24 h and 48 h to extract the CO_2 from carbonates for carbon and oxygen isotope analysis. 6 h reaction time was used

for calcite, 24 h dissolution time was applied for dawsonite (based on Baker et al., 1995) and 48 h for ankerite.

Csereszny és (2018) carried out experiments on pure carbonates: calcite (international standard provided by Merck KGaA), dawsonite (separated from the RM6-9R sample, Mihályi, Hungary), dolomite (Bükfürdő, Hungary), ankerite (Dobsina, Slovakia) and siderite (Bírótelek, Hungary) to verify the suitability of above-described methods in case of a complex carbonate assemblage. The minerals were dissolved in 100 % orthophosphoric acid at 25 °C for 1, 6, 24 and 48 hours. In case of siderite, 70 °C and 24-, 48-, 96- and 144-hours dissolution time was applied. The assumption was that the orthophosphoric acid starts to dissolve all carbonate minerals at some rate in the sandstone sample and the isotopic composition of the yielded CO_2 is not representative for only one mineral. Following on these experiences, the new experiments were carried out in this study to achieve more detailed picture applying different reaction times (see in the Result and Discussion).

4. Samples

The investigated samples derived from drilling cores from Mihályi-Répcelak and Ölbő areas. Additional rock and water samples from Covasna and the samples used for the laboratory experiments, including pure phases, artificial mixtures and natural samples are also described.

4.1. Samples from natural CO_2 occurrences

4.1.1. Mihály-Répcelak – Rock samples

From the Mihályi-Répcelak fields 6 sandstone reservoirs out of the 26 (Fig. 1) contain dawsonite (Király et al., 2017), which were selected for this study (Table 2). Four samples (7R1, 7R2, 7R3, 9R) derived from the RM6 drill core from the Mihályi field (1419-1461 m). Sample 6R (1396-1415 m) and 5R2 (1375-1392 m) were selected from RM19 and RM32 drill cores, respectively, from the Répcelak field (Mészáros et al., 1979). All samples, except RM6-9R and RM32-5R2, are from CO_2 reservoirs currently under production by Linde Gas Hungary.

Table 2. Summary of the Mihályi-Répcelak sandstone samples and the applied methods. daw: dawsonite, sd: siderite, ms: magnetic separation.

Area	Mihályi			Répcelak	
Sample name	RM6-9R	RM6-7R1	RM6-7R3	RM32-5R2	RM19-6R
Sample type	sandstone	sandstone	sandstone	sandstone	sandstone
Separated mineral	daw, sd	sd	sd	daw	sd
Separation method	hand-picking, ms	ms	ms	hand-picking	ms
XRD of the bulk sample	x	x	x	x	x
Micro-XRD of separated mineral	x			x	
Infrared spectroscopy of the bulk sample	x	x	x	x	x
Infrared spectroscopy of separated mineral	x			x	
Infrared spectroscopy after hydrogen isotope measurement	x			x	
Raman spectroscopy of mineral					x
Measured $\delta^{13}C$ and $\delta^{18}O$ composition of separated mineral	x	x	x	x	x
Measured δD composition of bulk rock (250-63 μm) for dawsonite	x	x	x	x	x

4.1.2. Ölbő – Rock samples

From the Ölbő field, 32 core samples were collected. Seven sandstones and five siltstones were selected from the Öl-1, Öl-2, Öl-3 and Öl-6 wells (at 1498-1687.5 m depths) for investigation (Table 3). Six samples (Öl 1-7, 1-8-1, 1-8-2, 1-9B1, 1-9B2, 1-10) derives from the Öl-1 well, three samples (Öl 2-5, 2-7A, 2-7B) comes from Öl-2 well, moreover two (Öl 3-5-1, 3-5-2) and one (Öl 6-4A) samples derived from Öl-3 and Öl-6 wells, respectively. These rocks originate from the same geological formation (Alföldi Formation Group) as the samples from Mihályi-Répcelak fields. The Öl-1 and Öl-3 wells are under operation by Messer Hungarogáz Ltd. and Öl-6 is used as a monitoring well in the area (Fig. 1).

4.1.3. Covasna – Rock samples

Dawsonite-bearing rock samples were collected in the Hankó Valley, along the creek in Covasna area in 2018 and 2019. Thirteen brecciated sandstone samples were collected from an outcrop and debris (fluvial deposit) along the creek (Fig 3B, Table 4).

4.1.4. Covasna – Water samples

Water samples were collected in three different sites in the Hankó Valley (Fig. 3B), two sampling points were in bank of the creek where dawsonite-bearing rock samples was found (GPS coordinates: N 45°51’10.48” E 26°12’15.55” and N 45°51’12.29” E 26°12’23.13”) and one was in a registered spring located close to the dawsonite sampling points (GPS coordinate: N 45°51’12.06” E 26°12’18.65”) (Fig. 3B). All together 29 water samples were collected during 4 years between 2018 and 2021. In 2020, from January to July a detailed monitoring campaign was carried out when water samples were collected

for chemical, stable isotope analyses. Also, physical parameters (e.g., temperature) were determined in the field on a monthly base (Table 5). In the creek water, CO_2-bubbling was observed close to the sampling points where the dawsonite-bearing rocks were collected. In addition, this registered spring water also appears to be rich in CO_2 (Stroescu, 1982).

Table 3. Summary of the Ölbő sandstone and siltstone samples and the applied methods. sd: siderite, ms: magnetic separation.

Area	**Ölbő**											
Sample name	Öl 1-7	Öl 1-8-1	Öl 1-8-2	Öl 1-9B1	Öl 1-9B2	Öl 1-10	Öl 2-5	Öl 2-7A	Öl 2-7B	Öl 3-5-1	Öl 3-5-2	Öl 6-4A
Sample type	sandstone	sandstone	siltstone	sandstone	siltstone	siltstone	sandstone	sandstone	siltstone	sandstone	siltstone	sandstone
Separated mineral	sd	sd		sd			sd	sd		sd		sd
Separation method	ms	ms		ms			ms	ms		ms		ms
XRD of the bulk sample	x	x	x	x	x	x	x	x	x	x	x	x
Infrared spectroscopy of the bulk sample	x	x	x	x	x	x	x	x	x	x	x	x
Measured $\delta^{13}C$ and $\delta^{18}O$ composition of separated mineral	x	x		x			x	x		x		x

Table 4. Summary of the Covasna rock samples and the applied methods. br.sandstone: brecciated sandstone, daw: dawsonite, cc: calcite, ahcal: alumohydrocalcite.

Area	**Sample name**	**Sample type**	**Separated mineral**	**Separation method**	**XRD of the bulk sample**	**Micro-XRD of separated mineral**	**Infrared spectroscopy of the bulk sample**	**Infrared spectroscopy of separated mineral**	**Infrared spectroscopy after hydrogen isotope measurement**	**Raman spectroscopy of mineral**	**Measured $\delta^{13}C$ and $\delta^{18}O$ composition of separated mineral**	**Measured δD composition of separated mineral**	**Clumped isotope composition**
	KOV-8	br. sandstone	daw	hand-picking	x	x		x	x		x	x	
	KOV-10	br. sandstone	daw	hand-picking	x	x		x	x		x	x	
	KOV-10/1	br. sandstone	daw	hand-picking	x	x		x	x	x	x	x	
	KOV-10/1 Cc	mineral	cc	hand-picking		x				x	x		x
	KOV-12	br. sandstone	daw	hand-picking	x	x		x	x		x	x	
	KOV-12/2/1	br. sandstone	daw	hand-picking	x	x		x	x		x	x	
	KOV-12/2/2	br. sandstone	daw	hand-picking		x		x	x		x	x	
Covasna	KOV-12/2/3	br. sandstone	daw	hand-picking	x	x		x	x		x	x	
	KOV-2B/1	br. sandstone	daw	hand-picking	x	x		x	x		x	x	
	KOV-2G/1	br. sandstone	daw	hand-picking	x	x		x	x	x	x	x	
	KOV-2G/2	br. sandstone	daw	hand-picking	x	x		x	x		x	x	
	KOV-2G/3	br. sandstone	daw	hand-picking	x	x		x	x	x	x	x	
	KOV-2G/4	br. sandstone	daw	hand-picking	x	x		x	x	x	x	x	
	KOV-2G/5	br. sandstone	daw	hand-picking	x	x		x	x		x	x	
	KOV-13	br. sandstone			x		x						
	KOV-13 Ahcal	mineral	ahcal	hand-picking	x			x		x			

Table 5. Creek and spring water samples from Covasna and the used analytical techniques.

Area	Sample name	Sample type	Determination of temperature	Chemical composition of water	Measured δD and $\delta^{18}O$ of water
	K-M18-1	creek water			x
	K-M18-2	spring water			x
	K-Á19-1	creek water	x		x
	K-Á19-2	spring water	x		x
	K-Á19-3	creek water	x		x
	K-J20-1	creek water	x		x
	K-J20-2	spring water	x		x
	K-J20-3	creek water	x		x
	K-F20-1	creek water	x		x
	K-F20-2	spring water	x		x
	K-F20-3	creek water	x		x
	K-M20-1	creek water	x		x
	K-M20-2	spring water	x		x
	K-M20-3	creek water	x		x
Covasna	K-Á20-1	creek water	x		x
	K-Á20-2	spring water	x		x
	K-Á20-3	creek water	x		x
	K-MJ20-1	creek water	x		x
	K-MJ20-2	spring water	x		x
	K-MJ20-3'	creek water	x		x
	K-J20-1	creek water	x		x
	K-J20-2	spring water	x		x
	K-J20-3	creek water	x		x
	K-JL20-1	creek water	x		x
	K-JL20-2	spring water	x		x
	K-JL20-3	creek water	x		x
	K-JL20-3'	creek water	x		x
	K-AU21-1	creek water		x	x
	K-AU21-2	spring water		x	x

4.2. Carbonates for laboratory experiments

4.2.1. Pure carbonate minerals and synthesized dawsonite

Pure carbonate minerals were used first to determine the original isotopic composition of the minerals using different reaction times. For the measurements, calcite (KALC, Kőszárhegy, Hungary), dolomite (DOL, Kapnikbánya, Romania), dawsonite (DW, synthetized dawsonite), ankerite (ANK, Alsósajó, Slovakia) and siderite (SID, Bírótelek, Hungary) were used (Table 6). For the dissolution 1, 6, 12, 24, 36, 48 and 72 hours were applied at 25 °C.

Table 6. Summary of the pure phases, artificial mixtures and natural samples used in the experiments. KALC: calcite, DW: synthetized dawsonite, DOL: dolomite, ANK: ankerite, SID: siderite.

Sample name	Origin	Sample type	XRD	Infrared spectroscopy	Measured $\delta^{13}C$ and $\delta^{18}O$ composition
KALC	limestone of Kőszárhegy	pure phase			x
DW	synthetized dawsonite	pure phase	x	x	x
DOL	dolomite from Kapnikbánya	pure phase			x
ANK	ankerite from Alsósajó	pure phase			x
SID	siderite from Bírótelek	pure phase			
ME1		artificial mixture			x
ME2	mixed from pure phases	artificial mixture			x
ME3		artificial mixture			x
RM6-9R	sandstone from Mihályi	natural sample	x	x	x
RM32-5R2	sandstone from Répcelak	natural sample	x	x	x

Dawsonite was synthetized for the lab experiments (used as pure phase and in the artificial mixtures) in order to have pure dawsonite phase which is not contaminated with other minerals and can be used in the experiments. To control the purity of the synthesized dawsonite, X-ray diffraction and Infrared spectroscopy were applied.

Dawsonite synthesis was carried out at the Technical University of Graz (Austria) by Martin Dietzel and Bettina Purgstaller. Dawsonite was synthetized in a titanium reactor at 175 °C following the method described by Van Der Heem (1980). During the experiment 15 g of gibbsite (Riedel-De Haen), 45 g of Na_2CO_3 (Roth), 18 g of $NaHCO_3$ (Roth) and 281 g of ultrapure water (Millipore Integral 3: 18.2 $M\Omega cm^{-1}$) were continuously mixed in a 600 mL titanium reactor (Parr Instruments) for 24 h at 175 °C, 7 bars and pH=10.1.

4.2.2. Artificial mixtures

Artificial mixtures (ME1, ME2, ME3) were made by mixing of the pure phases in different ratios. ME1 sample contains 40 % calcite (KALC), 30 % dolomite (DOL), 10 % dawsonite (DW), 15 % ankerite (ANK) and 5 % siderite (SID) (Table 6). ME2 samples compose by 15 % calcite, 30 % dolomite, 10 % dawsonite, 35 % ankerite and 10 % siderite. ME3 sample contains 40 % calcite, 20 % dawsonite and 40 % ankerite (Table 6). This sample does not contain dolomite and siderite at all. For the dissolution 6, 24 and 48 hours were applied at 25 °C.

4.2.3. Natural samples

Two natural samples were selected from the Mihályi-Répcelak field to test the selective acid extraction method. The samples contain dawsonite (RM6-9R, RM32-5R2) but not calcite (Table 7), to keep the system simple. The following reaction times were applied at 25 °C: 6, 24 and 48 hours. To verify the results, dawsonite (RM6-9R, RM32-

5R2) was separated and stable C, O isotope composition was determined (Cseresznyés et al., 2021).

Table 7. Mineral composition of the selected natural samples for the experiments in m/m%. ND: not detected.

Sample	Muscovite	Kaolinite	Quartz	K-feldspar	Calcite	Dolomite	Ankerite+ Siderite	Dawsonite	Notes	Reference
RM6-9R	15	3	36	2	ND	7	21	16	bulk rock	Király (2017)
RM32-5R2	8	3	45	1	<1	8	27	8	bulk rock	Király (2017)

5. Analytical methods

Different analytical methods were applied to determine the mineral composition of the rock samples, the water chemistry and the isotopic composition both of the carbonate minerals (pure phases, artificial mixtures and natural samples) and the water samples. The analytical techniques are summarized in tables. Table 2-4. contain the analysis on the natural rock samples, Table 5 shows the measurements of natural water samples and Table 6 contains the samples which are related to the experimental work.

5.1. Phase identification and analytics

Petrographic features of the natural samples from Mihályi-Répcelak, Ölbő and Covasna (Table 2-4) area were characterized by both optical and electron microscopy, thin sections were studied under polarization microscope at the Lithosphere Fluid Research Lab, ELTE (Budapest, Hungary). Scanning electron microscopy of the thin sections and fresh broken surface was carried out on AMRAY 1830 I/T6 scanning electron microscope (SEM) coupled with EDAX PV 9800 energy dispersive X-ray-spectrometer at the Department of Petrology and Geochemistry, ELTE (Budapest, Hungary), and with Hitachi TM4000 Plus scanning electron microscope equipped with AztecOne EDS (15kV, 0.8 nA) at the Research and Industrial Relations Center (RIRC), ELTE (Budapest, Hungary).

5.1.1. X-ray diffraction

The mineralogical composition of bulk rock powders (<63 μm), mineral separates and synthetized dawsonite (DW) (Table 2) were determined at the Supervisory Authority for Regulatory Affairs (SARA, Budapest, Hungary) with a Bruker D2 Phaser XRD powder diffractometer (CuKα radiation, 30kV, 10mA) in Bragg–Brentano geometry, in Theta/Theta vertical goniometer alignment. Patterns were recorded in 5-70° (2θ) range,

with 0.04° (2θ) steps, with an SSD detector. Phase identification was made with Search/Match on Crystallography Open Database (COD) in EVA. Quantitative evaluation was made by Rietveld refinement in TOPAS6 software. The spectra visualization was carried out with OriginPro 2021 (9.8.0.200 version) software.

5.1.2. Micro X-ray diffraction

Micro X-ray diffraction (MicroXRD) analysis of separated dawsonite samples and one separated calcite (KOV-10/1 cc) sample were performed at Institute for Geological and Geochemical Research (IGGR, Budapest, Hungary) using a RIGAKU D/MAX RAPID II diffractometer, which is a unique combination of a MicroMax-003 third generation microfocus, sealed-tube X-ray generator, and a curved imaging plate (IP) detector. The diffractometer was operated with CuKα radiation generated at 50 kV and 0.6 mA. The powdered samples for the micro-diffraction measurements were encapsulated in a borosilicate-glass capillary, with a diameter of 0.3 mm and a wall thickness of 0.01 mm, by a vertical manual charging process. Then, the capillary was analysed by the micro-diffractometer in transmission mode, with a beam spot diameter of 100 μm (Kovács et al. 2021). For each measurement, 0.5–1 mg sample was placed in the funnel end of the capillary, and the sample was tapped into the narrow portion. Acquisition time for each measurement was set to 5 minutes. The IP was read by a laser scanning readout system in approximately 1 min. 2DP RIGAKU software was used to record the diffraction image from the laser readout, allowing to determine the area to integrate for a 2θ versus intensity plot. This plot was read into the RIGAKU PDXL 1.8 software for data analysis. For the quantitative analysis, the diffraction patterns were processed using the Siroquant V4 software and the modal contents were determined by Rietveld method.

5.1.3. Infrared spectroscopy

Attenuated total reflection Fourier transform infrared (ATR-FTIR) spectroscopy is a very sensitive non-destructive method to identify OH-bearing phases. ATR-FTIR technique was used for more purposes. Firstly, to identify dawsonite, secondly to check the presence or absence of dawsonite in the natural samples. Lastly, the method was applied to check the success of the separation without material loss before the hydrogen isotope measurements. Following hydrogen isotope measurements, the OH^- release from the heated dawsonite sample was confirmed. The analysis of the samples was repeated minimum three times.

The samples were analysed by a Bruker Vertex 70 Fourier-transformation infrared (FTIR) spectrometer equipped with a Bruker Platinum diamond ATR cell and a DTGS detector at IGGR and SARA (Budapest, Hungary). The samples were dried at 70-80 °C for at least 30 min to remove the adsorbed water on the samples (Udvardi et al., 2014, Tóth et al., 2012). During the measurement 70N/cm constant pressure on the ATR cell, 4 resolution, 64 scan/sample were applied. For the interpretation OPUS 7.2 software was used. On the spectrum's atmospheric compensation (H_2O and CO_2 compensation), average of three spectra/samples, baseline correction (concave rubberband correction, number of baseline points: 64, 1 iteration) were applied, and cut it in the mid-infrared spectral range (400-4000 cm^{-1}). The spectra visualization was carried out with OriginPro 2021 (9.8.0.200 version) software.

5.1.4. Raman spectroscopy

Micro-Raman spectroscopic analysis is a non-destructive method which was used to identify separated minerals like dawsonite, siderite, calcite (KOV-10/1 Cc), alumohydrocalcite (KOV-13 Ahcal) and also minor constituents in the bulk rock such as anatase, realgar etc. The analysis was carried out at the RIRC of the Faculty of Science, ELTE (Budapest, Hungary). A confocal HORIBA Labram HR800 spectrometer was used with Nd:YAG laser (λ = 532 nm) excitation, 600 grooves/mm optical grating, 100 μm confocal hole, 2×30 s acquisition time and a 100× objective (numerical aperture: 0.9). The laser power was ∼25 mW on the sample surface. The spectral resolution was 3.0 cm^{-1}. The spectra were elaborated with OriginPro 2021 (9.8.0.200 version) software.

5.2. Isotope analyses

Isotope analysis was carried out on the samples used for laboratory experiments (pure phases, artificial mixtures and natural samples) and on the samples from natural CO_2 occurrences (Mihályi-Répcelak, Ölbő and Covasna).

Based on the previous experiences by Király (2016a) and Cseresznyés et al. (2021) on the Mihályi-Répcelak samples, a new method was applied to disintegrate the rock samples, which allows the physical separation of dawsonite and siderite from each other and from other carbonates, to determine their isotopic compositions individually. Due to textural reasons, the other carbonates could not be separated from each other (see section 2.1.2 and 6.2.1).

This method was not reasonable to use for samples from Covasna because dawsonite precipitated on the surface of the brecciated sandstone and could be easily separated in most cases.

5.2.1. Preparation for isotope analysis - Mineral separation from natural samples

The Mihályi-Répcelak and Ölbő rock samples were disintegrated by H_2O freezing-melting cycles. The advantage of this method, compared to crushing, is that the majority of minerals is preserved in their original grain size, shape and habit which helps their separation. Following disintegration, wet sieving was carried out producing grainsize fractions: >250 μm, 250-63 μm, <63 μm.

In case of the Mihályi-Répcelak samples, dawsonite grains were separated by hand picking under stereomicroscope from the 250-63 μm grain size fractions from samples RM6-9R and RM32-5R2, which have the highest modal content of dawsonite (Table 7). Under stereomicroscope dawsonite is easily distinguishable from the other carbonates because dawsonite is the only white fibrous mineral phase in the samples.

For siderite separation from the Mihályi-Répcelak and Ölbő samples, the same size fractions (250-63 μm) were used in a Frantz Isodynamic Magnetic Separator (0.6 A magnet current, Parfenoff et al., 1970) at SARA (Budapest, Hungary) from samples RM6-9R, RM6-7R3, RM6-7R1 (Mihályi), RM19-6R (Répcelak), and Öl 1-7, Öl 1-8-1, Öl 1-9B1, Öl 2-5, Öl 2-7A, Öl 3-5-1, Öl 6-4A (Ölbő). The purity of the separates depends on the mineral composition of the host rock and the quality of the mineral grains (Strong and Driscoll, 2016). Therefore, the success of the magnetic separation was checked under stereomicroscope (siderite has an orange color and isometric grain shape) and also with SEM (Hitachi TM4000 Plus AztecOne) at RIRC, ELTE (Budapest, Hungary).

In Covasna samples, dawsonite occurs on the surface of the sample, therefore hand-picking was used to separate dawsonite. From one sample (KOV-10/1), calcite was also separated by hand-picking for clumped isotope measurements. The success of the separation was checked with MicroXRD and Raman spectroscopy.

5.2.2. Carbon and oxygen isotope determination of carbonates

Stable carbon and oxygen isotope compositions were determined on 150–200 μg of carbonate powders. Carbonate powders were prepared from pure phases, artificial mixtures and natural bulk samples (Table 6-7). The powders were reacted with orthophosphoric acid at 25 °C for 1, 6, 12, 24, 36 and 72 hours.

The same amount of powders were made from the mineral separates, dawsonite and siderite (from Mihályi-Répcelak, Ölbő and Covasna, Table 2-4.) by reacting the powders with orthophosphoric acid at 72 °C for 1 hour for dawsonite and for 24 hours for siderite (Spötl and Vennemann, 2003; Cseresznyés et al., 2021). Acid fractionation factors determined by Rosenbaum and Sheppard (1986) and Kim et al. (2007) were applied for siderite and dawsonite, respectively (the fractionation factor for calcite was also applied to dawsonite in other studies, e.g., Baker et al., 1995; Liu et al., 2011).

The separated CO_2 was analysed, using an automated GASBENCH II sample preparation bench attached to a Thermo Finnigan Delta Plus XP Isotope Ratio Mass Spectrometer (IRMS) at IGGR (Budapest, Hungary). The isotopic compositions are expressed as $\delta^{13}C$ ($\delta^{13}C=((^{13}C/^{12}C_{sample})/(^{13}C/^{12}C_{VPDB})-1)*1000$) and $\delta^{18}O$ ($\delta^{18}O=((^{18}O/^{16}O_{sample})/(^{18}O/^{16}O_{VSMOW})-1)*1000$) values (in ‰) relative to Vienna Pee Dee Belemnite (VPDB) and Vienna Standard Mean Ocean Water (VSMOW) standards, respectively (Coplen, 1996). Three laboratory standards (calibrated against NBS-18, NBS-19 and LSVEC) provided by the International Atomic Energy Agency were applied for standardization (Flesch et al., 1973; Friedman et al., 1982). A Harding Iceland Spar (Landis, 1983) sample was measured as unknown, and yielded $\delta^{13}C$ and $\delta^{18}O$ values of –4.84 ±0.05 ‰ and –18.56 ±0.07 ‰ (n=24), respectively. These values are within error of the published values of –4.80 and –18.56 ‰, respectively (Landis, 1983). Based on these results and measurement reproducibility, the accuracies of $\delta^{13}C$ and $\delta^{18}O$ values are estimated to be better than ±0.1‰.

5.2.3. Hydrogen isotope measurement of dawsonite

Stable hydrogen isotope composition of the hydroxyl group of dawsonite ($NaAlCO_3(OH)_2$) was determined using an LGR LWIA-24d type laser analyser attached to an in-house built inlet system at IGGR (Czuppon et al., 2014; Demény et al., 2016). Bulk rock samples (250-63 μm fraction) containing dawsonite from Mihályi (RM6-9R, RM6-7R1, RM6-7R3, Table 2) and Répcelak (RM32-5R2, RM19-6R, Table 2) were heated up to 350 °C to release the OH^- group (Cseresznyés et al., 2021). In this instance bulk rock sample could be used because the only other OH^--bearing mineral present (kaolinite) decomposes thermally at temperatures as high as 580 °C (Földvári, 2011), leaving it intact at the above mentioned temperature. In the separated dawsonite from Covasna (13 samples, Table 4), 8 mg separated dawsonite was used. The liberated fluids (H_2O and CO_2) were trapped in a liquid nitrogen-cooled cold finger. The trapped CO_2

was liberated at –80 °C (using melting Ethyl alcohol) and removed from the system, and then the H_2O was liberated at 80 °C and introduced into the laser analyser (Cseresznyés et al., 2021).

The isotopic compositions are expressed as δD ($\delta D=((^2H/^1H_{sample})/(^2H/^1H_{V\text{-}SMOW})-1)*1000$) values relative to VSMOW (Coplen, 1996), the reproducibility of the measurements is estimated to be ±2 ‰ based on synthetic dawsonite (DW) analyses.

5.2.4. Clumped isotope measurement of calcite (KOV-10/1 Cc)

Carbonate clumped isotope analysis was carried out on the separated calcite sample (KOV-10/1 Cc from Covasna, Table S2) with a Thermo Scientific 253 Plus 10 kV isotope ratio mass spectrometer (IRMS) at Isotope Climatology and Environmental Research Centre, Atomki (Debrecen, Hungary). The details of the measurements are found in the Supplementary text 12.1. section.

5.3. Analyses of water samples

The physical and chemical analysis of water samples from Covasna (Table 5) was carried out at SARA (Budapest, Hungary). The temperature of the water samples was measured on site. The details of the analysis of water are found in Supplementary text 12.2. section.

5.3.1. Determination of hydrogen and oxygen isotope composition of water samples (Covasna)

Stable hydrogen and oxygen isotope analyses of 29 water samples from Covasna were carried out (Table 5) using a Liquid-Water Isotope Analyser-24d manufactured by Los Gatos Research at IGGR (Budapest, Hungary). The isotopic compositions of the water samples are expressed as δD and $\delta^{18}O$ in ‰ relative to V-SMOW (Vienna Standard Mean Ocean Water; Coplen et al., 1996). The precision is better than 1.0‰ and 0.15‰ for hydrogen and oxygen isotope ratios, respectively. More details of the stable isotope analyses are described in Czuppon et al. (2018).

5.4. Geochemical modelling

Geochemical modelling was used to simulate the chemical processes which take place after large amount of CO_2 injection into a sandstone reservoir. For the thermodynamic calculations PHREEQC 3.0 geochemical modelling software (Parkhust and Appelo, 2012) was used with the PHREEQC.dat database.

For the models, the mineral composition of Ölbő sandstone samples were used, as they were not flooded naturally with CO_2 (as in Mihályi-Répcelak case) (explanation in section 7.2.1). The aim of the modelling was to better understand the mineral dissolution and precipitation in the sandstone reservoir over 200 years and compare the modelling results with the observed reactions in the Mihályi-Répcelak samples. In addition, sensitivity analysis of the water composition was also performed on three different water types (ion-free water, Na-Cl type and Na-HCO_3 type water), and reservoir pressure (140-215 bar) and temperature (70-100 °C) were also varying in the models. Thermodynamic-batch, kinetic-batch and kinetic-reactive transport models were run with and without supercritical CO_2. Thermodynamic-batch models show the equilibrium state of the reactions and do not consider the time dependence of reactions. Kinetic-batch models consider time but run without fluid flow. Porewater is flowing through the rock and mineral reactions are time dependent and a more realistically described by kinetic-reactive transport models.

5.4.1. Input parameters

In the models the following parameters must be defined: equilibrium phases, secondary minerals, porosity of the rock, composition of the solution and gas, the pressure and temperature of the reservoir.

To add the equilibrium phases for the thermodynamic calculations, the average mineral composition of the Ölbő sandstone samples was used and calculated based on Szabó et al. (2018) to mol/kgWater unit (Table 8). Dolomite was eliminated from the model based on the petrographic observations by Király (2017) on the Mihályi-Répcelak reservoir samples (dolomite always has ankerite rim, therefore it is sealed off from reaction with porewater; see section 2.1.2). Chlorite (Chlorite14A) was also eliminated because its thermodynamic parameters sometimes blocked the model, chlorite has no important influence on the reactions. The other challenge was the presence of ankerite in the rocks. The PHREEQC.dat database contains ankerite, but its thermodynamic data was not suitable to use in the CO_2-water-sandstone system. Therefore, ankerite was tested with four different thermodynamic data and chemical composition in thermodynamic-batch models (Gysi and Stefánsson, 2012; Koenen et al 2014; Tesfay, 2006; Voigt et al., 2018). In agreement with the results of Király (2017) and Sendula (2015), the data of Koenen et al. (2014) proved to be appropriate and was used in all models and defined in the PHASES block of the geochemical model script. The Ölbő sandstones contain mica which was

divided into 50 % illite and 50 % muscovite, muscovite is present as K-mica in the PHREEQC.dat database. Plagioclase is mostly albite in the Mihályi-Répcelak sandstone reservoirs (Király, 2017). Albite, K-feldspar and K-mica was not allowed to precipitate in the models (for details see 7.2.1).

Table 8. Average mineral composition of Ölbő sandstone samples (m/m%) used in PHREEQC as equilibrium phases. ρ: density of the mineral, M: molar mass of the mineral, c: amount of mineral in mol/kgWater.

		input	input	input	used in PHREEQC
Average of Ölbő sandstones	**Equilibrium phases**	**m/m%**	**ρ (g/cm³)**	**M (g/mol)**	**c (mol/kgW)**
Plagioclase	albite	11.00	2.62	262	5.67
Kaolinite	kaolinite	2.89	2.60	258	1.51
Calcite	calcite	6.46	2.71	100	8.72
Chlorite	chlorite(14A)	0.00	2.65	554	0.00
Dolomite	dolomite	0.00	2.85	184	0.00
Mica	K-mica	4.68	2.82	399	1.58
Mica	illite	4.68	2.75	384	1.64
K-feldspar	K-feldspar	4.67	2.56	278	2.27
Quartz	quartz	43.17	2.63	60	97.12
Ankerite	ankerite	5.77	3.05	206	3.77
Siderite	siderite	2.31	3.96	116	2.69
Dawsonite	dawsonite	0	2.42	144	0

Secondary minerals also need to be listed in the modelling code. Based on the petrographic observation on the Mihályi-Répcelak samples by Király (2017), dawsonite should precipitate as a response of CO_2 flooding. Dawsonite is missing from the PHREEQC.dat database, therefore thermodynamic data of dawsonite was added from the LLNL.dat database (thermo.com.V8.R6.230 thermodynamic database compiled at Lawrence Livermore National Laboratory) according to Hellevang et al. (2010) and Szabó et al. (2016), and defined in the PHASES block of the geochemical model script. The density of the rock was 2.71 g/cm^3.

The kinetic-batch models were run for 200 years in different time steps. For the kinetic-batch modeling, minerals have to be defined in the KINETICS block of the geochemical model script with the following parameters: starting amount of the minerals (Table 8 last column) and secondary minerals (dawsonite, m0= 0 mol/kgW), and the molar mass of the minerals (Table 8). The specific surface area of the mineral phases was defined with the highest value for the given mineral in the Rossendorf Expert System for Surface and Sorption Thermodynamics (RES^{3}T database) (Table 9, www.hzdr.de).

Table 9. Specific surface areas of the minerals in m^2/g (RES^{3}T database, www.hzdr.de).

	albite	kaolinite	calcite	K-mica	illite	K-feldspar	quartz	ankerite	siderite	dawsonite
Specific surface area	21.6	200	22	0.68	200	12	58	0.1	0.175	2.8

The reaction rates of mineral dissolution and precipitation in acidic, neutral and alkaline environments (Rate constant: log k, Arrhenius activation energy: E, Reaction order: n) were defined in the RATES block of the geochemical model script for all of the minerals if rate constants were available (Palandri and Kharaka, 2004; Szabó et al., 2018). The mineral precipitation was controlled, since it is approximately 100 times slower than the mineral dissolution (Falus et al., 2016; Pham et al, 2011; Szabó et al., 2016; 2018).

Sensitivity analyses were carried out for the solution (reservoir fluid) composition, ion-free water, Na-Cl type and Na-HCO_3 type waters from Ölbő area were used (Table 10). Aluminium is a limiting factor in the models but usually it is not measured in the general water chemistry, therefore 0.05 mg/L aluminium was added in the SOLUTION block of the geochemical model script.

Table 10. Three different solution compositions in mg/L for sensitivity analysis in the models.

Chemical parameters	use in the PHREEQC	Ion-free water	Na-Cl type water	Na-HCO_3 type water
pH	pH	7	6.75	8.03
Na^+	Na		2052.8	1795.3
Ca^{2+}	Ca		186.3	230.3
Mg^{2+}	Mg		26.2	66.3
Fe	Fe		130.4	21.8
Cl^-	Cl		3315.1	897.8
HCO_3^-	Alkalinity		919.3	2430.2
SO_4^-	S(6)		36.2	64.2
SiO_2	Si		13.3	32.1
Al^{3+}	Al		0.05	0.05

For the gas composition, 100 % pure CO_2 was used in the CO_2 flooded models (GAS_PHASE block) at the calculated reservoir pressures (140-215 bar) and temperatures (70-100 °C). The pressure and temperature values were calculated based on the depth of the Mihályi-Répcelak and Ölbő sandstone samples. For the temperature calculation, the geothermal gradient (40 °C/km) of the Little Hungarian Plain (Dövényi et al., 1983) and the annual average surface temperature (12 °C) were used. According to Szamosfalvi (2014), who reinterpreted the well logs in the Mihályi-Répcelak area, the studied samples were located 700 m deeper than now, therefore these values were added

to the current depth to calculate the maximum *paleo pressure* and *paleo temperature* of the reservoirs.

The 1D-reactive transport model ran with one selected pressure and temperature pair (166 bar, 78 °C) for ~50 years in 300 meters distance. Time steps were 1 year in sec, cell length was 10 m. The dispersivity was 0.5 m and the diffusion coefficient was 2 x 10^{-9} m^2/s.

6. Results

6.1. Carbonates dissolution – reaction time and CO_2 yield

The determination of the isotope composition of carbonates from bulk rocks which contains more than two carbonate phases is not straightforward. To investigate time of dissolution of various carbonates, a series of experiments was carried out. Following dissolution times were used: 1, 6, 12, 24, 36, 48 and 72 hours at 25 °C. Pure phases (calcite, dawsonite, dolomite, ankerite and siderite), artificial mixtures (ME1, ME2, ME3, Table 6) and natural samples (RM6-9R, RM32-5R2, Table 7) were subject in these experiments. The artificial mixtures and natural samples were measured after 6, 24 and 48 hours of reaction time to test whether the method suggested by Liu et al. (2011) is appropriate to separate the carbonate phases.

In the following, the isotopic composition and CO_2 yields (amount of the extracted CO_2 gas from the carbonate) of pure carbonates (calcite, dawsonite, dolomite, ankerite and siderite) are presented with the increasing reaction time (Fig. 4-8) during the selective extraction experiments.

The $\delta^{13}C$ value of calcite (KALC) is between 1.6 ‰ and 1.7 ‰ during the 1-72 h experiments, the $\delta^{18}O$ values are varying between 19.3 ‰ and 19.6 ‰, the average value is 19.5±0.1 ‰. The integrated area of the extracted CO_2 seemed to stabilize after 12 hours (Fig. 4). Moreover, note that majority of calcite dissolved within the 1st hour.

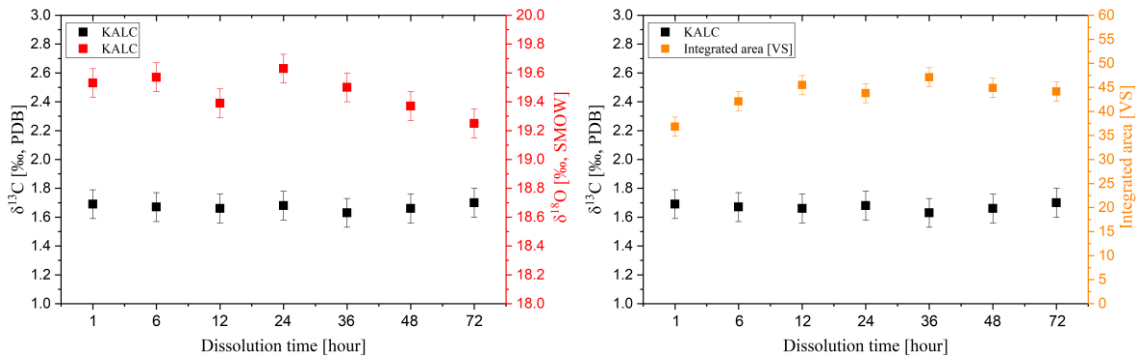

Fig. 4. Sequential acid extraction of calcite (KALC). Calcite $\delta^{13}C$ and $\delta^{18}O$ values (left), and the integrated area of the extracted CO_2 gas (right) during the 1-72 h experiment.

The $\delta^{13}C$ values of dawsonite (DW) are between –2.9 ‰ and –3.0 ‰, whereas the $\delta^{18}O$ values vary between 8.3 ‰ and 8.6 ‰. However, the isotopic values do not show systematic trend with time. The extracted CO_2 gas neither reveals systematic trend implying that majority of the CO_2 can be evolved in the 1st hour (Fig. 5).

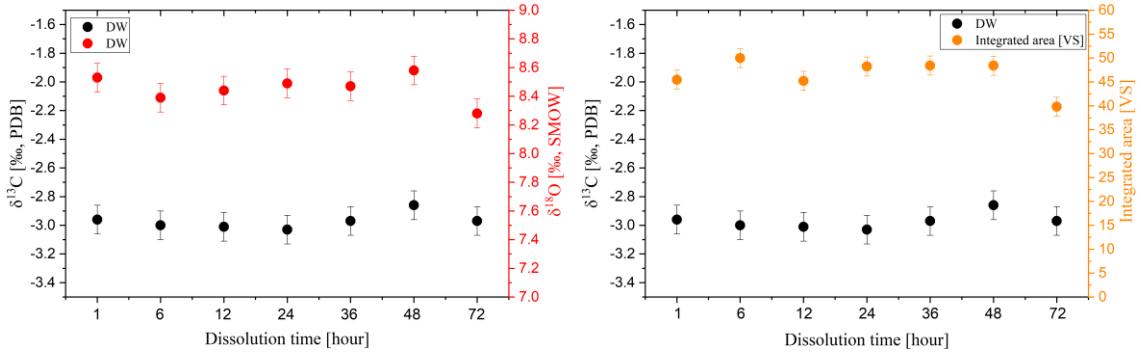

Fig. 5. Sequential acid extraction of dawsonite (DW). Dawsonite $\delta^{13}C$ and $\delta^{18}O$ values (left), and the integrated area of the extracted CO_2 gas (right) during the 1-72 h experiment.

In dolomite (DOL), it seemed to be some slight positive shift in both $\delta^{13}C$ and $\delta^{18}O$ values (Fig. 6). Although the change is small: the $\delta^{13}C$ values vary between –3.3 and –3.4 ‰; whereas the $\delta^{18}O$ values range from 10.9 to 11.1 ‰. The amount of CO_2 shows significant increase with time and stabilizes after 36 hours (Fig. 6). The liberated CO_2 after 6 hours reached 50 % of the maximum value.

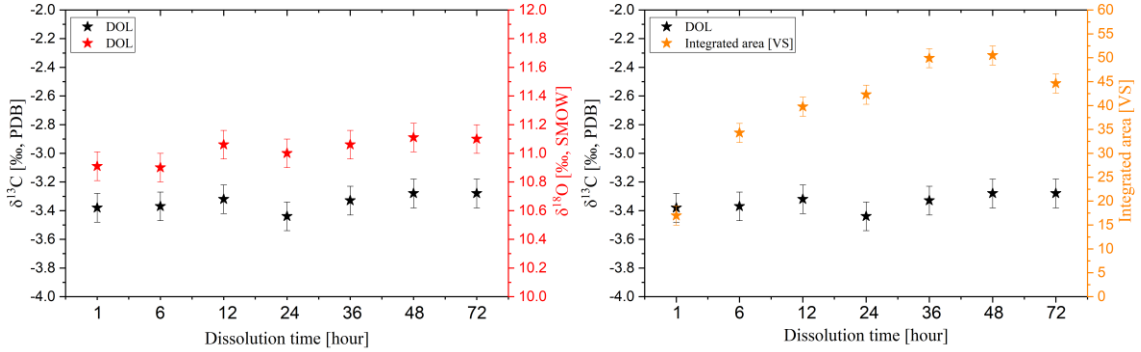

Fig. 6. Sequential acid extraction of dolomite (DOL). Dolomite $\delta^{13}C$ and $\delta^{18}O$ values (left), and the integrated area of the extracted CO_2 gas (right) during the 1-72 h experiment.

The isotopic values of ankerite also showed relative high variability, the $\delta^{13}C$ values are between –4.3 ‰ and –4.6 ‰, meanwhile $\delta^{18}O$ values are 19.0-19.3 ‰ (Fig. 7). In addition, the $\delta^{13}C$ values reveal systematic trend in the beginning of the experiment, it stabilized after 12 hours. The amount of CO_2 of ankerite shows an increasing trend within 36-hour reaction time when it reached the maximum value (Fig. 7). More than 50 % of ankerite dissolved after 12 hours.

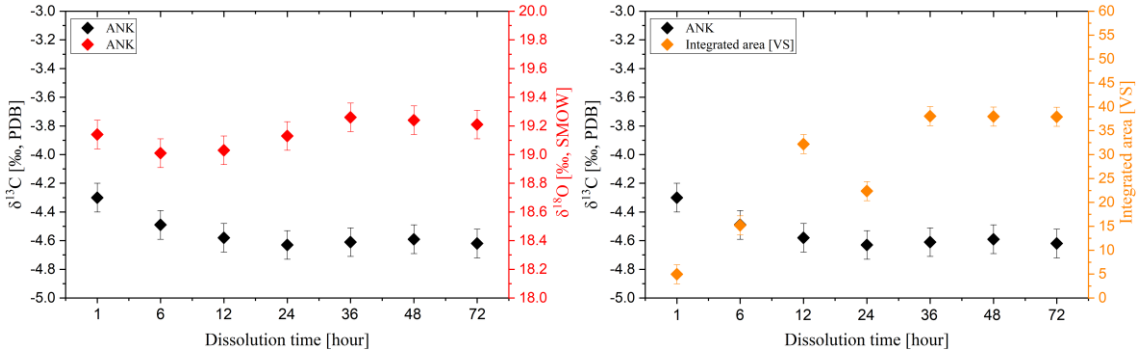

Fig. 7. Sequential acid extraction of ankerite (ANK). Ankerite $\delta^{13}C$ and $\delta^{18}O$ values (left) and the integrated area of the extracted CO_2 gas (right) during the 1-72 h experiment.

Siderites (SID) were investigated just after 24 hours reaction time. Its carbon isotope data are between –6.3 ‰ and –6.5 ‰, the oxygen isotope data are increasing with the reaction time, varying from 16.1 ‰ to 17.4 ‰ (Fig. 8). The liberated CO_2 from siderite showed a continuous increase from 1.5 to 19.2 VS [velocity secundum] and reached the maximum value in the 72nd hour (Fig. 8).

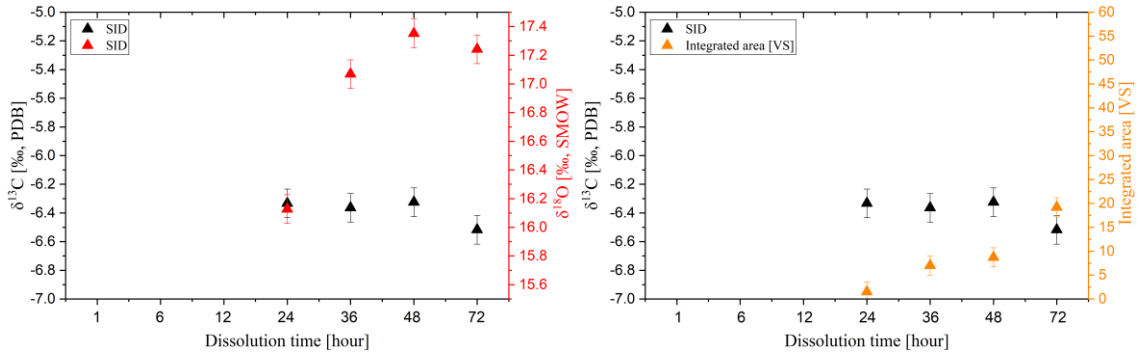

Fig. 8. Sequential acid extraction of siderite (SID). Siderite $\delta^{13}C$ and $\delta^{18}O$ values (left), and the integrated area of the extracted CO_2 gas (right) during the 1-72 h experiment.

In the artificial mixtures and natural samples, 6, 24, 48 hours reaction times were applied to test the applicability of the method of Liu et al. (2011). These samples are composed of varying amounts of carbonates (calcite, dawsonite, dolomite, ankerite and siderite). Values of $\delta^{13}C$ and $\delta^{18}O$ in sample ME1 are (–0.6 ‰) - (–3.2 ‰) and 15.7 ‰ - 17.3 ‰, respectively (Table 11). The values in ME2, $\delta^{13}C$ are between –2.2 ‰ and –3.7 ‰, $\delta^{18}O$ values fall in the range from 15.0 ‰ to 18.2 ‰ (Table 11). In ME3 sample, $\delta^{13}C$ and $\delta^{18}O$ values ranges (–0.7 ‰) - (–4.0 ‰) and 17.1 ‰ - 20.9 ‰, respectively (Table 11). The natural sample RM6-9R (bulk) from Mihályi shows 1.6 ‰ - 2.7 ‰ $\delta^{13}C$ values, and 20.7 ‰ - 26.6 ‰ $\delta^{18}O$ values (Table 11). The RM32-5R2 (bulk) natural sample from Répcelak shows $\delta^{13}C$ values from 0.0 ‰ to 0.5 ‰, and the $\delta^{18}O$ values are between 22.6 ‰ and 26.9 ‰ (Table 11).

Table 11. $\delta^{13}C$, $\delta^{18}O$ values and the integrated area of the extracted CO_2 gas for pure phases, artificial mixtures and natural samples from the experiments. KALC: calcite, DW: dawsonite, DOL: dolomite, ANK: ankerite, SID: siderite, PDB: Pee Dee Belemnite, SMOW: Standard Mean Ocean Water, VS: velocity secundum.

Sample name	Sample type	Temperature	Reaction time [hour]	$\delta^{13}C$ [‰, PDB]	$\delta^{18}O$ [‰, PDB]	$\delta^{18}O$ [‰, SMOW]	Integrated area [VS]
KALC	pure phase	25 °C	1	1.7	-11.0	19.5	36.8
			6	1.7	-11.0	19.6	42.1
			12	1.7	-11.2	19.4	45.5
			24	1.7	-10.9	19.6	43.8
			36	1.6	-11.1	19.5	47.1
			48	1.7	-11.2	19.4	44.9
			72	1.7	-11.3	19.3	44.1
DW	pure phase	25 °C	1	-3.0	-21.7	8.5	45.5
			6	-3.0	-21.8	8.4	50.0
			12	-3.0	-21.8	8.4	45.2
			24	-3.0	-21.7	8.5	48.2
			36	-3.0	-21.8	8.5	48.4
			48	-2.9	-21.7	8.6	48.4
			72	-3.0	-22.0	8.3	39.8
DOL	pure phase	25 °C	1	-3.4	-19.4	10.9	17.0
			6	-3.4	-19.4	10.9	34.3
			12	-3.3	-19.3	11.1	39.8
			24	-3.4	-19.3	11.0	42.3
			36	-3.3	-19.3	11.1	49.9
			48	-3.3	-19.2	11.1	50.5
			72	-3.3	-19.2	11.1	44.6
ANK	pure phase	25 °C	1	-4.3	-11.4	19.1	5.0
			6	-4.5	-11.5	19.0	15.2
			12	-4.6	-11.5	19.0	32.2
			24	-4.6	-11.4	19.1	22.4
			36	-4.6	-11.3	19.3	38.1
			48	-4.6	-11.3	19.2	38.0
			72	-4.6	-11.4	19.2	37.9
SID	pure phase	25 °C	24	-6.3	-14.3	16.1	1.5
			36	-6.4	-13.4	17.1	7.0
			48	-6.3	-13.2	17.4	8.7
			72	-6.5	-13.3	17.2	19.2
ME1	artificial mixture	25 °C	6	-0.6	-14.4	16.0	
			24	-3.2	-14.8	15.7	
			48	-2.8	-13.2	17.3	
ME2	artificial mixture	25 °C	6	-2.2	-15.4	15.0	
			24	-3.7	-13.5	17.0	
			48	-3.4	-12.3	18.2	
ME3	artificial mixture	25 °C	6	-0.7	-13.4	17.1	
			24	-4.0	-10.6	20.0	
			48	-3.4	-9.7	20.9	
RM6-9R	natural sample	25 °C	6	1.6	-9.9	20.7	
			24	2.3	-6.6	24.1	
			48	2.7	-4.2	26.6	
RM32-5R2	natural sample	25 °C	6	0.1	-8.0	22.6	
			24	0.0	-5.5	25.3	
			48	0.5	-3.9	26.9	

6.2. Natural CO_2 occurrences

Mihályi-Répcelak and Ölbő fields

6.2.1. Mineral composition of Ölbő rock samples

The selected samples from Ölbő field are fine-grained greyish sandstones and brownish siltstones. The mineral composition of sandstones is 30-58 m/m% quartz, 9-13 m/m% plagioclase, 6-15 m/m% dolomite, 3-19 m/m% calcite, 5-6 m/m% ankerite, 1-4 m/m% siderite (the Öl 6-4A sample does not contain siderite, Table 12), 3-7 m/m% K-feldspar, 4-24 m/m% mica, 1-4 m/m% kaolinite and 4-5 m/m% chlorite (the Öl 6-4A and Öl 9-B1 samples do not contain chlorite, Table 12). Thin sections of three sandstone sample (Öl 1-8-1, Öl 1-9B1, Öl 3-5-1) were used to count 300 points per image for the QFL (quartz, feldspar, lithoclast) classification which is based on McBride (1963). The Ölbő samples contain 51-62 v/v% quartz (Q), 10-11 v/v% feldspar (F) and 28-35 v/v% lithoclast (L) and they can be classified to feldspathic litharenites (Fig. 9).

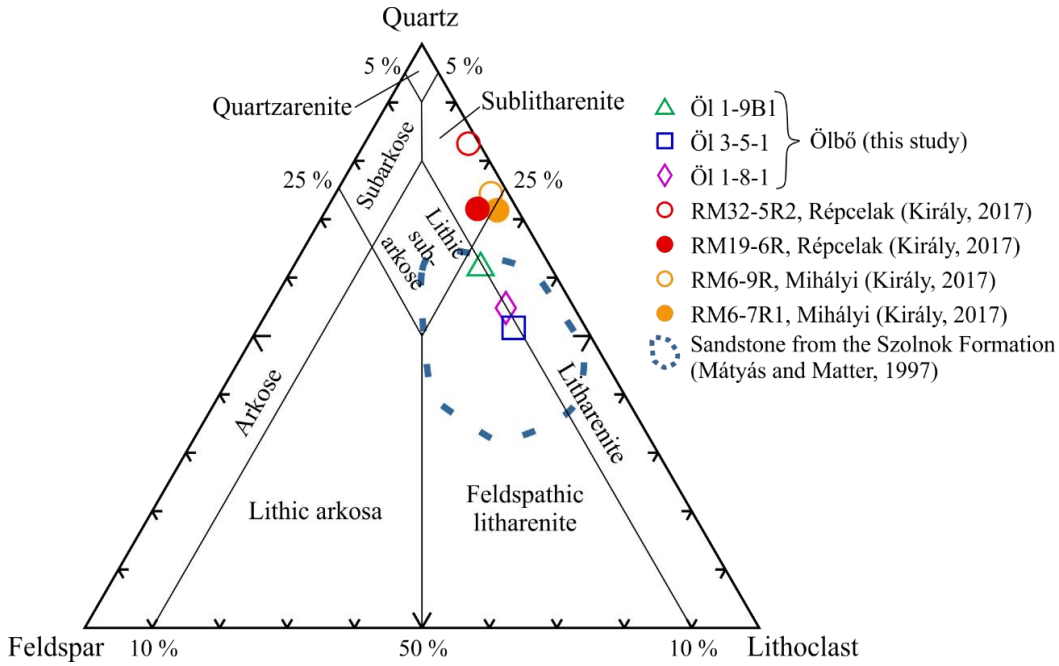

Fig. 9. Quartz, feldspar and lithoclast triangle of the Öl 1-8-1, Öl 1-9B1 and Öl 3-5-1 sandstone samples from Ölbő. Relevant samples from Mihályi-Répcelak and sandstone from Lower Pannonian formation are also shown (Király, 2017; Mátyás and Matter, 1997). Redrawn after McBride (1963).

Dolomite is usually ~200-300 μm in size, slightly rounded and often filled with cracks (Fig. 10 A-D). Dolomite has a 10-100 μm wide ankerite rim, forming euhedral crystals (Fig. 10 A-C). The outer rim of the ankerite is often more enriched in Fe+Mn (due to its higher brightness on the BSE images, Fig. 10 B). 100-200 μm sized calcite grains are

rounded (Fig. 10 A, C, E). Siderite appears as pore filling mineral, usually occurs in larger patches (~500 μm) (Fig. 10 D). These patches are composed of small, zoned siderite grains (~3-5 μm) due to their varying Fe-Mg content (Fig. 10 E). Albite is varying in size (between 50-250 μm), its shape is rounded and often irregular containing cracks as well (Fig. 10. A-C, F). Muscovite sometimes occurs as lithoclast with albite grains (Fig. 10 A). Potassic-feldspar is ~250 μm, and shows rectangular shape, often can contain quartz and albite grains (Fig. 10 A, B, F). Kaolinite appears as 100-200 μm pore filling aggregates in the sandstones (Fig. 10 A, D).

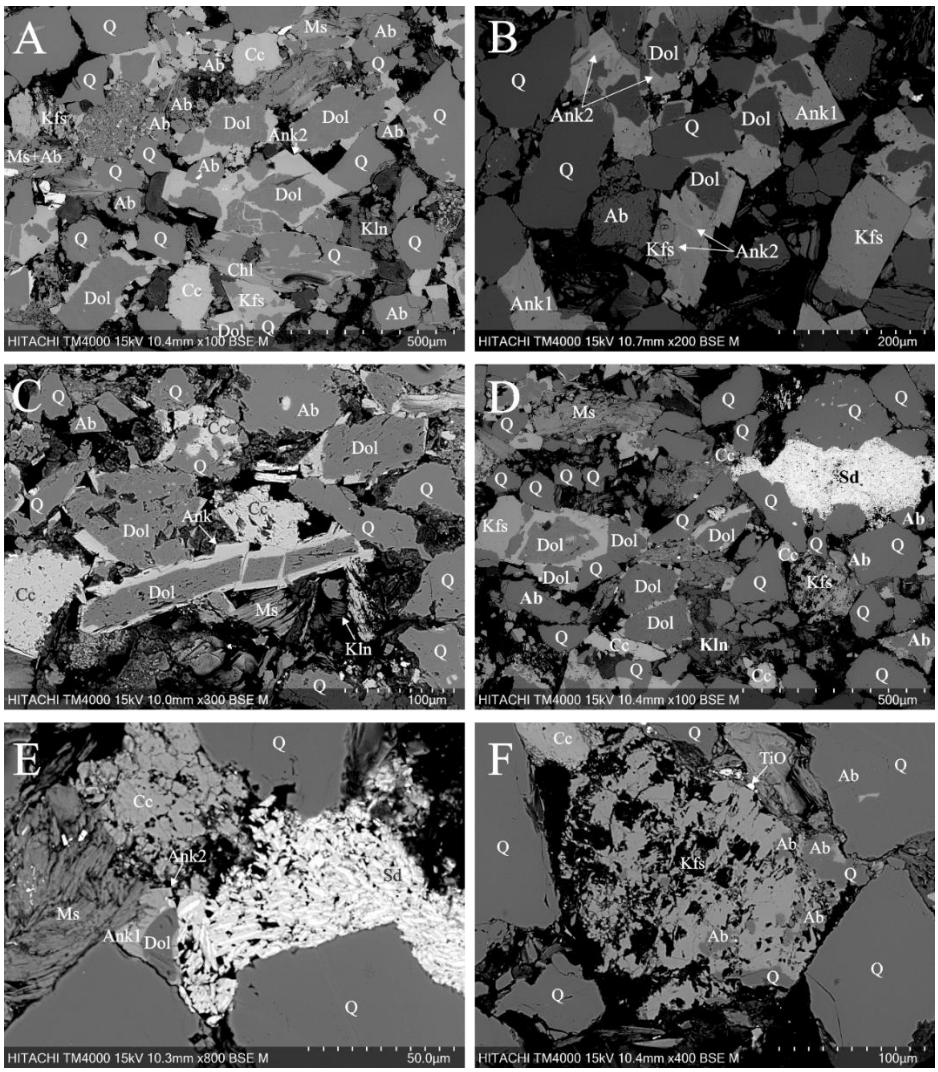

Fig. 10. Backscattered electron images of the sandstone samples from Ölbő.

Abbreviations: Ab: albite, Ank1: ankerite with low Fe-Mn content, Ank2: ankerite with high Fe-Mn content, Cc, calcite, Chl: chlorite, Dol: dolomite, Kfs: K-feldspar, Kln: kaolinite, Ms: muscovite, Q: quartz, Sd: siderite.

The mineral composition of the siltstones based on the XRD result is the following: 21-40 m/m% quartz, 10-33 m/m% mica, 5-16 m/m% plagioclase, 1-7 m/m% K-feldspar, 7-14 m/m% dolomite, 6-15 m/m% calcite, 3-12 m/m% ankerite, <1-5 m/m% siderite (Öl 3-5-2 sample does not contain siderite), 2-9 m/m% chlorite (Öl 1-10 and Öl 2-7B samples do not contain chlorite), 2-8 m/m% kaolinite (Table 12). Pyrite is only present in the Öl 1-10 sample (4 m/m%, Table 12).

Table 12. Mineral composition based on XRD data of the investigated core samples from Ölbő. Values are expressed in m/m %. 1 sigma uncertainty is 1 %. ND: not detected.

Area	Sample	Depth (m)	Sample type	Mica	Kaolinite	Chlorite	Quartz	K-feldspar	Plagioclase	Calcite	Dolomite	Ankerite	Siderite	Pyrite
Ölbő	Öl 1-7	1498-1500	sandstone	7	4	ND	43	4	11	8	11	9	3	ND
	Öl 1-8-1	1520.5-1523	sandstone	8	3	ND	51	4	10	5	11	6	2	ND
	Öl 1-8-2	1520.5-1523	siltstone	20	2	2	28	6	14	10	13	<1	5	ND
	Öl 1-9B1	1561.5-1565.5	sandstone	6	3	5	49	3	9	5	15	5	<1	ND
	Öl 1-9B2	1561.5-1565.5	siltstone	20	3	9	28	7	10	6	14	3	<1	ND
	Öl 1-10	1729.5-1730.5	siltstone	33	8	ND	21	1	5	15	7	6	<1	4
	Öl 2-5	1535-1537.5	sandstone	4	2	ND	58	6	12	3	9	5	1	ND
	Öl 2-7A	1632.5-1637.5	sandstone	12	4	ND	35	4	13	19	6	5	2	ND
	Öl 2-7B	1632.5-1637.5	siltstone	19	3	ND	34	5	10	6	12	6	5	ND
	Öl 3-5-1	1668-1673	sandstone	24	4	ND	30	6	12	3	11	6	4	ND
	Öl 3-5-2	1668-1673	siltstone	10	2	3	40	7	16	<1	10	12	ND	ND
	Öl 6-4A	1682.5-1687.5	sandstone	7	1	4	48	7	13	4	10	6	ND	ND

Based on the previous experiences with the Mihályi-Répcelak samples by Király (2017), the ATR-FTIR analysis of Ölbő samples was carried out. The main aim of the analysis was to check the presence or absence of the OH^--bearing minerals, especially dawsonite in the samples. The strongest O-H stretching vibration of dawsonite can occur at 3275-3280 cm^{-1} (Frost and Bouzaid, 2007). On the Fig. 11., the kaolinite O-H stretching vibration at 3697-3695, 3668-3664, 3621-3619 cm^{-1} is clearly shown, however the dawsonite characteristic O-H stretching vibration at 3275-3280 cm^{-1} is missing from the spectra (more details for the dawsonite IR spectra in the 6.2.4. section). To confirm the absence of dawsonite, the second derivate of the spectra was also checked but dawsonite was not recognizable in the samples.

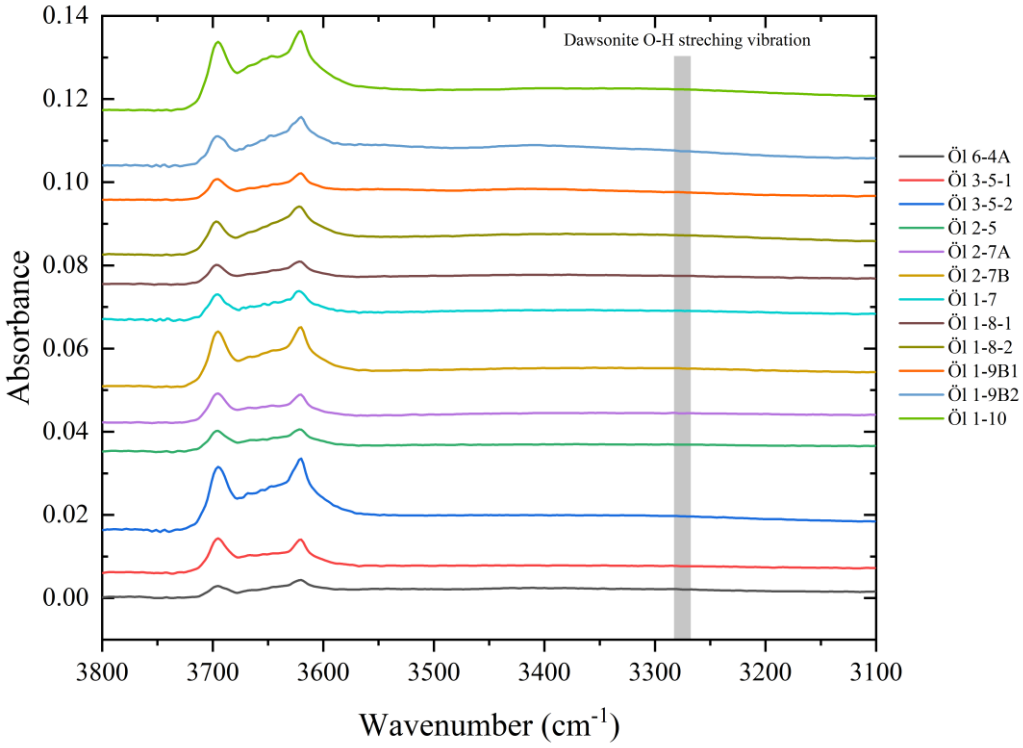

Fig. 11. Infrared (ATR-FTIR) spectra of Ölbő samples in the 3800-3100 cm^{-1} spectral range. The gray rectangle indicates the position of the strongest O-H stretching vibration of dawsonite.

6.2.2. Isotopic composition of the separated carbonates from Mihályi-Répcelak and Ölbő areas

Isotopic composition of separated dawsonite from Mihályi-Répcelak, separated siderite from Mihályi-Répcelak and Ölbő areas, was determined. The $\delta^{13}C_{PDB}$ values of dawsonite vary between +1.5 ‰ and +1.3 ‰, whereas the $\delta^{18}O_{SMOW}$ values range from +19.5 to +22.2 ‰ (Table 13). In contrast, the stable isotope compositions of siderite from Mihályi-Répcelak area show larger variation defining two generational different groups. The siderite $\delta^{13}C_{PDB}$ and $\delta^{18}O_{SMOW}$ values of Group-1 range from +4.2 to +4.3 ‰ and from +24.8 to +25.1 ‰, respectively. Siderite carbon and oxygen isotope compositions of Group-2 are characterized by lower values ($\delta^{13}C_{PDB}$: from +1.3 to +2.1 ‰; $\delta^{18}O_{SMOW}$: from +22.2 to +22.3 ‰; Table 13). The separated siderites from Ölbő show –0.69 ‰ - +1.72 ‰ $\delta^{13}C_{PDB}$ values and +24.12 ‰ - +25.62 ‰ $\delta^{18}O_{SMOW}$ values (Table 13).

Table 13. $\delta^{13}C$ and $\delta^{18}O$ composition of separated dawsonite and siderite from Mihályi-Répcelak and Ölbő. Uncertainty of $\delta^{13}C$ and $\delta^{18}O$ is 0.1 ‰.

Area	Sample name	Separated mineral	$\delta^{13}C$ [PDB, ‰]	$\delta^{18}O$ [PDB, ‰]	$\delta^{18}O$ [SMOW, ‰]
Mihályi	RM6-9R	dawsonite/1	1.6	-11.0	19.5
	RM6-9R	dawsonite/2	1.5	-11.1	19.5
	RM6-9R	siderite/1	2.1	-7.7	23.0
	RM6-9R	siderite/2	1.9	-8.3	22.3
	RM6-7R3	siderite	4.3	-5.6	25.1
	RM6-7R1	siderite	4.2	-5.9	24.8
Répcelak	RM32-5R2	dawsonite	1.3	-8.4	22.2
	RM19-6R	siderite	1.3	-4.9	25.9
Ölbő	Öl 1-7	siderite	1.7	-5.6	25.1
	Öl 1-8-1	siderite	1.1	-5.1	25.6
	Öl 1-9B1	siderite	0.7	-5.4	25.3
	Öl 2-5	siderite	0.0	-5.7	25.0
	Öl 2-7A	siderite	1.7	-6.0	24.7
	Öl 3-5-1	siderite	-0.7	-6.0	24.8
	Öl 6-4A	siderite	1.5	-6.6	24.1

The determined δD values of dawsonite-bearing samples from the Mihályi field cover a narrow range between –61 ‰ and –59 ‰ (Table 14), except for one sample (RM6-9R) that shows a lighter value (–74 ‰). The hydrogen isotope composition of dawsonites from the Répcelak field ranges between –62 ‰ and –57 ‰.

Table 14. δD values of dawsonite from Mihályi-Répcelak field. Uncertainty of δD is 2 ‰.

Area	Sample name	$\delta D_{dawsonite}$ [‰, SMOW]
Mihályi	RM6-9R	-74
	RM6-7R3	-60
	RM6-7R2	-59
	RM6-7R1	-61
Répcelak	RM32-5R2	-57
	RM19-6R	-62

Covasna

6.2.3. Mineral composition of the dawsonite-bearing samples from Covasna

The studied rocks containing dawsonite are breccias, their clasts are sandstones (Fig. 12A), originating from the Cretaceous flysch zone (Dénes et al., 2005). The rocks, sampled along the creek of Hankó Valley (Fig. 3B), are generally fractured, grey-greyish green sandstones with millimetre-wide calcite veins. In some cases the breccias are silicified and covered with clays.

Based on the XRD, the bulk rock is composed of quartz, calcite+Mg-calcite, illite+illite/smectite, muscovite, plagioclase, dawsonite, goethite, chlorite, ankerite, siderite and dolomite. Quartz is between 51 and 83 m/m% except for two samples (KOV-2G/1 and KOV-2G/3) where it is only 31 and 25 m/m%, respectively (Table 15). The host rock samples contain calcite+Mg-calcite (1-34 m/m%), illite+illite/smectite (5-22 m/m%), muscovite (2-22 m/m%), plagioclase (<1-15 m/m%), goethite (<1-12 m/m%),

chlorite (1-7 m/m%), ankerite (1-4 m/m%) and siderite (<1-2 m/m%) (Table 15). Dolomite is only present in two samples (KOV-12/2/1 and KOV-12/2/3), kaolinite only occurs in one sample (KOV-8) (Table 15). The quantity of dawsonite ranges from 1 to 14 m/m% (Table 15). The alumohydrocalcite-bearing KOV-13 sample contains 63 m/m% quartz, 12 m/m% calcite, 10 m/m% muscovite, 7 m/m% chlorite, 5 m/m% illite/smectite, 3 m/m% dolomite and <1 m/m% pyrite (Table 15).

Table 15. Mineral composition of the bulk rock and separated alumohydrocalcite (KOV-13 Ahcal) from Covasna. Values are expressed in m/m%. ND: not detected.

Rock sample	muscovite	illite+illite/smectite	kaolinite	chlorite	quartz	plagioclaise	calcite+Mg-calcite	dolomite	ankerite	siderite	dawsonite	goethite	pyrite	alumohydrocalcite
KOV-8	6	ND	2	ND	71	4	11	ND	1	2	3	<1	ND	ND
KOV-10	3	ND	ND	ND	72	<1	7	ND	1	1	4	12	ND	ND
KOV-10/1	3	ND	ND	ND	69	<1	16	ND	2	1	2	7	ND	ND
KOV-12	2	5	ND	1	83	3	3	ND	2	<1	1	ND	ND	ND
KOV-12/2/1	9	21	ND	6	51	8	ND	2	ND	<1	3	ND	ND	ND
KOV-12/2/3	8	22	ND	5	53	8	ND	1	ND	ND	3	ND	ND	ND
KOV-2G/1	19	16	ND	7	31	15	3	ND	4	ND	5	ND	ND	ND
KOV-2G/2	4	7	ND	2	73	5	6	ND	2	ND	1	ND	ND	ND
KOV-2G/3	22	ND	ND	7	25	10	19	ND	3	ND	14	ND	ND	ND
KOV-2G/4	5	ND	ND	3	70	2	18	ND	1	ND	1	<1	ND	ND
KOV-2G/5	6	ND	ND	1	55	1	34	ND	2	ND	1	<1	ND	ND
KOV-2B/1	4	12	ND	3	67	7	1	ND	3	ND	3	ND	ND	ND
KOV-13	10	5	ND	7	63	ND	12	3	ND	ND	ND	ND	<1	ND
KOV-13 Ahcal	ND	ND	ND	ND	10	ND	ND	ND	ND	ND	ND	ND	ND	90

Dawsonite appears as a white, fibrous mineral with silky lustre (Fig. 12B) and also occurs as fine fibrous or powdery aggregates. It covers the breccia surface and appears along the small fractures and cracks of the brecciated sandstone (Fig. 12C-D). It can fill the small fractures and the cracks in the studied rocks (Fig. 13A-B), and it can also form large patches ~1500 μm in size (Fig. 13A) and approximately 50 μm long fibres (Fig. 13 C and D). Dawsonite crystals intermix with other carbonates, e.g., siderite (Fig. 13C) and calcite (Fig. 13D). Dawsonite and calcite can appear in close textural relationship with each other, where dawsonite needles are growing into the calcite crystals (Fig. 13D). Additionally, dawsonite appears powdery on the surface of rocks and fluvial deposits in the creek (Fig. 12E-F).

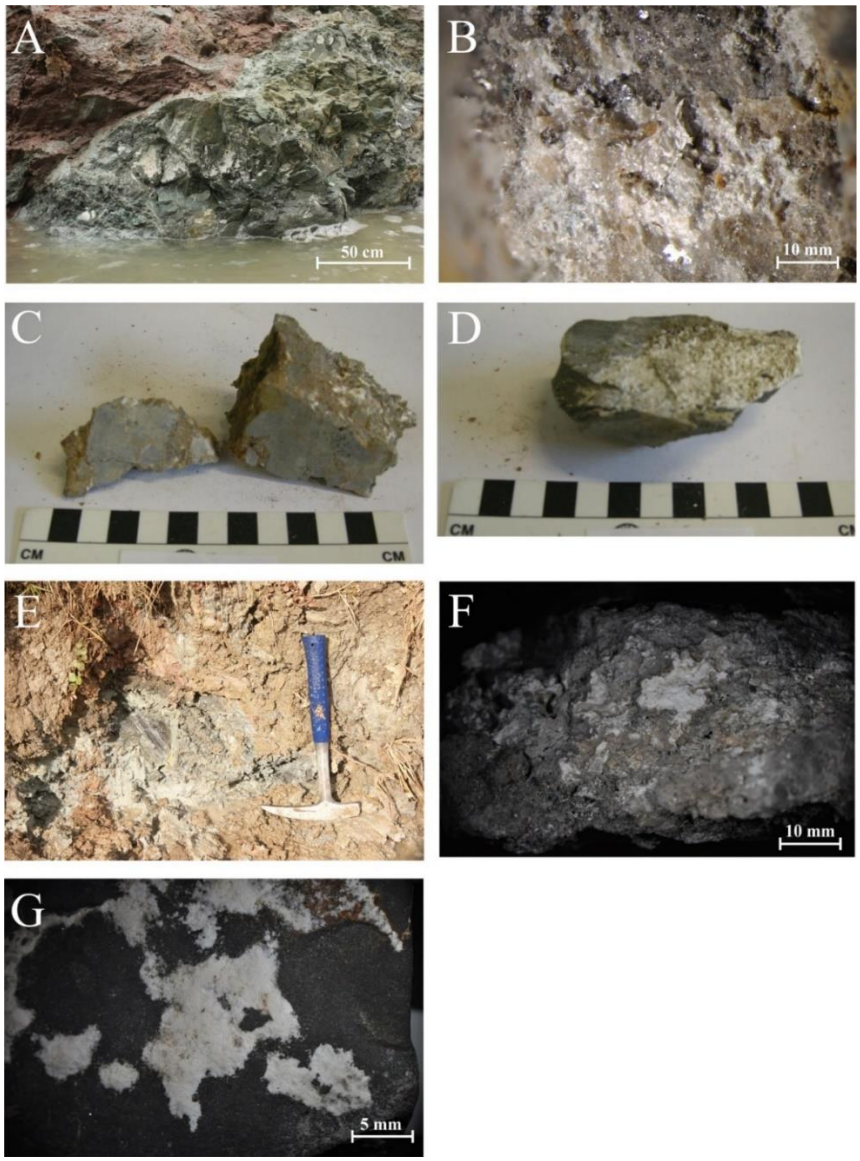

Fig. 12. Appearance of dawsonite and alumohydrocalcite. A: Dawsonite appearance (white patches) on the brecciated sandstone along the creek of Hankó Valley, B: White dawsonite fibers under the stereomicroscope, C: Dawsonite appears in the crack of the brecciated sandstone, D: Dawsonite covers the brecciated sandstone's surface, E-F: Powdery dawsonite appearance on surface of the fluvial deposit, G: Alumohydrocalcite (white) patches on the rock surface.

Calcite appears as radial crystals (Fig. 13E) and in veins. Siderite occurs as rhombohedral crystals (Fig. 13F) and is usually observed along the edges of quartz or calcite crystals (Fig. 13A-B). Anatase (Fig. 13G) and pyrite can occur as minor constituents, and realgar is also present in the calcite veins (Fig. 13 E and H). Realgar usually appears in close textural relationship with calcite (Fig. 13H-E).

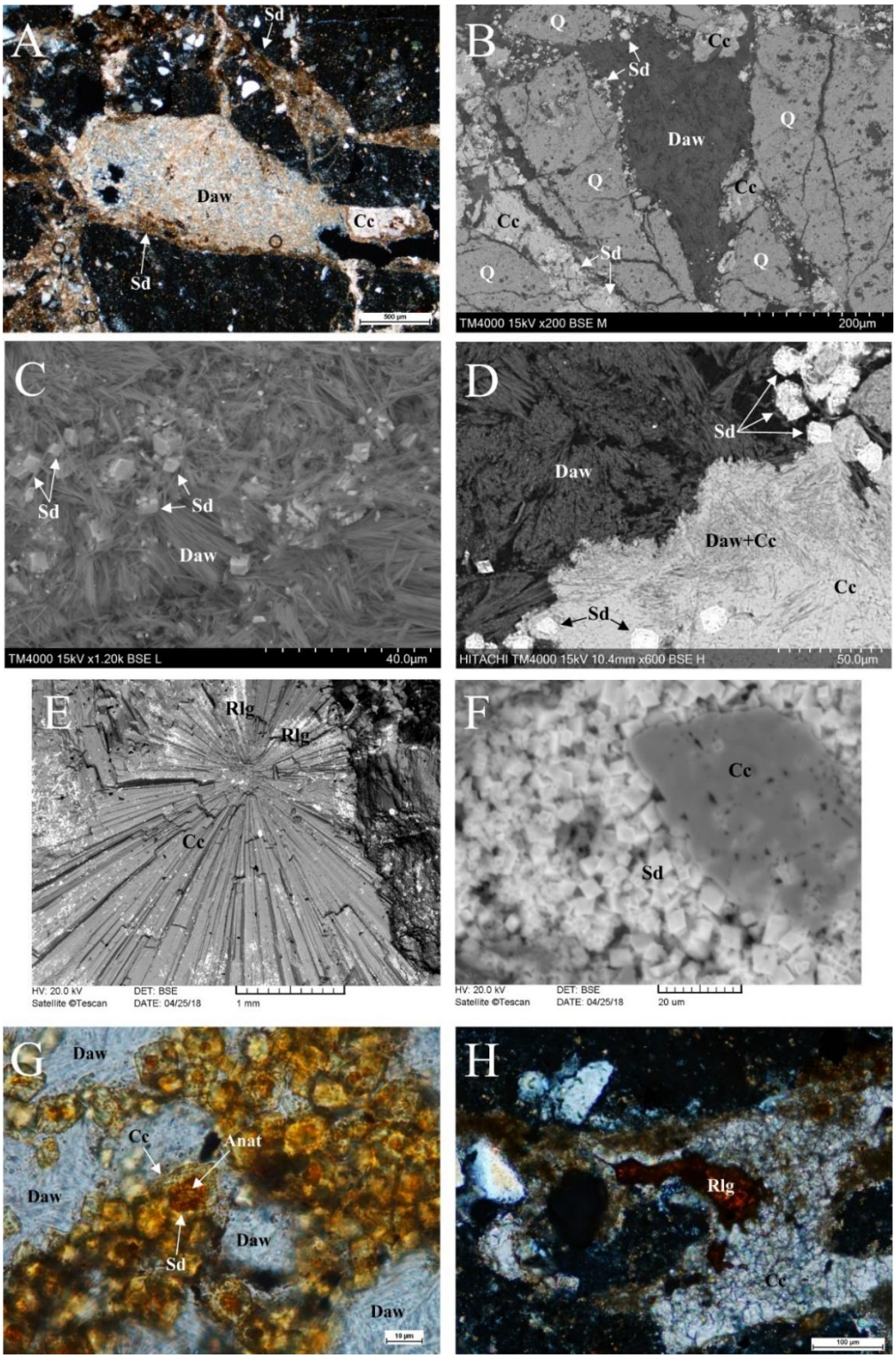

Fig. 13. Dawsonite-bearing brecciated sandstone from Covasna. A: Dawsonite patch (microphotograph, +N), B: Dawsonite and siderite with calcite as fracture filling materials in quartz grains (BSE image), C: Rhombohedral siderite crystals within fibrous dawsonite (BSE image), D: Dawsonite and calcite aggregates, containing rhombohedral siderite crystals (BSE image), E: Realgar on radial calcite crystals (BSE image), F: Aggregates of rhombohedral siderite crystals with calcite (BSE image), G: Aggregates of dawsonite, anatase and minor calcite (microphotograph, 1N), H: Realgar in a calcite aggregate (microphotograph, +N). Abbreviations: Anat: anatase, Cc: calcite, Daw: dawsonite, Rlg.: realgar, Q: quartz, Sd: siderite.

The presence of alumohydrocalcite [$CaAl(CO_3)_2(OH)_4 \times 4H_2O$] was proved in the KOV-13 sample by XRD, ATR-FTIR and Raman spectroscopy (Fig. 14-16, Table 15). The alumohydrocalcite only appears on the surface of the sample, the separated alumohydrocalcite (90 m/m%) occurs with quartz (10 m/m%) (Fig. 14, Table 15). Alumohydrocalcite forms white, needles or columnar like crystals and it generally appears together with quartz (Fig. 12G). This is the first description of alumohydrocalcite from Covasna.

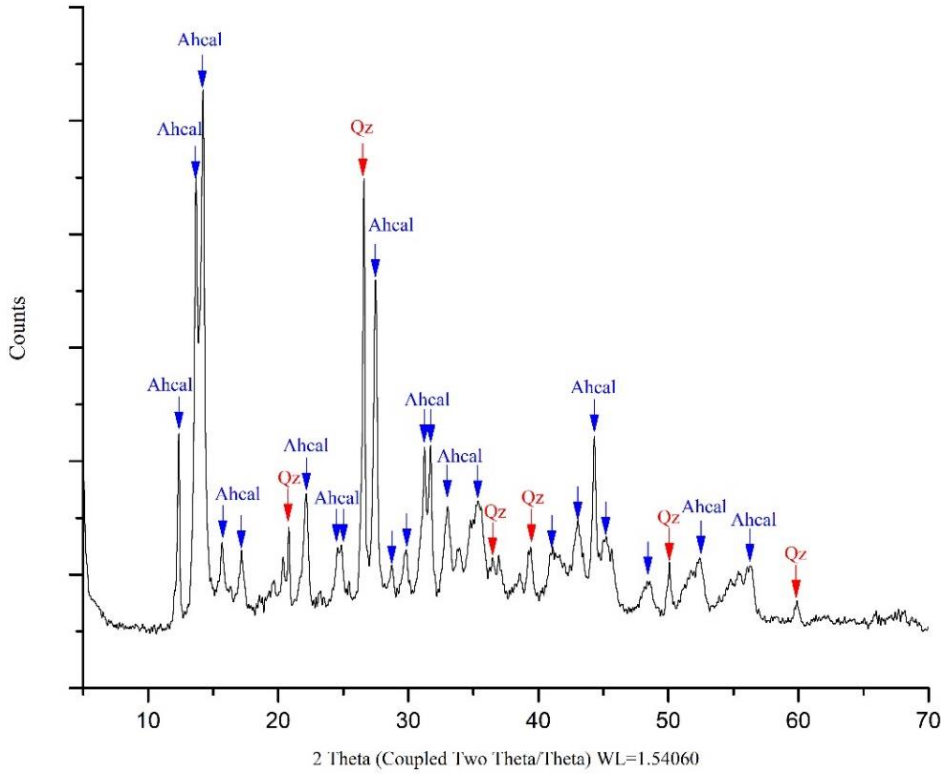

Fig. 14. X-ray diffractogram of separated alumohydrocalcite and quartz (KOV-13 Ahcal). Ahcal: alumohydrocalcite, Qz: quartz.

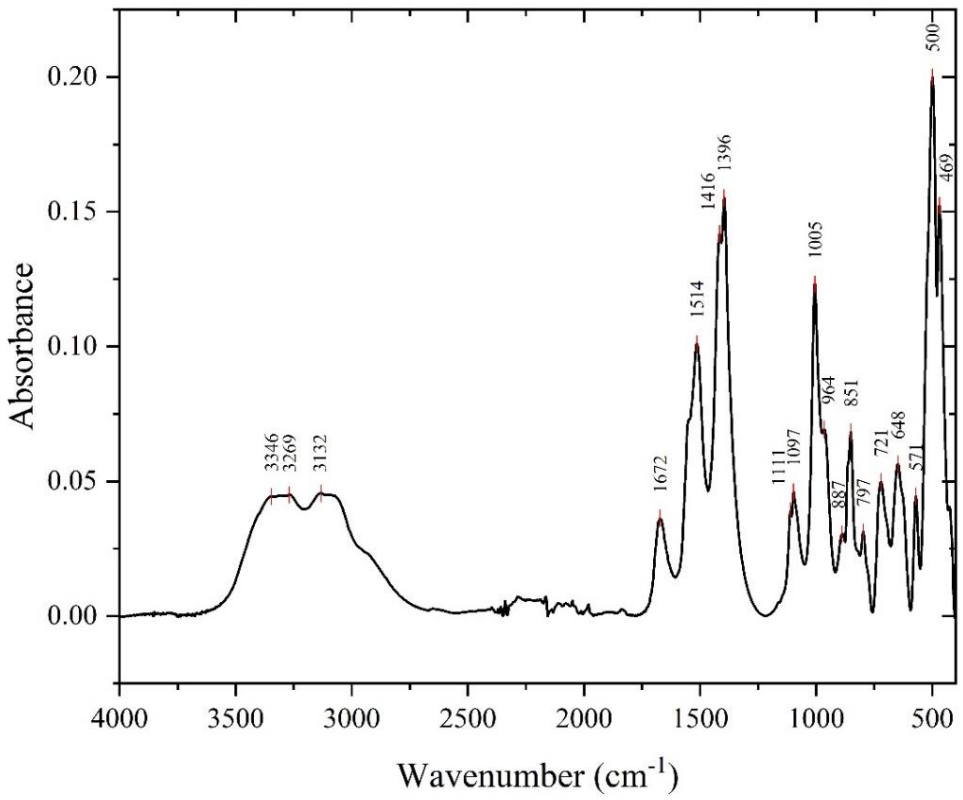

Fig. 15. Infrared spectrum (ATR-FTIR) of separated alumohydrocalcite (KOV-13 Ahcal) in the 4000-400 cm^{-1} spectral range.

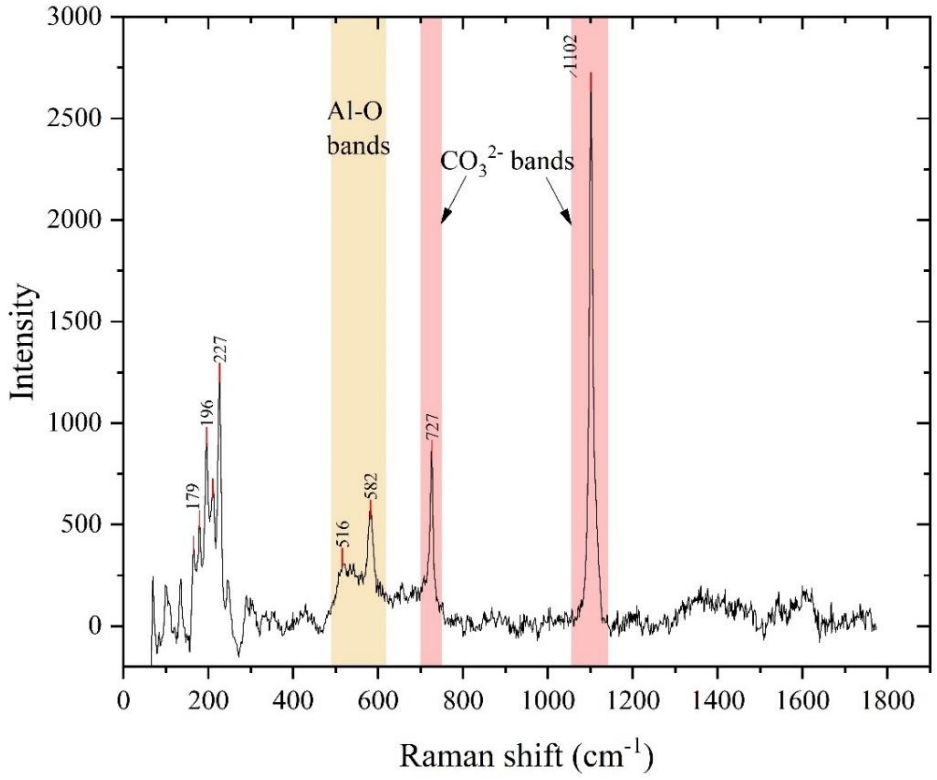

Fig. 16. Raman spectrum of alumohydrocalcite (KOV-13 Ahcal) in the 100-1800 cm^{-1} range.

6.2.4. Dawsonite, calcite and alumohydrocalcite separates

Micro-XRD of dawsonite and calcite

Separated dawsonite and calcite were measured by micro-XRD analysis to verify the purity of the separation. Most of the dawsonite separates contain 70-100 m/m% dawsonite, 9 samples out of the 13 contain 1-15 m/m% calcite, 4-15 m/m% quartz, one sample contains 4 m/m% feldspar, whereas clay minerals are present in only two separates (Table 16). Calcite separates (KOV-10/1 Cc) contain only calcite.

Table 16. Micro-XRD data on the separated dawsonite and calcite samples in m/m%. Daw: dawsonite, Cc: calcite, ND: not detected. Note that almost each separate contains quartz and calcite.

Rock sample	Separated phase	Dawsonite	Calcite	Quartz	Feldspar	Clay mineral
KOV-8	Daw	100	ND	ND	ND	ND
KOV-10	Daw	90	3	7	ND	ND
KOV-10/1	Daw	70	10	20	ND	ND
KOV-12	Daw	90	5	5	ND	ND
KOV-12/2/1	Daw	70	15	14	ND	ND
KOV-12/2/2	Daw	80	1	10	ND	9
KOV-12/2/3	Daw	85	ND	15	ND	ND
KOV-2G/1	Daw	85	5	4	4	2
KOV-2G/2	Daw	95	5	ND	ND	ND
KOV-2G/3	Daw	95	5	ND	ND	ND
KOV-2G/4	Daw	90	5	5	ND	ND
KOV-2G/5	Daw	86	6	8	ND	ND
KOV-2B/1	Daw	95	5	ND	ND	ND
KOV-10/1 Cc	Cc	ND	100	ND	ND	ND

Infrared spectroscopy (ATR-FTIR) of dawsonite

Infrared spectroscopy of the separated dawsonite samples was carried out before the hydrogen isotope measurements. The two most intensive bands of dawsonite occur at 1391-1393 cm^{-1} and 1570-1580 cm^{-1}, which correspond to the asymmetric stretching of CO_3^{2-}, whereas the bands at 3271-3273 cm^{-1} belong to the O-H stretching vibration (Fig. 17). The dawsonite ATR-FTIR spectra also show the OH-Al bending at ~950 cm^{-1} and the other CO_3^{2-}-bending at 1090-1100, 863, 846, 731 and 685-690 cm^{-1} (Fig. 17). Some harmonics and external stretching were also observed at 1722, ~539 and ~495 cm^{-1} (Fig. 17). The measured bands of dawsonite fall in the spectral range (1390-1400, 1550-1588 and 3275-3280 cm^{-1}) and agree with previously reported data on dawsonite (e.g., Frueh and Golightly, 1967; Estep and Karr (1968), Serna et al. (1985), Frost and Bouzaid (2007).

In 6 rock samples (KOV-12/2/1, KOV-12/2/2, KOV-12/2/3, KOV-2B/1, KOV-2G/1, KOV-2G/2), bands appear at 1164-1166, 799-801, 779-780 cm^{-1} in the ATR-FTIR spectra (Fig. 17), which is related to the Si-O band of quartz (Van der Marel and Beutelspacher, 1976; Hlavay et al., 1978). However, typical calcite vibration (e.g., 712-713 cm^{-1}; Farmer, 1974; Vaculíková and Plevová, 2005; Van der Marel and Beutelspacher, 1976) was not detected on the ATR-FTIR spectra, in contrast to the micro-XRD results (Table 16).

The ATR-FTIR spectra clearly showed that the typical dawsonite OH^- band (~3270 cm^{-1}) disappeared in the samples after the hydrogen isotope measurements, therefore the elimination of dawsonite OH^- group was successful (Fig. 17).

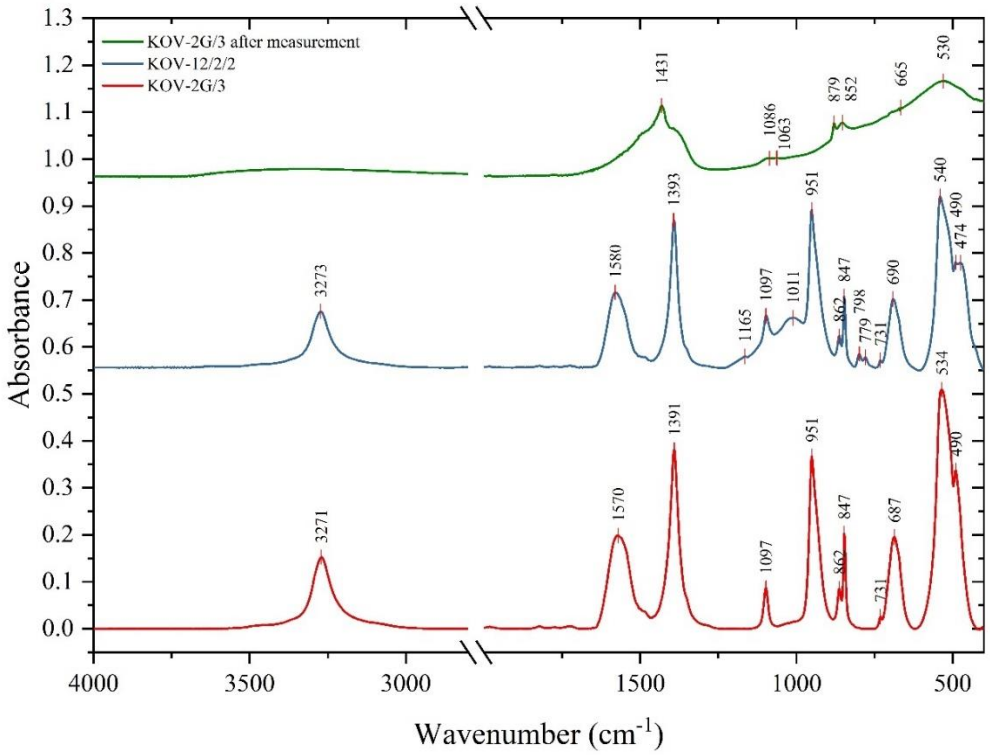

Fig. 17. Infrared spectra (ATR-FTIR) of separated dawsonite in the 4000-400 cm^{-1} spectral range. Red color (KOV-2G/3 sample) shows dawsonite spectra, blue color (KOV-12/2/2) shows dawsonite spectra with quartz before the hydrogen isotope measurements, and green color (KOV-2G/3 after measurement) indicates the sample after the hydrogen isotope measurement.

Raman microspectroscopy of dawsonite

Raman microspectroscopy was applied on the surface of the rocks, before the separation to identify dawsonite. The spatial resolution of Raman microspectroscopy is much higher than the ATR-FTIR and XRD analyses, therefore single dawsonite fibres

were analysed. The typical O-H stretching vibrations of dawsonite occur at around 3285 and 3254 cm^{-1}, 898 and 825 cm^{-1} Raman shifts (Fig. 18). Bands of CO_3^{2-} appear at 1506, 1092, 1069 and 730 cm^{-1}, Al-O stretching vibration bands are observed near 588, 518, 389 cm^{-1} and the external vibrations at 262, 219, 192, 153 cm^{-1} (Fig. 18). The Raman spectra of the dawsonite in this study are very similar to those of reported data (Frost and Bouzaid, 2007; Frost et al., 2015; Serna et al., 1985).

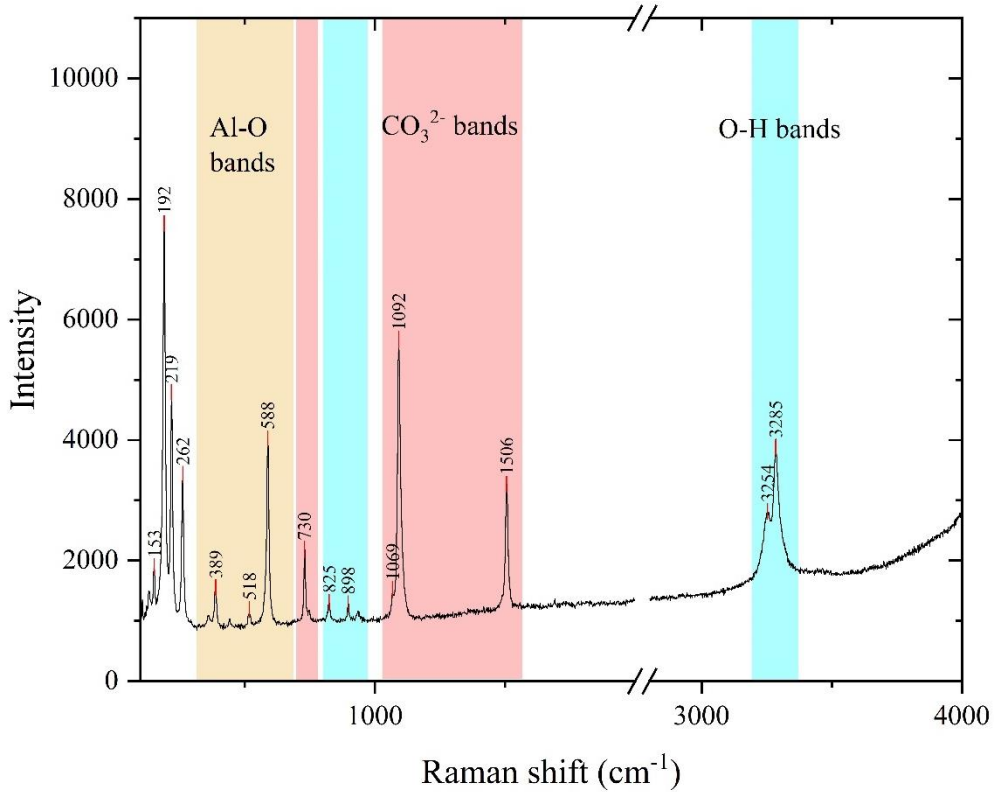

Fig. 18. Raman spectrum of separated dawsonite (KOV-2G/4) over the 100-4000 cm^{-1} range.

6.2.5. Stable isotope composition of separated dawsonite

The $\delta^{13}C$ values of dawsonite are between +8.0 ‰ and +10.1 ‰, the $\delta^{18}O$ values of dawsonite fall between the +40.7 and +46.7 ‰ range (Table 17). The measured δD values of dawsonite range from –55 to –42 ‰ (Table 17).

Table 17. $\delta^{13}C$ and $\delta^{18}O$ data of dawsonite and calcite, and δD data of dawsonite from Covasna. Uncertainty of $\delta^{13}C$ and $\delta^{18}O$ are 0.1‰, for δD is 2‰. Daw: dawsonite, Cc, calcite, NM: not measured.

Rock sample	Separated phase	$\delta^{13}C$ [‰, PDB]	$\delta^{18}O$ [‰, SMOW]	δD [‰]
KOV-8	Daw	8.6	44.2	-54
KOV-10	Daw	8.1	40.7	-55
KOV-10/1	Daw	8.3	44.1	-53
KOV-12	Daw	8.0	44.6	-48
KOV-12/2/1	Daw	9.1	44.8	-47
KOV-12/2/2	Daw	8.4	43.1	-50
KOV-12/2/3	Daw	10.0	45.2	-46
KOV-2G/1	Daw	9.4	44.9	-44
KOV-2G/2	Daw	8.4	45.0	-42
KOV-2G/3	Daw	10.1	46.1	-43
KOV-2G/4	Daw	8.2	45.7	-45
KOV-2G/5	Daw	9.0	46.7	-48
KOV-2B/1	Daw	8.1	44.5	-47
KOV-10/1 Cc	Cc	-1.5	24.0	NM

6.2.6. Chemical and stable isotope composition of creek and spring water

Chemical analyses were carried out only on two water samples: K-AU21-1 represents the creek water, whereas K-AU21-2 stands for the spring water (Table 18). These two samples show considerable differences in every value (Table 18). The creek water pH is higher (7.55) than the spring water (6.89). The major ions concentrations in the creek water sample (e.g., Na^+, Cl^- and HCO_3^-) are considerably lower than in the spring water (Table 18).

Table 18. Chemical composition of creek (K-AU21-1) and spring (K-AU21-2) water. The units are the following: EC is µS/cm, for the major elements is mg/L, for trace elements (*in italic*) is µg/L.

	K-AU21-1 (creek)	K-AU21-2 (spring)
pH	7.55	6.89
EC	2010	16460
Na^{+}	320	4037
K^{+}	11.7	168
Ca^{2+}	82.4	73.7
Mg^{2+}	20.9	102
Fe^{2+}	0.187	0.655
Al^{3+}	29.9	2
NH^{4+}	0.22	<0.1
Mn^{2+}	0.12	0.0155
Cl^{-}	247	2370
NO_3^{-}	2.07	<0.1
NO_2^{-}	<0.1	<0.1
HCO_3^{-}	866	8662
CO_3^{2-}	<0.3	<3.0
PO_4^{3-}	<0.15	0.21
SO_4^{2-}	32.3	3.09
OH^{-}	<0.1	<0.1
H_2SiO_3	15	45.9
TDS	1598	15463
As	128	391
B	13065	162368
Ba	133	778
Cd	<5.0	<5.0
Cu	<5.0	<1.0
Li	601	8377
Sr	455	654

The isotopic compositions of all collected water samples are summarized in Table 19. The hydrogen (δD) and oxygen ($\delta^{18}O_{SMOW}$) stable isotope compositions of the creek water samples vary from –79.7 ‰ to –56.8 ‰, and from –10.9 ‰ to –7.4 ‰, respectively (Table 19). The δD values of spring water show heavier isotope compositions relative to creek water, varying between –50.9 ‰ and –48.4 ‰. The oxygen isotope values are also characterized by heavier isotopic data ranging from –0.1 ‰ to +2.5 ‰ (Table 19).

Temperature of the creek and spring water were also measured during the 7 month-monitoring. The temperature of the creek water shows relatively large variation, varying from 1 °C to 22 °C as a consequence of the sampling time (Table 19).

Table 19. δD and $\delta^{18}O$ values of collected creek and spring water samples. Uncertainty of δD and $\delta^{18}O$ are 1‰ and 0.15‰, respectively. NM: not measured. Sample name refers to location, month and year of collection, the number 1 and 3 (or 3') represent the creek water from two different sampling points, number 2 indicates the spring water.

Water sample	Date of the sampling	GPS coordinates	Water type	Temperature [˚C]	δD_{water} [‰, SMOW]	$\delta^{18}O_{water}$ [‰, SMOW]
K-M18-1	March 2018	N 45°51'10.48" E 26°12'15.55"	creek	NM	-72.1	-9.1
K-M18-2		N 45°51'12.06" E 26°12'18.65"	spring	NM	-50.5	-0.1
K-A19-1	April 2019	N 45°51'10.48" E 26°12'15.55"	creek	21	-73.5	-10.1
K-A19-2		N 45°51'12.06" E 26°12'18.65"	spring	9	-49.6	2.1
K-A19-3		N 45°51'12.29" E 26°12'23.13"	creek	18.5	-74.1	-10.2
K-J20-1	January 2020	N 45°51'10.48" E 26°12'15.55"	creek	1	-73.4	-9.6
K-J20-2		N 45°51'12.06" E 26°12'18.65"	spring	8	-48.4	2.7
K-J20-3		N 45°51'12.29" E 26°12'23.13"	creek	1	-73.0	-10.0
K-F20-1	February 2020	N 45°51'10.48" E 26°12'15.55"	creek	4	-79.4	-10.6
K-F20-2		N 45°51'12.06" E 26°12'18.65"	spring	8	-50.6	2.2
K-F20-3		N 45°51'12.29" E 26°12'23.13"	creek	4	-79.7	-10.9
K-M20-1	March 2020	N 45°51'10.48" E 26°12'15.55"	creek	7	-76.5	-10.5
K-M20-2		N 45°51'12.06" E 26°12'18.65"	spring	8	-49.1	2.1
K-M20-3		N 45°51'12.29" E 26°12'23.13"	creek	7	-76.1	-10.5
K-A20-1	April 2020	N 45°51'10.48" E 26°12'15.55"	creek	11	-73.7	-9.9
K-A20-2		N 45°51'12.06" E 26°12'18.65"	spring	8	-49.9	2.5
K-A20-3		N 45°51'12.29" E 26°12'23.13"	creek	11	-73.4	-9.9
K-MY20-1	May 2020	N 45°51'10.48" E 26°12'15.55"	creek	12	-56.8	-7.4
K-MY20-2		N 45°51'12.06" E 26°12'18.65"	spring	10	-50.0	2.2
K-MY20-3'		N 45°51'12.29" E 26°12'23.13"	creek	11	-64.3	-8.7
K-J20-1	June 2020	N 45°51'10.48" E 26°12'15.55"	creek	21	-69.1	-9.6
K-J20-2		N 45°51'12.06" E 26°12'18.65"	spring	12	-50.9	1.8
K-J20-3		N 45°51'12.29" E 26°12'23.13"	creek	18	-68.4	-9.7
K-JL20-1	July 2020	N 45°51'10.48" E 26°12'15.55"	creek	22	-62.1	-8.7
K-JL20-2		N 45°51'12.06" E 26°12'18.65"	spring	13	-48.9	2.2
K-JL20-3		N 45°51'12.29" E 26°12'23.13"	creek	19	-63.1	-9.0
K-JL20-3'		N 45°51'12.29" E 26°12'23.13"	creek	20	-62.8	-8.9
K-AU21-1	August 2021	N 45°51'10.48" E 26°12'15.55"	creek	NM	-60.0	-7.7
K-AU21-2		N 45°51'12.06" E 26°12'18.65"	spring	NM	-48.8	2.2

6.2.7. Calcite stable and clumped isotope results

The isotope composition $\delta^{13}C$ and $\delta^{18}O_{SMOW}$ from the separated calcite of KOV-10/1 cc sample is -1.50 ‰ and +24.04 ‰, respectively (Table 17). Calcite $\Delta_{47(I\text{-}CDES90)}$ value is 0.3787 ±0.0289 ‰ (Table 20 and S2), the calculated temperature by Anderson equation is 143 °C (Table 20, Anderson et al., 2021).

Table 20. Average of Δ_{47} values of separated calcite (KOV-10/1 cc) and Δ_{47}-temperature calibration by Anderson et al. (2021). SD: standard deviation, SE: 1σ standard error, ND: not determined.

	Value	$\Delta(\Delta_{47})$	±1SD	±1SE	Equation
Δ_{47} [I-CDES90°C]	0.3738 ‰	ND	0.0289	0.0077	
Anderson Temperature	143 °C	-920.80	ND	7	$\Delta_{47(I-CDES90°C)} = 0.0391(\pm 0.0004) * \frac{10^6}{T^2} + 0.154\ (\pm 0.0004)$ r^2=0.97

7. Discussion

Different geological environments (Mihályi-Répcelak, Ölbő, Covasna) were investigated to better understand the formation of dawsonite. The applicability of sequential acid extraction method was tested to determine the isotopic composition of carbonates. The presented petrographical results, geochemical parameters, and isotopic result (C, O, H) of natural carbonates are discussed in the following sections to determine the origin of the parental fluid (CO_2 and H_2O) of dawsonite. In addition, geochemical modelling was applied to understand the formation of dawsonite and constrain the reactions which can take place during a CO_2 storage project in sandstone reservoir.

7.1. Sequential acid extraction method

Since the 1960's many publications focused on the sequential acid extraction of carbonates with off-line and on-line method as well (Al-Aasm et al., 1990; Baudran et al., 2012; Epstein et al., 1964; Ray and Ramesh, 1998; Yui and Gong, 2003; Walters 1972). However, these studies mostly investigated the calcite-dolomite SEA. Clayton et al. (1968a, b) and Walters et al (1972) emphasized the effect of grain size and temperature during phosphoric acid reaction and demonstrated that substantial fraction of the dolomite was dissolved in the first hour of reaction in the case of the smaller grain size (Table S3). Al-Aasm et al. (1990) suggested a three-step procedure, for calcite-dolomite mixture at 25 °C and 50 °C, with a step in-between when pumping out the CO_2 (Table S3). Ray and Ramesh (1998) have also developed a method to reduce the grain size effect and efficiently separate CO_2 from pure end-members without any significant mixing. Yui and

Gong (2003) found that nonstoichiometric calcite-rich dolomite reacts more easily with the phosphoric acid. These observations might question the usage of the acid extraction method on partially dolomitized samples. In addition, it was not advised to compare the published isotopic data of coexisting dolomite and calcite if the grain size and the stoichiometry of dolomite were not considered (Yui and Gong, 2003). Baudrand et al. (2012) used mass balance equation to determine the isotopic composition of dolomite in a calcite-dolomite mixture (Table S3). Most recent studies (Du and Song, 2020; Liu et al., 2019) try to optimize the pre-treatment conditions and introduce a whole workflow to reduce the interference from dolomite. Liu et al. (2019) concluded that the isotopic ratios of calcite are unavoidably affected by simultaneous reactions of dolomite with phosphoric acid, even at 25 °C (Liu et al., 2019). Du and Song (2020) modified the procedure and tested it at low temperature (2 °C), because dolomite is immediately digested at 25 °C (Table S3). Du and Song (2020) explained that the traditional SAE method produces (25 °C) at least three times more contamination from dolomite than at 2 °C.

Morera-Chavarría et al. (2016) investigated the reaction rate of siderite as well beside calcite and dolomite under different pH and temperature conditions, considering both grain size and the used acid, later validating with different natural samples (Table S3). Chloroacetate buffer was applied for calcite digestion and maleate solution was used for dolomite. Siderite was dissolved completely with both organic solutions.

The above introduced studies show that SEA method can still be used in a simple system like calcite-dolomite. However, a special care is needed and attention to the grain size, composition and crystallinity of the carbonates, beside the acid and temperature used.

Beside of simple system like dolomite-calcite, the SEA is widely used to determine the stable isotope composition of rock samples containing more than two carbonates (Al-Aasm et al., 1990; Epstein et al, 1964; Liu et al., 2011). Most recent one, Liu et al. (2011) reacted whole sandstone samples (containing calcite, dawsonite, ankerite) with 100% orthophosphoric acid at 25°C for 6 h, 24h and 48 h to extract the CO_2 from carbonates for carbon and oxygen isotope analysis. 6 h reaction time was used for calcite, 24 h dissolution time was applied for dawsonite (based on Baker et al., 1995) and 48 h for ankerite.

Moreover, to use the SEA method on a bulk rock arises more questions and the meaning of the yielded isotopic result is even more ambiguous. Therefore, series of experiments were conducted on pure phases and bulk rock samples.

7.1.1. Applicability of selective acid extraction (SAE) of pure carbonates

The majority of calcite (~80 %) was dissolved in the first hour of the experiment (Fig. 4). The difference in $\delta^{13}C$ and $\delta^{18}O$ values in the first hour (1.69 ‰ and 19.53 ‰, respectively) and when the derived CO_2 reached the maximum value ($\delta^{13}C$: 1.63 ‰ and $\delta^{18}O$: 19.50 ‰ in the 36. hour) are in the range of the measurement error (0.1 ‰). In agreement with Liu et al. (2011), 6 h is sufficient at 25 °C for calcite dissolution, but it is also worth to note that 1 hour of reaction time can already give a representative information. To compare, Al-Aasm et al. (1990) determined 2 hours, meanwhile Liu et al. (2019) 45 min for calcite at 25 °C, with grain size of <75 μm or 75-80 μm, respectively. Extracted CO_2 gas from dawsonite reached its maximum after 6 h of dissolution, but more than 90 % of dawsonite dissolved in the first hour (Fig. 5). The proposed reaction time (24 hours, Baker et al., 1995; Liu et al, 2011) for dawsonite is probably too long, it can give reliable results after 1 hour. Al-Aasm et al. (1990) reported representative isotopic results for dolomite after 24 h reaction time at 25 °C. On the other hand, CO_2 yield from dolomite reached its maximum after 48 h dissolution at 25 °C in the experiments, while ~70 % of dolomite reacted in the first 6 hours (Fig. 6). Ankerite started to dissolve in the first hour (Fig. 7), but the CO_2 yield reached its maximum in the 36th hour, while ~80 % of ankerite was dissolved after 12 hours. According to these results, 48 hour dissolution (Liu et al., 2011) at 25 °C is not required to determine ankerite's carbon and oxygen isotope composition. Siderite was not investigated by Liu et al. (2011) work, but both study sites (Mihályi-Répcelak and Ölbő) contain siderite, therefore this mineral was also included in the sequential dissolution experiments. After 24 hours (Fig. 8) siderite started to dissolve, and measurable CO_2 gas could be extracted. This observation is important if the studied samples contain siderite beside of the above mentioned carbonates. Experimental results on the pure phases indicate that after one hour calcite, dawsonite and ankerite show different rate of dissolution.

7.1.2. Testing the SAE method on artificial mixtures and natural samples

According to Liu et al. (2011), the isotopic composition should be representative for calcite after 6 hours reaction time, for dawsonite after 24 hours and for ankerite after 48 hours dissolution time. The artificial mixtures, which contain different amount of the investigated carbonates were also measured by the same method, with varying dissolution times. ME1 sample mainly contains calcite (40 %) and dolomite (30 %) but ankerite (15

%), dawsonite (10 %) and siderite (5 %) are also present. The ME2 sample is ankerite-(35 %) and dolomite-rich (30 %), however contains 15 % calcite and 10-10 % dawsonite and siderite as well. ME3 sample contains only three carbonate phases, 40-40 % calcite and ankerite, and 20 % dawsonite. Comparing the isotopic composition of the artificial mixtures and the pure phases, it is clearly shown that the results of artificial mixtures are not approaching neither the isotopic values of calcite after 6 hours of dissolution, nor the dawsonite's isotopic composition after 24 hours of dissolution (Fig. 19). The isotopic composition of calcite dominated samples (ME1 and ME3) are closer to the pure calcite than the ankerite dominated ME2 sample, but the influence of all carbonates is recognizable (Fig. 19). The ankerite dominated samples (ME2, ME3) are closer to the ankerite isotopic composition after 24 and 48 hours but the siderite isotopic signature may also influence it (Fig. 19). These results show that the carbonate ratios have a significant effect on the isotopic composition of the mixtures, so it is not negligible when the bulk sample contains more than two carbonate phases.

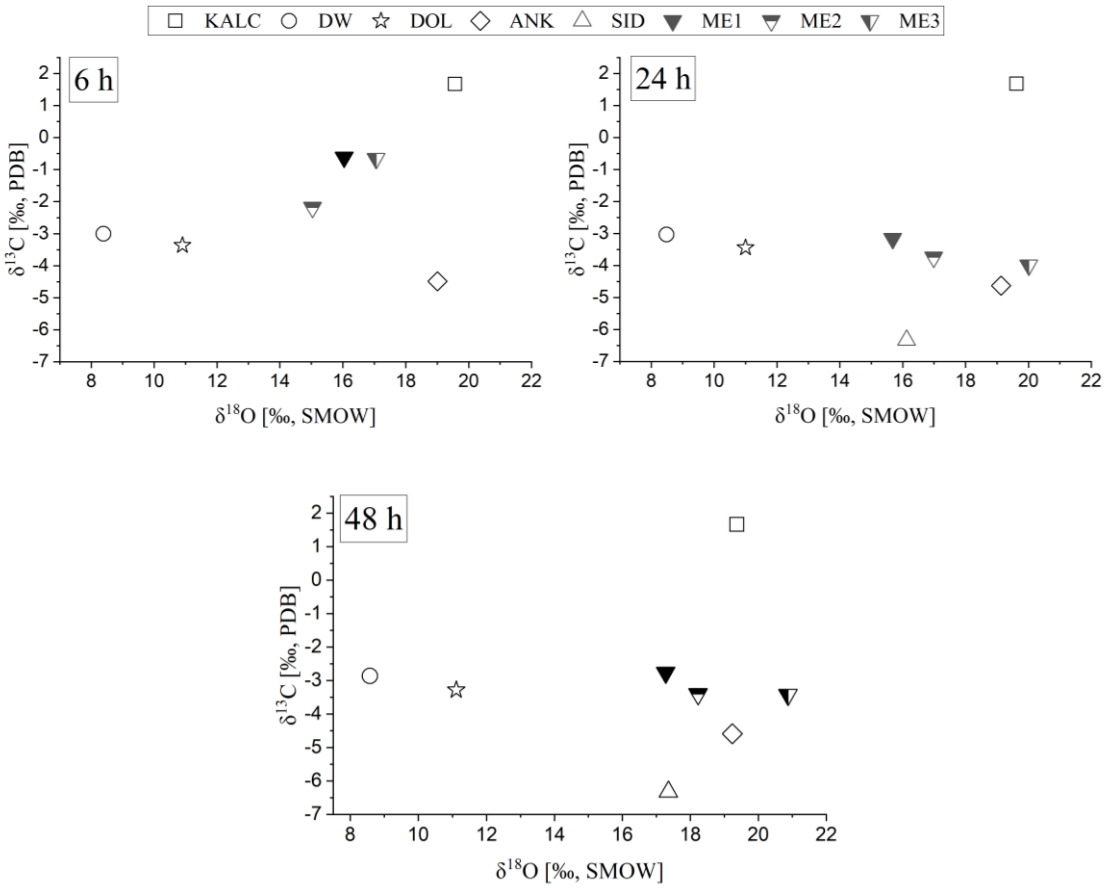

Fig. 19. $\delta^{13}C$ and $\delta^{18}O$ values of pure phases (KALC, DW, DOL, ANK, SID) and artificial mixtures (ME1, ME2, ME3) after 6, 24 and 48 hours of dissolution. ANK: ankerite, DOL: dolomite, DW: dawsonite, KALC: calcite, SID: siderite.

To test the method on real natural samples (RM6-9R and RM35-5R2), calcite "free" (the amount of calcite is trace or not detectable by XRD, Table 7) but dawsonite-bearing (16-8 m/m%, Table 7) samples were chosen. These samples also contain dolomite (7-8 m/m%, Table 7) and ankerite+siderite (21-27m/m%, Table 7). In these two natural samples dawsonite separation was possible. Therefore, it gives the opportunity to compare results of the bulk and the separates' isotopic composition. The isotopic results of the bulk rock samples are shown after 6-, 24- and 48-hours dissolution (Fig. 20). The isotopic composition of dawsonite separates represent the final data that the sequential method should give. The results show that after 24 hours reaction time, the isotopic composition of the bulk sample is different both in carbon and oxygen isotope values and does not represent the dawsonite's isotope data (Fig. 20). Thus, the other dissolving carbonates in the sample (dolomite, ankerite, siderite) influence and shift the isotopic composition/isotopic signature (Fig. 20).

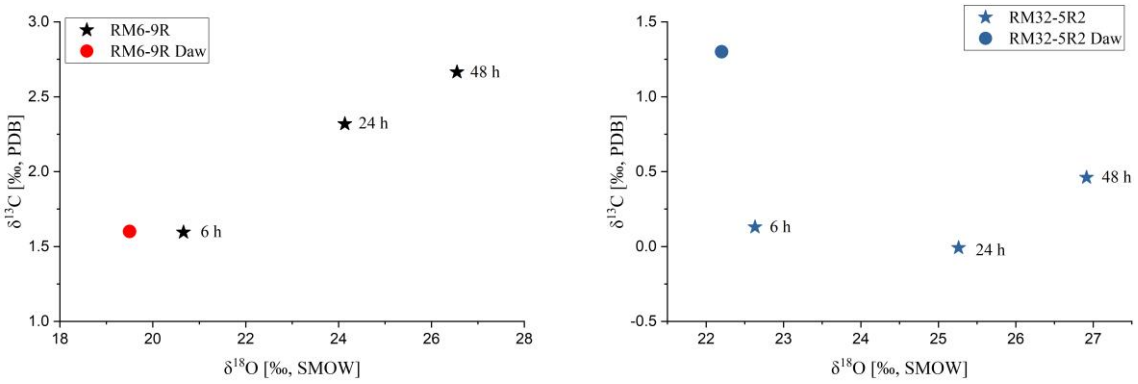

Fig. 20. $\delta^{13}C$ and $\delta^{18}O$ values of dawsonite separates (circle) and natural bulk samples (asterisk) after 6, 24 and 48 hour of dissolution. Natural samples are RM6-9R (left), RM32-5R2 (right). Daw: dawsonite.

It can be concluded that the widely used SEA methods are not suitable to obtain accurate isotopic composition for each carbonate phase, especially if the rock contains calcite, dawsonite ankerite, dolomite and siderite as well. Therefore, the separation of carbonate in the complex carbonate assemblage is not possible using this method. Although calcite could be eliminated from the samples with acetic acid (Pierre and Rouchy 1990, Swart and Melim, 2000) or ethylenediamine tetra acetic acid (EDTA, Glover, 1961; Humphrey, 1988), but it may partly dissolve dawsonite in the sample too. If a sample only contains calcite, dawsonite and dolomite: dawsonite can be separated by hand-picking (if it is possible), calcite can be eliminated with weak acid, which probably dissolve the rest of the dawsonite as well, and the isotopic composition of the remaining dolomite can be measured.

To get a representative result for each carbonate, mineral separates are recommended to use. Consequently, mineral separates were used in the rest of this study. It should be noted that the most commonly used density separation method, with bromoform+alcohol mixture, can shift the oxygen isotopic values of dawsonite. Freezing and melting of the rocks, instead of pulverizing (as in all the above cited studies), is an excellent tool to prepare it for the physical separation (dawsonite: hand-picking, siderite: magnetic separation) for isotope analyses.

7.2. Natural CO_2 occurrences

Based on the results of laboratory experiments, to avoid any questionable effect of the sequential dissolution of carbonates, separated minerals' isotope compositions were used to determine the origin of the parental fluid of the carbonate minerals and to shed light on the effect as well as the presence of CO_2 during their precipitation.

Mihályi-Répcelak and Ölbő fields

7.2.1. Crystallization and dissolution processes in the sandstone reservoir

Mineral compositions and textural relationship between mineral phases were studied to find traces of CO_2 flooding in the reservoir rock of Mihályi-Répcelak, by comparing with unaffected Ölbő sandstones. The samples from Ölbő are feldspathic litharenites, meanwhile the Mihályi-Répcelak sandstones are sublitharenites (Fig. 9). This indicates the difference in feldspar contents between the samples: plagioclase (albite) is 9-13 m/m% in the Ölbő samples, however, it is not detectable by XRD in the investigated sandstone reservoirs from Mihályi-Répcelak. K-feldspar is also more abundant (3-7 m/m%) in the Ölbő sandstones relative to the samples of Mihályi-Répcelak (1-3 m/m%) (Table 1 and 12). Kaolinite content is lower (1-4 m/m%) in the Ölbő samples compared to the Mihályi-Répcelak sandstone samples (3-12 m/m%). The amount of dolomite is similar, 6-15 m/m% and 6-11 m/m% in the Ölbő and Mihályi-Répcelak sandstones, respectively (Table 1 and 12). In case of calcite, Ölbő sandstones contain more calcite (3-19 m/m%) than the samples from Mihályi-Répcelak (<10 m/m%). The abundance of ankerite+siderite in the Ölbő sandstones (5-12 m/m%) is lower than the Mihályi-Répcelak samples (9-27 m/m%). Dawsonite [$NaAlCO_3(OH)_2$] content of the Mihályi-Répcelak sandstone samples is <16 m/m%, which is the indicator mineral of the large amount of CO_2 inflow in the reservoir (e.g., Worden, 2006). Dawsonite has not been found with XRD, ATR-FTIR and SEM methods in the Ölbő sandstone (and siltstone) samples which can mean that these rocks have not been flooded by large amount of CO_2 as in the Mihályi-Répcelak case.

Ankerite often occurs as a rim around dolomite grains, and it appears in two generations in both areas. Magnesium and iron (+manganese) content of carbonates shows a continuous transition between dolomite and ankerite in the Ölbő samples (Fig. 21, Table S4), differently from the Mihályi-Répcelak samples where ankerite were distinguished into two groups (Király, 2017) (Fig. 21). The outer rim (late generation) of ankerite is usually richer in iron than the inner rim (early generation) around the dolomite. However, the position of the Fe-rich and Fe-poor rims of ankerite may switch around the dolomite both in the Ölbő and Mihályi-Répcelak samples (Fig. 2A, 10B, and 21A).

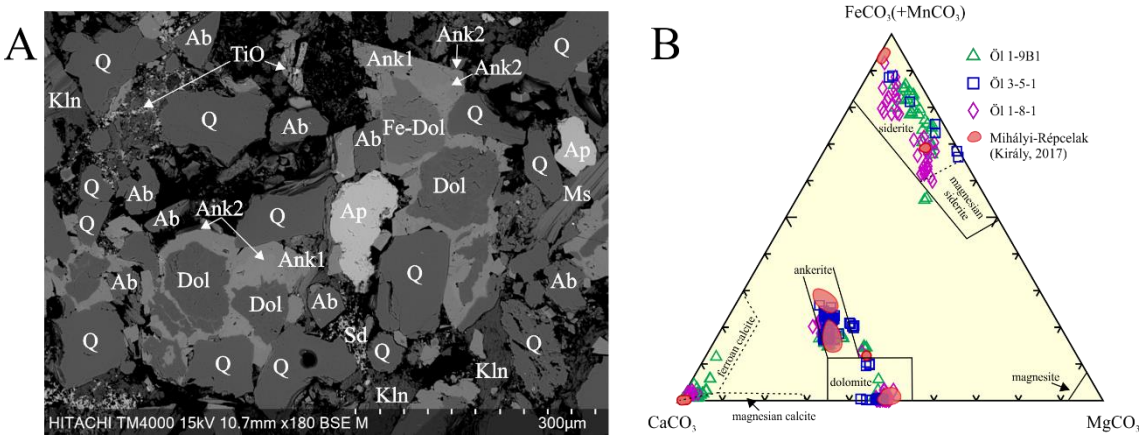

Fig. 21. BSE image of Öl 3-5-1 sample (A) and the chemical composition of carbonates (B; Chang et al., 1996; Karim et al., 2010). Dolomite, Fe-dolomite and two generations of ankerite are shown. Abbreviations: Ab: albite, Ank1: ankerite with low Fe + Mn content, Ank2: ankerite with high Fe + Mn content, Ap: apatite, Dol: dolomite, Fe-dol: Fe-dolomite, Kfs: K-feldspar, Kln: kaolinite, Ms: muscovite, Q: quartz, Sd: siderite

Siderite is present as a pore filling mineral in both areas, but in the Mihályi-Répcelak sandstone samples siderite grains can be mixed with dawsonite fibers. Siderite also shows zonation in the Ölbő sandstone, with varying Mg-Fe(+Mn) content (Fig. 10E).

Based on their textural and chemical characteristics (Table S4, Fig. 2 and 10), the carbonate minerals can be separated into three groups: 1) detrital, 2) early-diagenetic (formed during the sandstone diagenesis) and 3) late-diagenetic (formed during and after CO_2 flooding) (Cseresznyés et al., 2021). Dolomite most likely represents as a detrital carbonate phase that was originally deposited during sedimentation. Calcite remnants, low-Fe+Mn ankerites surrounding dolomite and most likely some of the siderites are considered to be early-diagenetic minerals in the Mihályi-Répcelak samples. Calcite, at least, is also partially detrital, whereas siderite is clearly replacing flake-like silicates, presumably biotite and clay minerals, providing the necessary Fe+Mn for siderite precipitation in the Mihályi-Répcelak area. The low-Fe+Mn ankerite could be the early cement phase in the studied sandstones, partially dissolving dolomite and probably calcite in the Mihályi-Répcelak area (Fig. 22A).

In Mihályi-Répcelak area dawsonite occurs in the pores as cement or replacing partially dissolved feldspars (K-feldspar, albite), representing a late diagenetic phase (Fig. 22B). This agrees with the literature on dawsonite formation induced by CO_2 flooding (e.g. De Silva et al., 2015; Worden, 2006). Other carbonates, i.e. the Fe+Mn-rich ankerite and siderite, occurring in the pores in textural equilibrium with the pore filling and cementing dawsonites, could have also formed in relation with the CO_2 flooding event (Fig. 22B). Studies proposed (e.g. De Silva et al., 2015; Forray et al. 2021; Worden, 2006)

that the source of Na^+, necessary for the crystallization of dawsonite, comes from the dissolving albite or porewater, whereas Al^{3+} may derive from the potential dissolution of aluminosilicates (feldspars and clay minerals). These ions become available in the porewater or in a thin fluid film around the grains (e.g. in a microenvironment, mineral replacement; Forray et al., 2021; Király et al., 2016a) when CO_2 floods the reservoir, dissolves in the porewater, which starts to dissolve the minerals in the sandstone. These effects are reflected in the Mihály-Répcelak sandstones, as their lower calcite contents may indicate dissolution by CO_2. Moreover, the higher abundance of ankerite+siderite associations in Mihályi-Répcelak also suggests that some part of ankerite+siderite could have precipitated after the CO_2 inflow. Király (2017) assumed that the second generation of ankerite precipitated after the CO_2 was introduced to the reservoir. The petrography of the Ölbő sandstone samples (Fig. 10A-B) can neither support nor disprove this assumption. The CO_2-flooding related dissolution process can also explain the considerable difference in feldspar content of sandstones in the two areas.

In contrast to Mihályi-Répcelak, kaolinite is present only in a single generation in the Ölbő sandstone samples. The absence of a second generation of kaolinite, which probably precipitated after the CO_2 flooding (Forray et al., 2021; Király, 2017), further supports the assumption that Ölbő sandstone was not flooded with CO_2, contrarily to those in Mihályi-Répcelak. Thus, it can be used as an initial (unchanged) sandstone for modelling geochemical interactions with CO_2.

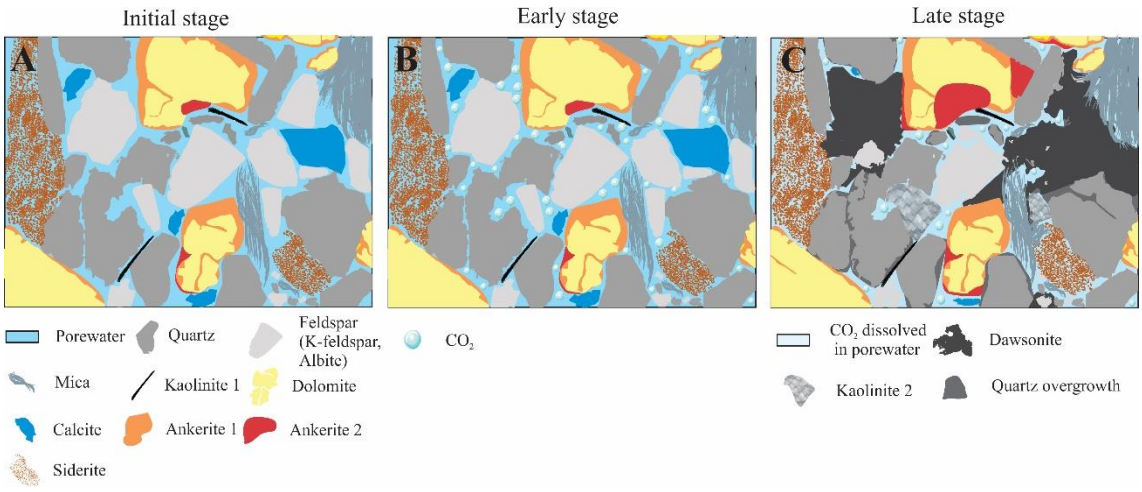

Fig. 22. Schematic figure of mineral changes in sandstone before the CO_2 inflow (A), during the CO_2 dissolution into the porewater (B) and after the CO_2 flooding (C).

7.2.2. The origin of carbonate forming CO_2

In order to constrain the source of the carbonate forming CO_2 and to identify which minerals could form during and/or after the CO_2 flooding, stable carbon and oxygen isotope compositions of the separated carbonates were determined. The measured isotopic compositions of the dawsonite and siderite were used in the carbonate-CO_2 fractionation equations of Bottinga (1968), Ohmoto & Rye (1979) for dawsonite and Golyshev et al. (1981) for siderite, to define the carbon isotope composition of CO_2 that was present during the formation of these carbonates (Eq. S1-S3 in Suppl.). Fractionation factors were calculated for temperatures of 70 °C and 98 °C, obtained from the geothermal gradient of the Pannonian Basin (40 °C/km; Dövényi et al. 1983; Lenkey et al. 2002), according to the current reservoir depths of 1375-1461 m (as a lower limit at 70 °C) and the assumed reservoir depths (~2100 m) maximum 98 °C before the inversion and tectonic uplift (Szamosfalvi, 2014), and an annual average surface temperature of 12 °C. These fractionation factors were used to calculate carbon isotope composition of CO_2 ($\delta^{13}C_{CO2}$) for the Mihályi field ($\delta^{13}C_{CO2}$: –4.5 ‰ and 2.0 ‰) and for the Répcelak field ($\delta^{13}C_{CO2}$: –4.8 ‰ and –2.2 ‰) which was present during dawsonite formation (Table 21) (Cseresznyés et al., 2021).

Table 21. Calculated $\delta^{13}C_{PDB}$ in CO_2 – dawsonite and CO_2 - siderite equilibrium at 70 and 98 °C. Calculations used carbonate-CO_2 fractionation equation (Bottinga, 1968; Golyshev et al., 1981; Ohmoto & Rye, 1979) see Eq. S1-S3 in Suppl.

Area	Sample name	Separated mineral	$\delta^{13}C_{CO2}$ [‰, PDB]		References
			T =70 °C	T =98 °C	
Mihályi	RM6-9R	dawsonite/1	-3.9	-2	Bottinga (1986)
			-4.5	-2.6	Ohmoto & Rye (1979)
	RM6-9R	dawsonite/2	-4	-2	Bottinga (1986)
			-4.5	-2.6	Ohmoto & Rye (1979)
	RM6-9R	siderite/1	-8.2	-6.1	Golyshev et al. (1981)
	RM6-9R	siderite/2	-8.4	-6.3	
	RM6-7R3	siderite	-6	-3.9	
	RM6-7R1	siderite	-6	-4	
Répcelak	RM32-5R2	dawsonite	-4.2	-2.2	Bottinga (1986)
			-4.8	-2.8	Ohmoto & Rye (1979)
	RM19-6R	siderite	-8.9	-6.8	Golyshev et al. (1981)
Ölbő	Öl 1-7	siderite	-8.5	-6.5	Golyshev et al. (1981)
	Öl 1-8-1	siderite	-9.2	-7.1	
	Öl 1-9B1	siderite	-9.5	-7.5	
	Öl 2-5	siderite	-10.2	-8.2	
	Öl 2-7A	siderite	-8.5	-6.5	
	Öl 3-5-1	siderite	-10.9	-8.8	
	Öl 6-4A	siderite	-8.8	-6.7	

The calculated $\delta^{13}C_{CO2}$ values in equilibrium with dawsonite (Fig. 23) overlap with those that are characteristics for mantle/magmatic derived carbon sources (–8 ‰ to –4 ‰; Ohmoto & Rye, 1979) and they agree well with the estimation of the European

subcontinental lithospheric mantle (SCLM, $\delta^{13}C$ = –3.9 ‰ - –2.1 ‰; Weinlich et al., 1999). Interestingly, the calculated $\delta^{13}C_{CO2}$ values also overlap with those ones measured in the current free CO_2 gas from the Mihályi-Répcelak field: –5.5 ‰ - –3.1 ‰ (Nádor, 2002) and –3.3 ‰ - –2.1 ‰ (Palcsu et al., 2014). Note that the reported isotopic composition of CO_2 may differ from the original source, because of the ongoing mineral forming reactions (isotopic fractionation) in the reservoir. It was assumed that the original volume of the CO_2 gas (which may not be limited to the reserve estimate of 25 Mt) is orders of magnitude higher than what can be consumed by mineral reactions (Gilfillan et al. 2009), leaving the overall isotopic composition of the gas intact. The assumed isotopic fractionation, caused by the potential CO_2 dissolution in the formation water, would cause only an insignificant fractionation compared to the degree of overlap observed here (Gilfillan et al. 2009). The isotope values of dawsonite suggest magmatic origin for the majority of the CO_2 from which the dawsonite crystallized (Fig. 23) (Cseresznyés et al., 2021).

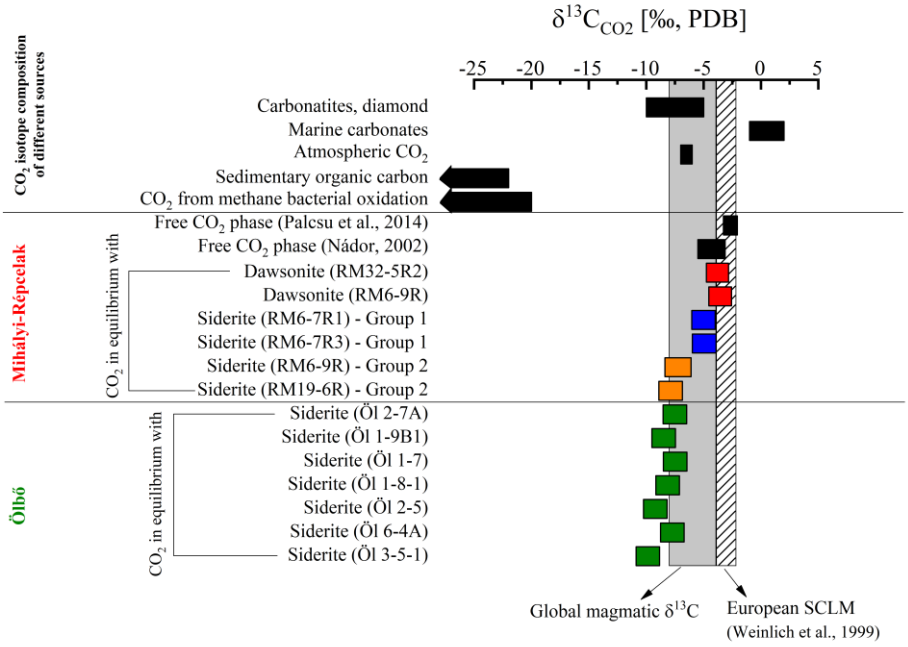

Fig. 23. Calculated $\delta^{13}C_{CO2}$ in equilibrium with separated dawsonite and siderite along with carbon isotope ranges of free CO_2 fluid from Mihályi-Répcelak, compared to that of a selection of carbonate reservoirs worldwide. Calculated $\delta^{13}C_{CO2}$ in equilibrium with siderite is presented from both Ölbő and Mihályi-Répcelak field.

In contrast, the calculated $\delta^{13}C_{CO2}$ values in equilibrium with siderite and ultimately the source of the CO_2 from which siderite precipitated is not obvious. Based on the measured carbon isotope composition of siderite from Mihályi-Répcelak, two

groups can be distinguished: Group-1 (heavy): from +4.2 ‰ to +4.3 ‰ and Group-2 (light): from +1.3 ‰ to +2.1 ‰ (Table 13) (Cseresznyés et al., 2021). In the Group-1 samples, the calculated $\delta^{13}C_{CO2}$ values in equilibrium with siderite (–6.0 ‰ - –3.9 ‰; Table 21) fall closer to the calculated values from dawsonites and to the European SCLM (Fig. 23). This means that, at least part of the siderite may also have precipitated as an effect of CO_2 flooding in Mihályi-Répcelak. The inter-mixed petrographic feature of dawsonite and siderite in these sandstones (Fig. 2D) might support this scenario. However, in case of Group-2, the calculated $\delta^{13}C_{CO2}$ values (–8.4 ‰ - –6.1 ‰; Table 21) are significantly lighter than those calculated from dawsonites and lighter than what is observed in the free CO_2 gas (Fig. 23). Interestingly, the calculated $\delta^{13}C_{CO2}$ values (–10.9 ‰ - –6.5 ‰; Table 21) of siderite from Ölbő overlap with these siderites in Group-2.

These findings can indicate two scenarios: 1) the CO_2 present during the precipitation of Group-2 siderites did not have a different origin, but went through some degree of fractionation by dissolution into water, relative to its isotopic composition when Group-1 was formed (along with dawsonite). This could imply that Group-2 siderites have a different age than Group-1. Although dating siderite is beyond the scope of this work, this may be a reasonable explanation considering the variety of its fabric features (Fig. 2 and 10); 2) the CO_2 present during the precipitation of Group-2 siderites has a different origin. This is difficult to envisage in light of the consistency of the dawsonite data, along with the conclusions on a single CO_2 source in the Mihályi-Répcelak field (Palcsu et al., 2014, Vető et al. 2014) and considering the overlapping data with siderite from Ölbő area. However, since not all the siderite shows close textural relationship to dawsonite, at least some part of the siderite could have formed before CO_2 flooding, likely representing an early diagenetic mineral (Cseresznyés et al., 2021). The presence of siderite and the calculated data of siderite from the unflooded Ölbő sandstones also support this scenario. These observations reinforce that stable carbon isotopes provide an excellent tool to distinguish diagenetic carbonates from CO_2 flooding-related mineral precipitations and/or the timing of formation.

7.2.3. Origin of the porewater

Theoretically dawsonite provides an exceptional opportunity to determine the origin of porewater during CO_2 flooding as, besides oxygen, it contains hydrogen within its structural OH^-, of which isotopic composition must be strongly related to the fluid from which it was formed (Cseresznyés et al., 2021). However, it has not yet been exploited as all studies to date focused only on carbon and oxygen isotope analyses (Baker et al., 1995; Comerio et al., 2014; Ferrini et al., 2003; Gao et al., 2009; Golab et al., 2006; Li and Li, 2017; Liu et al., 2011; Ming et al., 2017; Uysal et al., 2011; Zhao et al., 2018; Zhou et al., 2014). As the hydrogen isotope fractionation factor is not known for the dawsonite-water system, a fractionation factor of another OH-bearing mineral needs to be utilized. Based on experiments (Chesworth, 1971) and natural samples (e.g. Goldbery and Loughnan, 1977), the polymorph of $Al(OH)_3$ (gibbsite, bayerite, nordstrandite; Chesworth, 1971) or boehmite [AlO(OH)] can form in a geological reservoir similar to the one presented in this study, which grants further investigation into these candidates. It has been found that at T<51 °C gibbsite incorporates the lighter hydrogen isotope during its formation (Chen et al., 1988; Vitali et al., 2001). Since the OH^- in the dawsonite is also connected to Al octahedrons (Łodziana et al., 2011) therefore the H isotopic fractionation in the gibbsite – H_2O system can be similar to dawsonite – H_2O systems (Cseresznyés et al., 2021). Therefore, the hydrogen isotope composition of porewater in equilibrium with dawsonite was calculated using the gibbsite-H_2O fractionation equation (<150 °C; Méheut et al., 2010; Eq. S4 in Suppl.) (Table 22).

Table 22. Estimated δD values of porewater from the dawsonite-bearing sandstone samples calculated with gibbsite-H_2O fractionation factor.

Area	Sample	δD_{H2O} [‰, SMOW]		References
		T=70 °C	T=98 °C	
Mihályi	RM6-9R	-103	-86	Méheut et al. (2010)
	RM6-7R3	-89	-72	
	RM6-7R2	-88	-71	
	RM6-7R1	-90	-73	
Répcelak	RM32-5R2	-86	-69	
	RM19-6R	-91	-74	

The measured δD values of dawsonite from Mihályi-Répcelak field, scatter around –60 ± 2 ‰, except in the RM6-9R sample, which is characterized by value of –74 ‰ (Table 14). The calculated δD_{H2O} values are between –86 ‰ and –91 ‰ at 70 °C and –69 ‰ - – 74 ‰ at 98 °C for the RM6-7R1, RM6-7R2, RM6-7R3, RM32-5R2, RM19-6R, and for RM6-9R are –103 ‰ at 70 °C and –86 ‰ at 98 °C (Table 22). To determine the oxygen isotope composition of porewater in equilibrium with dawsonite, the calcite-

water fractionation factor was used (O'Neil et al., 1969; Eq. S5) at temperatures of 70 °C and 98 °C. The calculated $\delta^{18}O_{H2O}$ values for RM6-9R ranges from –1.4 ‰ to +2.1 ‰, whereas the calculated $\delta^{18}O_{H2O}$ values in dawsonite from the RM32-5R2 range between +1.3 ‰ and +4.7 ‰ (Table 23).

Table 23. Calculated oxygen isotope composition of porewater ($\delta^{18}O_{H2O}$) in equilibrium with dawsonite at two different temperatures in the Mihályi-Répcelak field. Calculation used calcite-water fractionation equation (O'Neil et al., 1969) see Eq. S5 in Supplementary.

Area	Sample	Separated mineral	$\delta^{18}O_{H2O}$ [‰, SMOW]	
			T =70 °C	T =98 °C
Mihályi	RM6-9R	dawsonite/1	-1.4	2.1
	RM6-9R	dawsonite/2	-1.4	2
Répcelak	RM32-5R2	dawsonite	1.3	4.7

The calculated δD_{H2O} and $\delta^{18}O_{H2O}$ values in equilibrium with RM6-9R and RM32-5R2, and available groundwater data (Bükfürdő; Nádor, 2002) are presented in the δD-$\delta^{18}O$ diagram (Fig. 24). The calculated isotope values are plotting on the right side of the Global Meteoric Water Line (GMWL; Craig, 1961). Assuming that the original fluid has a meteoric origin (falls on the GMWL) the observed systematics (i.e. enrichment in ^{18}O) can be caused by interaction with country rock with an elevated oxygen isotope composition. Generally, the carbonate, metamorphic and magmatic rocks are characterized by $\delta^{18}O$ values above 2 ‰ (Clark and Fritz, 1997), thus this shift in the data relative to GMWL indicates enhanced modification of the isotopic ratios of the porewater due to (CO_2-)water-rock interactions (Clark and Fritz, 1997).

As the data plot close to the global magmatic field, some contribution from a magmatic source (Taylor, 1974) can be envisioned as well. This possibility can especially be realistic because it was found that the majority of the CO_2 that triggered the dawsonite formation, also has a magmatic origin (Cseresznyés et al., 2021). However, the contribution of the magma-originated water is likely subordinate compared to the groundwater circulating in the basin (Tóth et al., 2016).

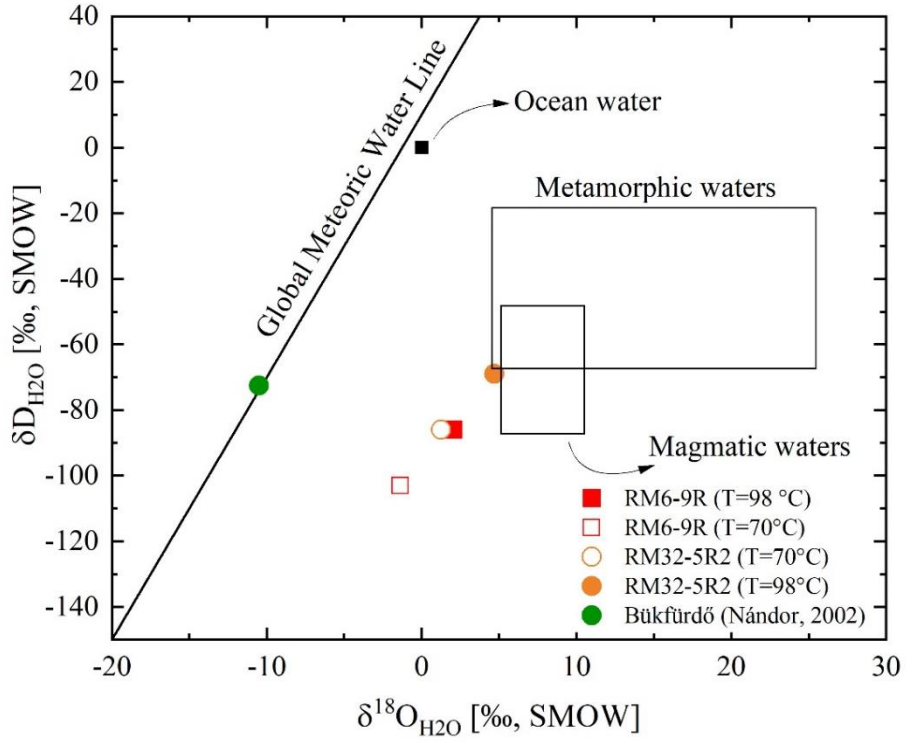

Fig. 24. Estimated porewater δD and $\delta^{18}O$ values in equilibrium with dawsonite (RM6-9R: red square; RM32-5R2: orange square). Groundwater data from the vicinity (i.e., Bükfürdő; green circle) of the studied location and ranges of major water types is shown as well. Magmatic and metamorphic values are from Taylor (1974). Modified after Brownlow (1996), Rice (1993), Sheppard (1986).

7.2.4. Geochemical modelling – simulation of the sandstone-water-CO_2 system

To simulate the interactions in the rock-water-CO_2 system of the sandstone reservoirs, the petrographic observations of Ölbő and Mihályi-Répcelak sandstone samples were utilized. (in section 7.2.1). The aim of the modeling was to understand and predict the geochemical reactions, which take place on the timescale of decades, after CO_2 is injected into a sandstone reservoir. To simulate this complex system, thermodynamic-batch model type is the first step to check which reactions are realistic and which should be ignored. The thermodynamic-batch models shown similar changes in the porewater, mineral dissolution and precipitation as kinetic models, therefore only kinetic model results are described in detail. Important to note, that in the kinetic-batch models, dissolved CO_2 was injected into the system just once.

For the sensitivity analysis of water, three different water types were utilized. The initial ion concentration was different in ion-free water, NaCl and $NaHCO_3$ type waters (Table 10). Most of the ions show similar trend in the 200 years following the CO_2 injection. Small differences can be recognizable in Na^+ (Na) and Ca^{2+} (Ca) content in the

first few seconds of the simulation (Fig. 25). The Fe^{2+} (Fe) content also shows small increase in the first half year in the $NaHCO_3$ type water but unfortunately, this simulation was blocked after the first half year.

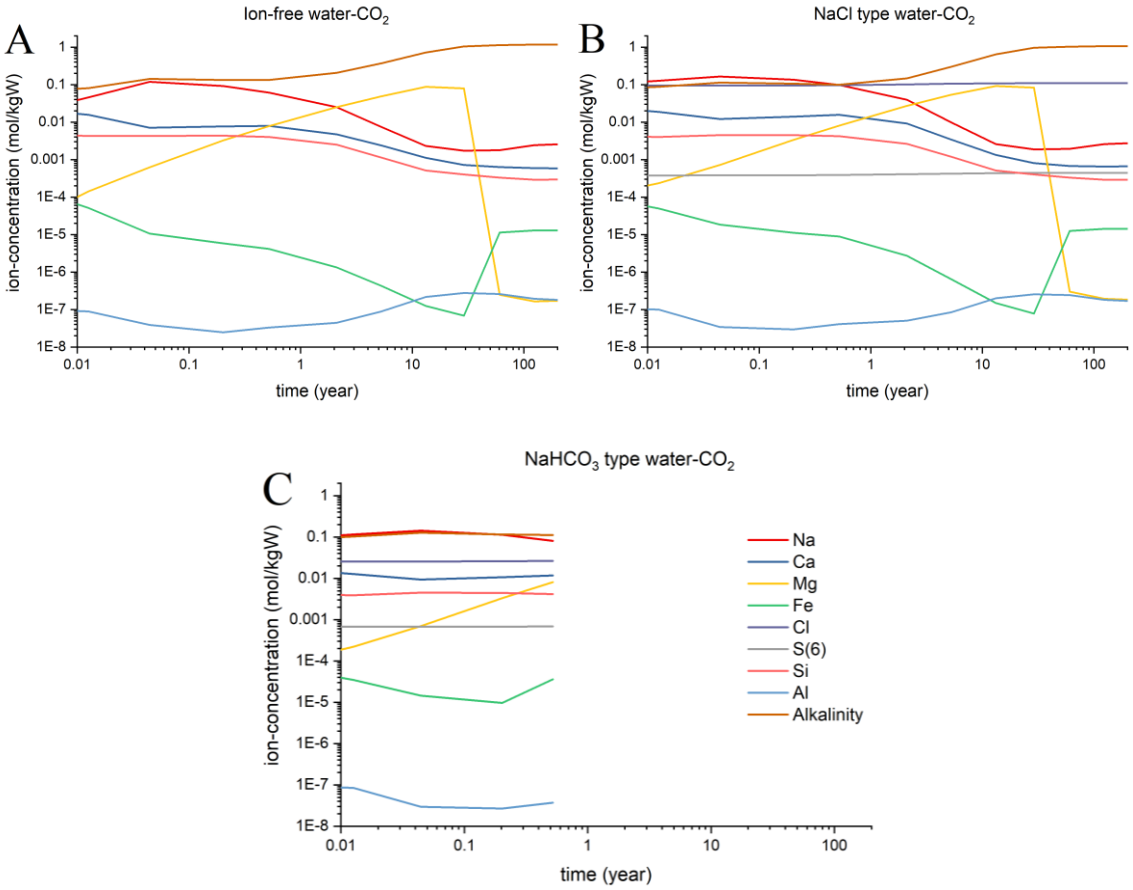

Fig. 25. Kinetic-batch model shows the changes in the ion concentration (mol/kgW) on log scale over 200 years in the ion-free water-CO_2 (A), NaCl type water-CO_2 (B) and the $NaHCO_3$ type water-CO_2 (C) systems.

The effect of water chemistry on the mineral dissolution and precipitation processes during the simulation are shown in Fig. 26. The models (irrespective of different initial water compositions) mainly show similar results. Dawsonite, kaolinite, ankerite and quartz are precipitated meanwhile albite, calcite, illite, and siderite are dissolved (Fig. 26). Due to the different order of magnitude, quartz was excluded from the figure for better visualization. Significant differences in the model results were not observed therefore, ion-free water was used in the rest of the models.

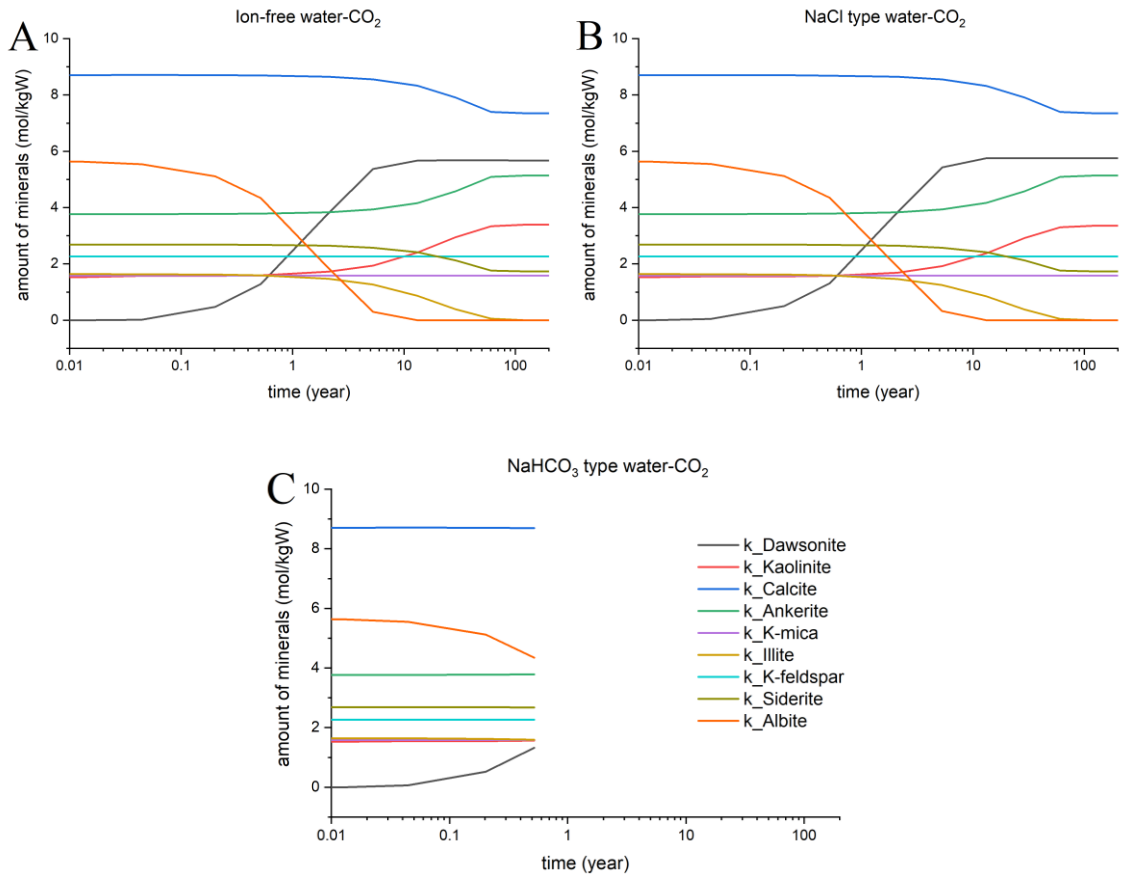

Fig. 26. Kinetic-batch models show the rate of mineral dissolution/precipitation (mol/kgW) on log scale over 200 years in the ion-free water-CO_2 (A), NaCl type water-CO_2 (B) and the $NaHCO_3$ type water-CO_2 (C) system. Quartz was excluded from the figure for better visualization.

Focusing on the changes in mineral abundances in the kinetic-batch models, the amount of albite is decreasing after the CO_2 injection, and dawsonite precipitates parallel to albite dissolution (Fig. 27A-D). The amount of calcite and illite is also decreasing, meanwhile ankerite and kaolinite precipitate. The model also indicates quartz precipitation (Fig. 27B, D). Considering the time scale, the majority of the reactions take place in the first 30 years (Fig. 27A-D) and reach equilibrium state around 125 years (Fig. 27B). Based on the model the first twelve year period is the most intensive, where most of the mineral dissolution and precipitation reactions take place (Fig. 27C-D).

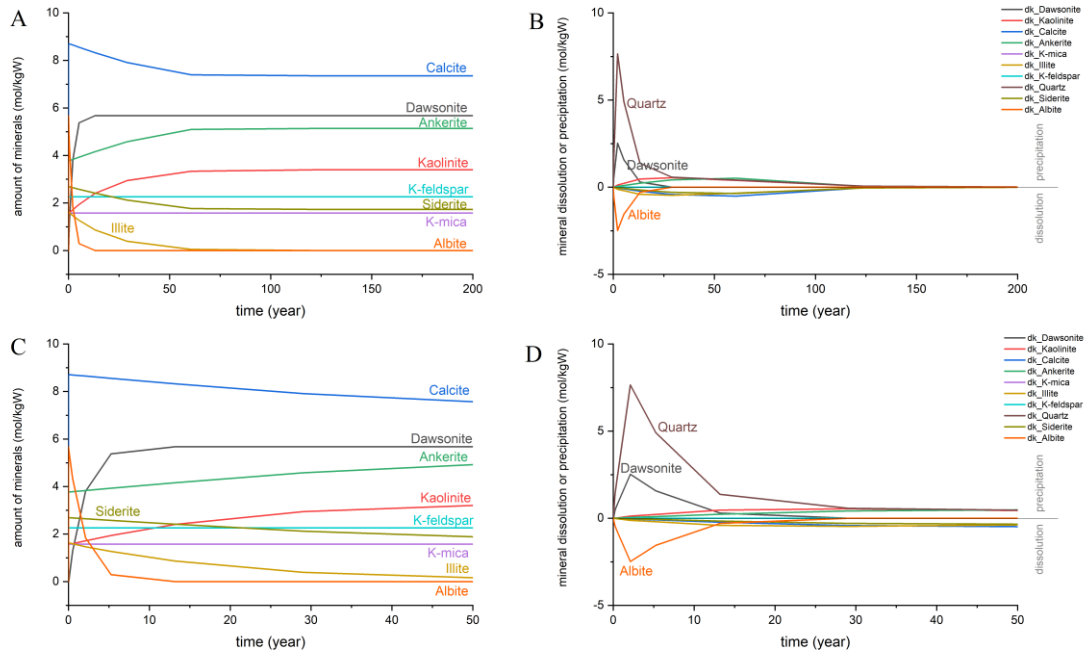

Fig. 27. Kinetic-batch model results for 200 years (A, B) at fixed temperature (70 °C) and pressure (190 bar). Amount of minerals (left) and the rate of mineral dissolution/precipitation (right) in mol/kgW unit are shown. C and D figures show the first 50 years. Quartz was excluded from the A and C figures for better visualization.

The sensitivity analysis of temperature and pressure were run on three different scenarios: 1) fixed pressure (190 bar) and the temperature changing between 70 °C and 100 °C, 2) fixed temperature (90 °C) and the pressure changing from 140 to 215 bar. The third scenario considers the parallel change of the temperature and pressure based on exact depths (1400-2150 m). These models (Fig. 28) are focusing on the first twelve years based on the results of the previous model (Fig. 27). These models show similar mineral reactions, and mineral abundance changes, however, the propagation of the reaction front is changing during the three scenarios (Fig. 28A-C). When the temperature increases but the pressure is stable (Fig. 28A), the rate of mineral dissolution and precipitation is higher. The albite-dawsonite pair marks the reaction front very well and can be followed easily. However, in the scenario where pressure increases, and the temperature is stable (Fig. 28B), the albite-dawsonite pair show the same at the 140 bar and at 215 bar. These models do not show recognizable differences in the reaction rate (Fig. 28B). The third scenario (Fig. 28C) shows well the significance of temperature for the mineral dissolution/precipitation rate. The increasing temperature accelerates the rate of the mineral reactions, meanwhile increasing pressure has no significant effect on the dissolution/precipitation rates of the minerals. The model results agree with the observations of Sendula (2015), who carried out kinetic-batch modelling on sandstone

samples of the Szolnok Formation, from Zagyvarékas (Great Hungarian Plain, Hungary) for 800,000 years.

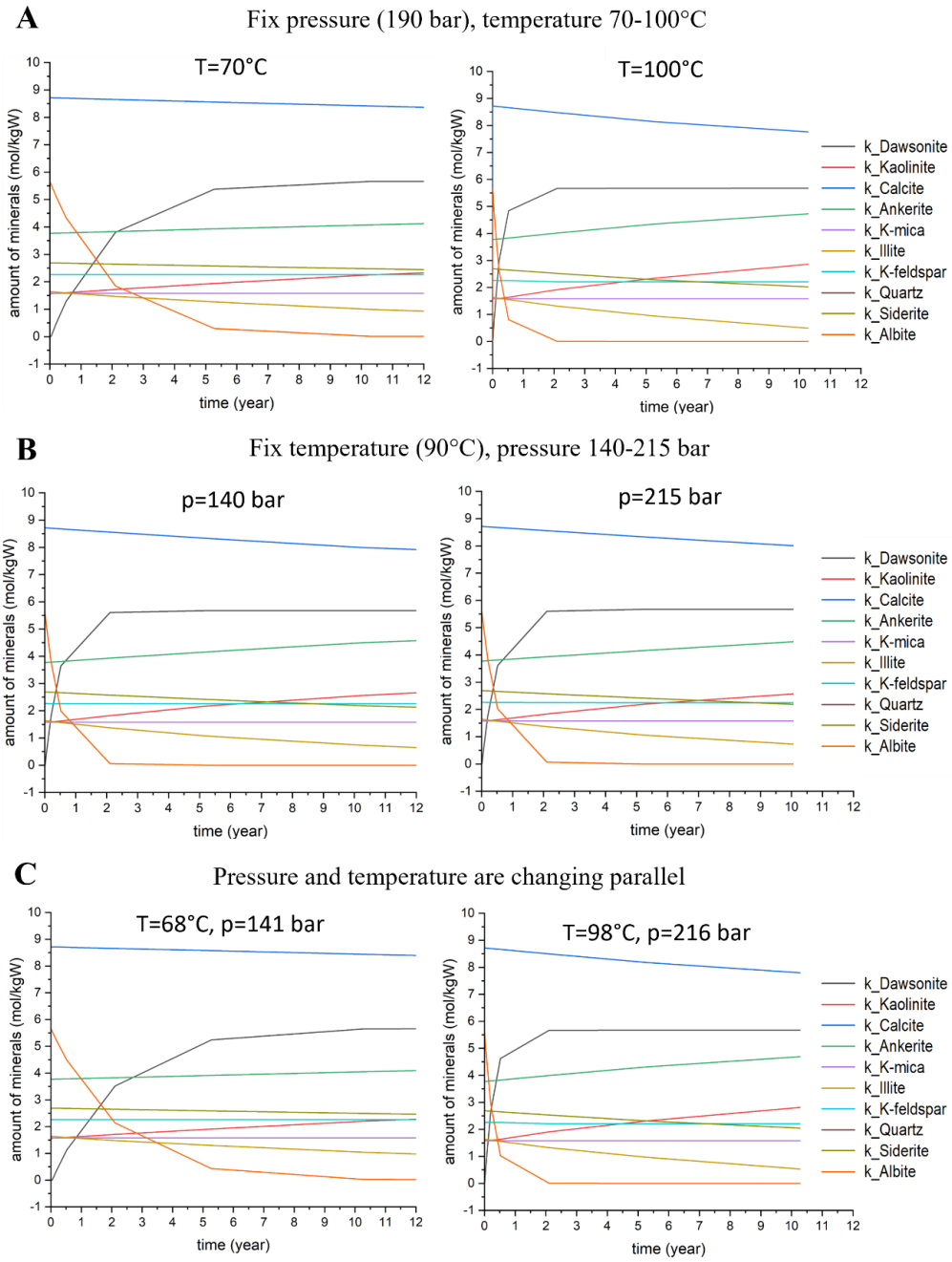

Fig. 28. Sensitivity analysis of temperature and pressure in kinetic-batch models. Amount of minerals is shown in mol/kgW unit. A: fix pressure (190 bar), changing temperature (70-100 °C), B: fix temperature (70 °C), varying pressure (140-215 bar), C: changing pressure (141-216 bar) and temperature (68-98 °C) parallel. Quartz was excluded from the figure for better visualization.

One kinetic-reactive transport model was run based on the results of the above presented kinetic-batch models. The temperature was set to 78 °C, the pressure was 166 bar. The model was run for 54 years and over 300 m distance. The main difference

compared to the previous models is that the reactive transport model considers fluid flow in time through the rock, refreshing the solution, therefore the porewater can dissolve CO_2 repeatedly, and affects the rock body on a large distance. The CO_2-rich solution is flowing from the left to the right on the plots, therefore the reaction front can be followed (Fig. 29A-C). The pH decreases from 10 to 4 immediately after CO_2 floods the reservoir and dissolves in the porewater (Fig. 29A). The CO_3^{2-} (C) and HCO_3^- (Alkalinity) contents of the solution are increasing from the first step (Fig. 29A). SiO_2 (Si) starts to decrease, but it is quasi stagnant during the simulation (Fig. 29A-C). Cl^- and SO_4^{2-} are constantly zero during the simulation. Na^+ in the solution is increasing in the first seconds, then continuously decreasing (Fig. 29A-C). The Al^{3+} content is moving together with the Na^+ (Fig. 29A-C), because of the coupled albite dissolution and dawsonite precipitation (Fig. 29A-C). In the middle of the simulation, pH starts to increase up to 6 (Fig. 29B), due to the buffering effect of the dissolving carbonates (calcite and siderite). HCO_3^- is decreasing slowly with time (Fig. 29B-C). The Ca^{2+} and Fe^{2+} content is increasing, meanwhile Mg^{2+} is decreasing parallelly (Fig. 29B-C). By the end of the simulation pH is around 6 (Fig. 29C) and CO_3^{2-} reaches a plateau. Kaolinite, ankerite and quartz precipitations (quartz is out of the figure scale) are observed as well. Calcite, siderite, illite and K-feldspar are dissolving during the simulation (Fig. 29A-C).

In summary, the model results support most of the petrographic observation that lower amount of albite in the Mihályi-Répcelak (CO_2-flooded) sandstone samples indicates its dissolution, which drives dawsonite precipitation. Low amount of kaolinite can also precipitate after albite dissolution. According to the kinetic-batch models, the majority of these reactions takes place in the first 30 years after CO_2 injection. However, in this model CO_2 was injected only once into the reservoir (in the beginning) and it does not take fluid flow into consideration (closed system). On the other hand, the reactive transport model considers the continuous flow of CO_2-saturated water through the rock and indicates that the reactions getting slower after 54 years in the first 200 m of the rock body. The Ölbő and Mihályi-Répcelak areas, as natural laboratories, provided the opportunity to validate these geochemical models both before interaction with CO_2 (Ölbő samples) and after millions of years being in contact with CO_2 (Mihályi-Répcelak samples).

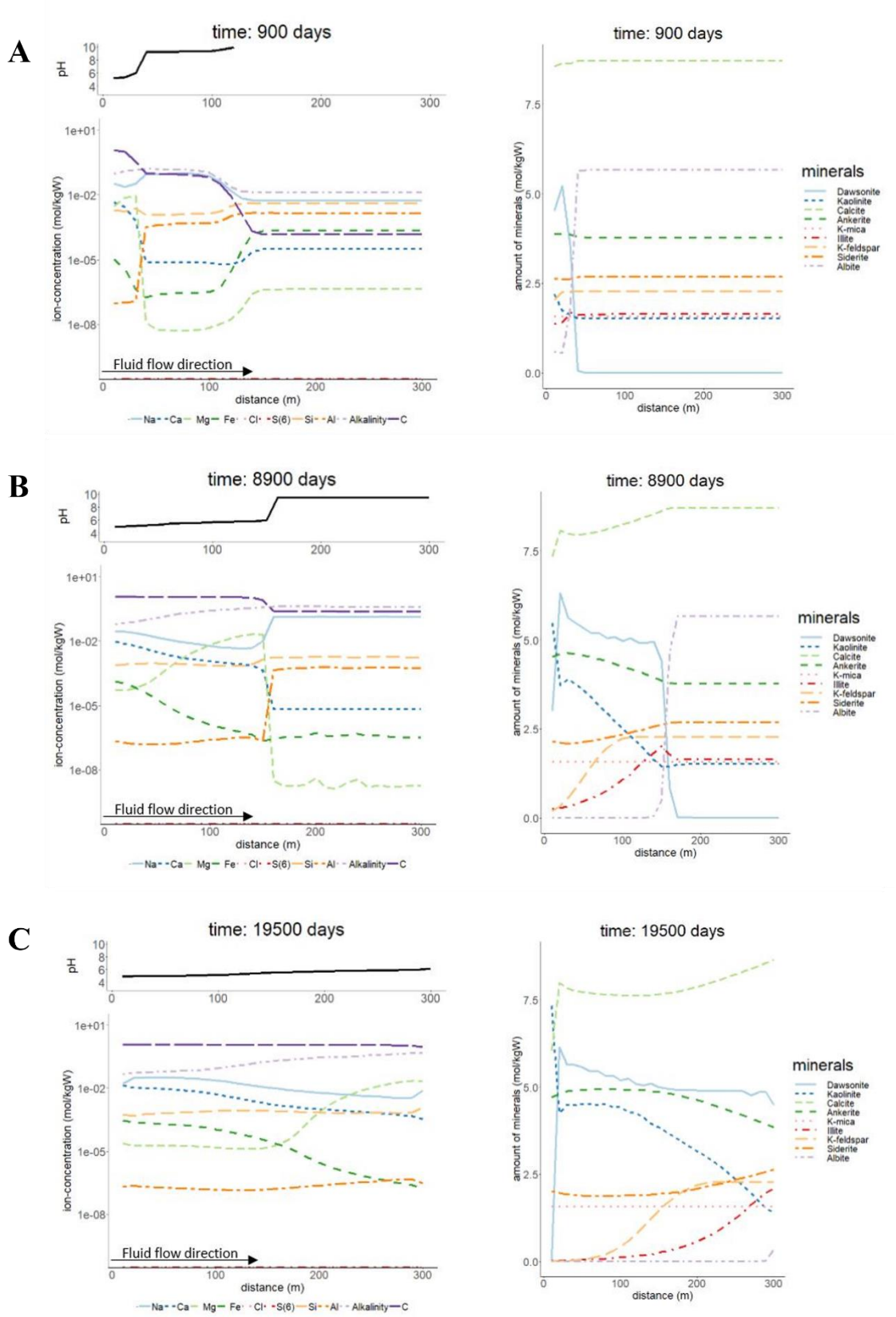

Fig. 29. Kinetic-reactive transport model in three states of the simulation. Result of the pH (top left), ion concentration in mol/kgW unit (bottom left) and the amount of minerals in mol/kgW unit (right). A: beginning of the simulation, B: middle part of the simulation, C: end of the simulation.

Covasna

Dawsonite surface occurrence can be found along the bank of the creek and mineral spring waters, which come to the surface in the Hankó Valley in Covasna, therefore it is necessary first to discuss both the chemical and isotopic composition of the studied waters.

7.2.5. Hydrogeochemical facies of waters

To constrain the hydrogeochemical facies of the creek and the spring waters, Piper plots (Piper, 1944) were utilized. The spring water shows Na^+ dominance with elevated concentrations of Cl^- and HCO_3^-, therefore, its hydrogeochemical facies is sodium bicarbonate type (Fig. 30). Although the creek water can be also regarded as sodium bicarbonate type based on the major ion content, it plots into the mixed type of water zone (Fig. 30). Previously published well water data from Covasna by Georgescu (1976; Table S5) plots in the same zone, however, two data also fall in the sodium bicarbonate field, close to the spring water data of this study, and one water in the magnesium bicarbonate zone (Fig. 30). The hydrogeochemical facies of well water data published by Vaselli et al. (2002) from Covasna is also sodium bicarbonate and plot close to the Covasna spring water data from this study (Fig. 30). It can be concluded that our data and all published spring and well water data from Covasna are in the sodium bicarbonate or fall in the mixed type of water zones.

The Na^+ and HCO_3^- rich waters from Covasna have 54.1-183.3 mg/L Ca^{2+} content (Table 18 and S5). Among the trace elements, aluminium has a relatively high concentration in the creek water (29.9 µg/L) and is also present in the spring water (2 µg/L) (Table 18). The creek and the spring water chemical compositions indicate that chemical constituents needed to precipitate dawsonite (and/or alumohydrocalcite) are present in considerable concentrations in these waters. These observations imply that the studied waters could be the source of dawsonite and alumohydrocalcite formation in the Hankó Valley.

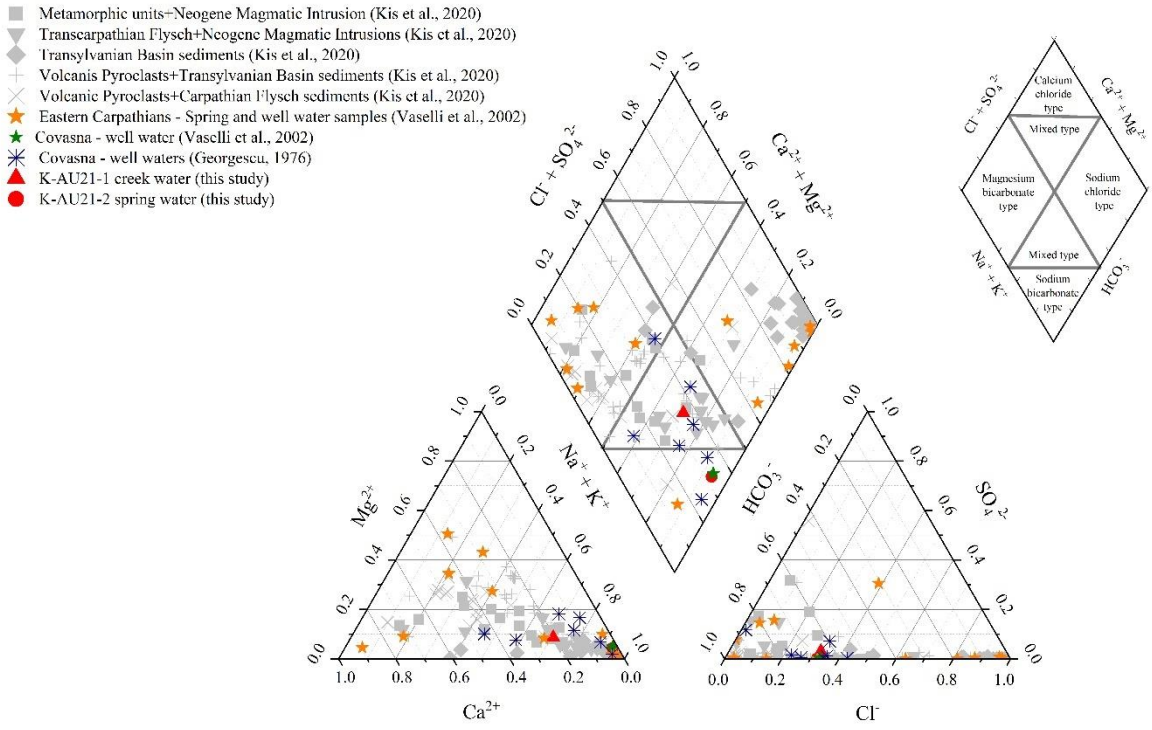

Fig. 30. Piper diagram of creek (red closed triangle) and spring (red closed circle) waters from Covasna in comparison with the CO_2-rich waters from the Eastern Carpathians (Georgescu, 1976; Kis et al., 2020; Vaselli et al., 2002).

7.2.6. Isotopic signature of waters

The hydrogen and oxygen isotope compositions of the collected creek water plot close to the Global Meteoric Water Line (GMWL; Craig, 1961) and the Local Meteoric Water Line (LMWL, Fig. 31; Ionete et al., 2015). The LMWL was defined based on the isotope data from Bodoc spring that is located 30 km away from the present study area. In addition, the studied creek water data fit very well with spring water samples from the Ciuc Basin (Fórizs et al., 2011) and the majority of the spring and well water data from the Eastern Carpathians (Kis et al., 2020) (Fig. 31).

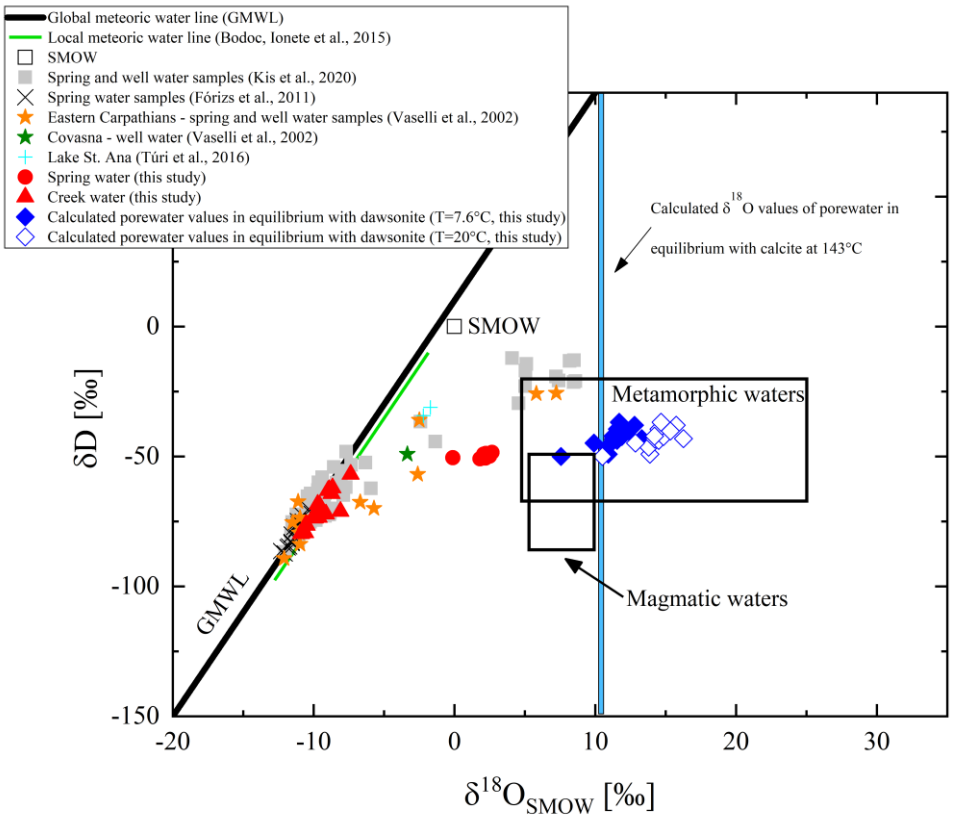

Fig. 31. δD and $\delta^{18}O_{SMOW}$ diagram showing isotopic values of collected creek (red closed triangle), spring water samples (red closed circle) and the calculated porewater (for 7.6 and 20 °C) in equilibrium with dawsonite (blue closed and open diamond, respectively). Spring and well water samples in Eastern Carpathians (Fórizs et al., 2011; Kis et al., 2020; Túri et al., 2016; Vaselli et al., 2002) and Covasna (Vaselli et al., 2002) are shown for comparison. Global Meteoric Water Line (GMWL; Craig, 1961), Local Meteoric Water Line of Bodoc (LMWL; Ionete et al., 2015) and SMOW (Colpen, 1996) are also shown. Magmatic and metamorphic values are after Taylor, (1974). Modified after Brownlow, (1996); Rice, (1993); Sheppard, (1986).

In contrast, the spring water isotopic composition (red circles, δD: –50.9 ‰ to –48.4 ‰, $\delta^{18}O_{SMOW}$: –0.1 ‰ to +2.5 ‰) plots on the right side of the GMWL and the LMWL (Fig. 31) showing more (rather) positive $\delta^{18}O$ values (–0.1 ‰ - +2.7 ‰). Their δD values (–50.9 ‰ - –48.4‰) nevertheless are within the range of water samples falling on the GMWL. Beside this spring water, there is data from other springs and wells from Covasna and Eastern Carpathians, which plot on the right side of the GMWL (Kis et al., 2020; Vaselli et al., 2002). Some of these waters show even higher positive hydrogen values than those with pure meteoric origin (Fig. 31, Kis et al., 2020; Vaselli et al., 2002). These waters are characterized by high salinity (i.e. saline waters). Their origin and isotopic signature are explained by complex geochemical process like halite dissolution

or interaction with clay minerals present in the underlying rock formations (Kis el al., 2020; Vaselli et al., 2002).

Although the spring water present in this study shows similar oxygen isotope shift to the above mentioned waters' data but their salinity is significantly lower than those studied by Kis et al. (2020). Therefore, its origin is likely different. Various phenomena can affect and modify the isotopic composition of waters, e.g., mixing, mineral dissolution/precipitation, evaporation, water-rock interaction (Clark and Fritz, 1997; Hoefs, 2009; Kis et al., 2020; Sharp, 2017). Chemical/isotopic exchange between basinal brines and host rocks is one of the typical reasons which modifies the oxygen isotope composition (Sharp, 2017). Sedimentary rocks have typically heavy $\delta^{18}O_{SMOW}$ values (+20 - +30 ‰, especially for carbonates), therefore water $\delta^{18}O_{SMOW}$ may increase during the rock-water interactions (Hoefs, 2009; Sharp, 2017). Oxygen isotope exchange between CO_2 and H_2O in aqueous environment can also cause enrichment only in $\delta^{18}O_{SMOW}$ values (Johnson and Mayer, 2011).

To reveal the origin of waters, use of the δD-Cl^- and $\delta^{18}O_{SMOW}$-Cl^- values were plotted in Fig. 32. The Cl^- concentration of the studied creek water (Cl^-: 247 mg/L) falls in the field occupied by most of the water samples (Cl^-: 2 - 200,168 mg/L) from the Eastern Carpathians (Fig. 32). The oxygen and hydrogen isotope compositions in the creek water of Hankó Valley show slightly more positive values ($\delta^{18}O_{SMOW}$: –7.7 ‰, δD: –60 ‰) than the majority of the water samples ($\delta^{18}O_{SMOW}$: –12 ‰ to –8 ‰, δD: –86 ‰ to –67 ‰) (Fig. 32). The studied spring water data show heavier oxygen isotope composition ($\delta^{18}O_{SMOW}$: +2.2 ‰, Cl^-: 2370 mg/L) than most of the water samples generally, and the theoretical sea water (i.e. $\delta^{18}O_{SMOW} = 0$ ‰), similar to saline/extremely saline waters ($\delta^{18}O_{SMOW}$: +4.1 ‰ to +8.6 ‰, Cl^-: 5697 mg/L to 197,686 mg/L) studied by Kis et al. (2020) and Vaselli et al. (2002). However, the studied spring water's hydrogen isotope composition (–48.8 ‰) shows significantly lighter hydrogen isotope value than the SMOW and the saline waters/extremely saline waters (–25.6 ‰ to –12.2 ‰) (Kis et al., 2020; Vaselli et al., 2002). Vaselli et al. (2002) noticed that saline waters discharge is mainly located around the eastern part of the Transylvanian Basin (Corund Nord), also along the main thrust belt area (Slanic, Targu Ocna, Covasna), as well as in the foredeep area (Piriul Sarat; Berca). These extremely saline waters (Corund Nord – Harghita Mts., Berca - Vrancea) which are much more saline (Cl^-: 33,600 mg/L and 100,625 mg/L) than the SMOW on the $\delta^{18}O_{SMOW}$-Cl^- diagram, can be related to the evaporites that precipitated during the Messinian salinity crisis (Vaselli et al.,2002). This

could cause heavier oxygen isotope composition in the above mentioned extremely saline waters. However, Kis et al. (2020) argues that the direct dissolution of the halite-domes cannot cause such isotopic shift also in δD values in case of their saline samples. Kis et al. (2020) assumed interaction with clay minerals in case of their highly saline water samples, which can change the chemical composition (e.g. increase Ca^{2+} and the salinity) of brines and cause enrichment in the heavy isotopes, since dehydration of clay minerals during compaction could increase the stable hydrogen and oxygen isotope values (Boschetti et al., 2016; Kharaka and Hanor, 2013; Kis et al., 2020; Zuber and Chowaniec, 2009).

In case of Covasna, the halite dissolution, and a relation to the Messinian salinity crisis is not plausible. However, the filtration of clay minerals can be a possible interaction in the area, which could have enriched the Ca^{2+} and the trace element content like Al^{3+} in the waters. The studied spring water (which is CO_2-rich) also has a potential to interact with the country rocks, causing the enrichment in calcium and trace elements. It can cause also shift in the oxygen isotope ratio. In addition, the oxygen isotope composition of the studied spring water can also be shifted as a result of exchange with high concentration of CO_2 dissolved in the water.

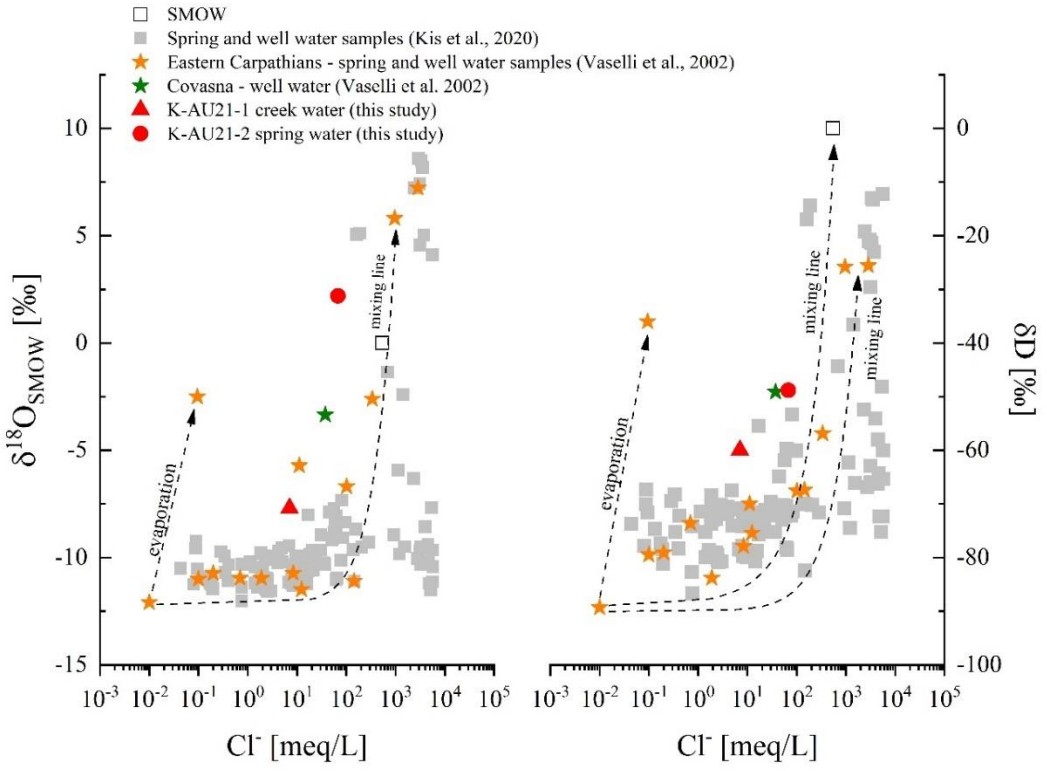

Fig. 32. Variation of isotopic composition ($\delta^{18}O$, δD) and chloride ion content of spring and creek waters in comparison to the spring and well waters from the Eastern Carpathins region and SMOW (Colpen, 1996; Kis et al., 2020; Vaselli et al., 2002).

7.2.7. Dawsonite-bearing mineral assemblage in Hankó Valley, Covasna

In this study, we focus on the role of dawsonite in the mineral assemblage in Hankó Valley and its precipitation process. Dawsonite can occur in the cracks of the brecciated sandstones, covering the rock surface and may also appear on the surface of recent, unconsolidated fluvial deposits in the creek. This observation implies that dawsonite precipitated after the above mentioned characteristic mineral assemblage. Furthermore, the appearance on the surface of the fluvial deposits indicates that dawsonite precipitation can be related to a recently ongoing process. Based on the close textural relationship between dawsonite and calcite (Fig. 13D) in brecciated sandstone, namely that dawsonite started to consume the calcite, indicates that dawsonite formed subsequent to calcite precipitation.

Besides dawsonite, another Al and carbonate-bearing mineral namely alumohydrocalcite, is also present in this study area. Alumohydrocalcite is a member of the dundasite [$PbAl_2(CO_3)_2(OH)_4 \times H_2O$] group (Rumsey et al., 2020), and usually forms from low-temperature hydrothermal solutions (<140 °C, Aikawa et al., 1972, Dunning, 2000, Fleischer et al., 1978). It often occurs together with dawsonite and nordstrandite [$AlOH_3$] (Aikawa et al., 1972, Dunning, 2000, Wopfner and Höcker, 1987). Alumohydrocalcite was previously described in Italy (Wopfner and Höcker, 1987), Japan (Aikawa et al., 1972), Australia (Goldbery and Loughnan, 1977) as an alteration product of dawsonite (Wopfner and Höcker, 1987). It was also mentioned that alumohydrocalcite can precipitate directly from surface solutions (Srebrodol'skiy, 1976). This close association of the two carbonates is rare (Dunning, 2000).

Dawsonite could precipitate in the study area because of the relatively high and continuous emanation of CO_2. On one hand, this provides the source of CO_3^- for carbonate minerals, and on the other hand its dissolution makes the waters aggressive to be able to interact with the alumina-bearing minerals (e.g., feldspar or kaolinite) from the debris of the local flysch rock. Alumohydrocalcite probably formed as an alteration product of dawsonite close to and on the surface of the flysch debris. Alternatively, dawsonite and alumohydrocalcite could precipitate in the same low-temperature processes and from the same CO_2-rich solution in the Hankó Valley. It was assumed that these two minerals formed in another most likely subsequent process than that developing the arsenic minerals which related to low-temperature hydrothermal alteration in the flysch. The

formation of these two minerals, namely dawsonite and alumohydrocalcite can be related to the recent and continuous CO_2 emanation.

7.2.8. Estimation of formation temperature of carbonates

The formation temperature of dawsonite (and its mineral assemblage) is unknown, in addition, the paragenetic sequence of the minerals has not been identified in this area previously. Therefore, in this section we attempt to estimate the formation temperature of the studied mineral assemblage (i.e., calcite, dawsonite).

For this purpose, three methods were applied. First, the studied spring water chemistry was used which is assumed to be equilibrated with the rocks of the underlying flysch sequence. Following, the method published by Giggenbach (1988), the Na^+, Mg^{2+}, K^+ concentrations of the studied waters were utilized (Fig. 33). According to the geothermometric evolution of water samples, the creek water data fall in the immature water zone therefore is not suitable to determine the temperature (Fig. 33). However, the studied spring water data fall in the partial equilibrium-dilution zone and its K/Mg equilibrium temperature is around 110 °C, meanwhile the Na/K geothermometer defines temperatures around 170 °C. Previously published Covasna well waters (Georgescu, 1976) also fall close to the creek water data, except one. One data point out of the seven, falls on the border of the immature waters zone and the partial equilibrium dilution zone (Fig. 33).

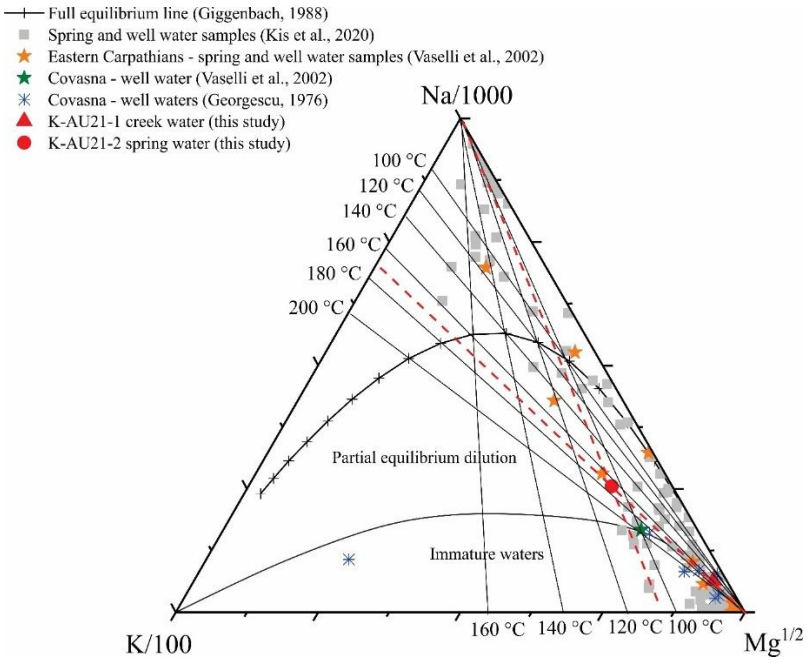

Fig. 33. Geothermal evolution of waters in the Eastern Carpathians (Giggenbach, 1988; Kis et al., 2020; Georgescu, 1976; Vaselli et al., 2002).

Second method is based on the mineral association characteristic in the study area. The calcite-aragonite-realgar-pyrite-marcasite mineral association usually forms in low-temperature hydrothermal systems, which means that the formation temperature of the minerals is below 200 °C (Kristmannsdottir, 1979). The presence of alumohydrocalcite in the study area can also indicate a lower formation temperature, below 140 °C (Fleischer et al., 1978).

Finally, clumped isotope technique was used for calcite of the assemblages to get a more precise formation temperature. Only the clumped isotope composition of calcite could be measured, which yielded 143 °C (Table 20). This calcite temperature was used as a maximum value (upper limit) as the petrographic observation suggested that the dawsonite likely formed after calcite (Fig. 13D).

Additionally, the dawsonite-bearing brecciated sandstones occur on surface and dawsonite is also present in the unconsolidated fluvial deposit along the bank of the creek (Fig. 12C-F), where CO_2 emanation is current in the study area. Therefore, with the petrography and site observation, the hypothesis is that dawsonite can precipitate even under this surface environment, at very low temperatures, in recent times. Thus, lower temperature (<25 °C) origin is the most plausible. In Covasna, the annual average temperature is 7.6 °C and the average temperature in the summer is around 20 °C (Botos, 2005). The creek water temperatures vary between 1-22 °C from January to July, and the spring water temperatures are 9.5±2 °C (Table 18).

Natural dawsonite precipitation can vary in a wide temperature range (25-200 °C) at 200-2295 m depth, but mostly between 50 and 110 °C (Table S1) Baker et al., 1995; Ferrini et al, 2003; Cseresznyés et al., 2021; Gao et al., 2009; Király et al., 2017; Li and Li et a., 2017; Liu et al., 2011; Ming et al., 2017; Oelkers and Cole, 2008; Qu et al., 2022; Worden, 2006; Zhao et al., 2018; Zhou et al., 2014). Baker et al. (1995) and Ming et al. (2017) published low temperature dawsonite (25-44 °C) from natural CO_2 occurrences at shallow depths (~200-650 m). In addition, Ferrini et al. (2003) reported dawsonite-bearing realgar-orpiment deposits from Albania. This dawsonite has heavier oxygen isotope composition ($\delta^{18}O_{SMOW}$=+42.5 ‰ - +43.9 ‰; Ferrini et al., 2003) then dawsonite, which formed in Covasna ($\delta^{18}O_{SMOW}$= +40.7 ‰ - +46.7 ‰) and also higher formation temperature (<85 °C).

To summarize, clumped isotope analysis of calcite determined the maximum formation temperature of 143 °C, which agrees with the estimation based on the studied

spring water composition (between 110 °C and 170 °C). Moreover, we argue that the formation temperature of dawsonite can be as low as 25 °C.

7.2.9. Characterization of the parental fluids of dawsonite

7.2.9.1. Source of CO_2

As demonstrated in the case of Mihályi-Répcelak and Ölbő, the $\delta^{13}C$ of CO_2 can be used to trace the origin of the fluid, since different CO_2 reservoirs worldwide can be characterized by distinct stable carbon isotope compositions (Craig, 1953; Hoefs, 1997; Ohmoto and Rye, 1979; Fig 34). To determine the origin of the CO_2 during carbonate formation (dawsonite and calcite), the measured carbon isotope data and the fractionation equations were applied. The measured carbon isotope value of calcite ($\delta^{13}C_{PDB}$: –1.50 ‰, $\delta^{18}O_{SMOW:}$ +24.04 ‰) and the determined formation temperature of calcite (143 °C) were used for the calculation of the carbon isotope composition of CO_2 in equilibrium during calcite formation. Ohmoto and Rye (1979) calcite-CO_2 fractionation equation was applied, the calculated $\delta^{13}C_{CO2}$ is –3.3 ‰ at 143 °C (Table 24).

Table 24. Calculated $\delta^{13}C$ of CO_2 in equilibrium with dawsonite and calcite from Covasna at different temperatures (7.6 – 170 °C). Daw: dawsonite, Cc: calcite, ND: not determined.

Rock sample	Separated phase	$\delta^{13}C$ of CO_2 [‰, PDB]					
		T=7.6 °C	T=20 °C	T=70 °C	T=110 °C	T=143 °C	T=170 °C
KOV-8	Daw	-3.4	-2.1	2.5	5.2	6.8	7.9
KOV-10	Daw	-4.0	-2.6	2.0	4.6	6.3	7.4
KOV-10/1	Daw	-3.8	-2.4	2.2	4.8	6.5	7.6
KOV-12	Daw	-4.1	-2.7	1.9	4.5	6.2	7.3
KOV-12/2/1	Daw	-3.0	-1.6	3.0	5.6	7.3	8.4
KOV-12/2/2	Daw	-3.6	-2.3	2.3	5.0	6.6	7.7
KOV-12/2/3	Daw	-2.0	-0.7	3.9	6.6	8.3	9.3
KOV-2G/1	Daw	-2.6	-1.3	2.0	4.6	6.3	7.4
KOV-2G/2	Daw	-3.6	-2.3	3.3	6.0	7.7	8.7
KOV-2G/3	Daw	-1.9	-0.6	2.3	5.0	6.7	7.7
KOV-2G/4	Daw	-3.8	-2.4	4.0	6.7	8.3	9.4
KOV-2G/5	Daw	-3.0	-1.7	2.1	4.8	6.5	7.5
KOV-2B/1	Daw	-4.0	-2.6	2.9	5.6	7.2	8.3
KOV-10/1 Cc	Cc	ND	ND	ND	ND	-3.3	ND

For the calculation of $\delta^{13}C_{CO2}$ in equilibrium with dawsonite, the following temperature values were used: 7.6, 20, 70, 110, 143, 170 °C (Table 24). As in section 6.2.2, the measured carbon isotope values of dawsonite were used to calculate the carbon isotope composition of CO_2 in equilibrium during dawsonite formation. Calcite-CO_2 fractionation equation (Ohmoto and Rye, 1979) was also applied at different temperatures

according to Baker et al. (1995), because the dawsonite-CO_2 fractionation is unknown yet (Cseresznyés et al., 2021). The calculated $\delta^{13}C_{CO2}$ are between –4.1‰ and –1.9 ‰ at 7.6 °C and vary from –2.7 ‰ to –0.6 ‰ at 20 °C (Table 24). The calculations using higher temperature values (70-170 °C) give significantly higher $\delta^{13}C_{CO2}$ values (from +1.9 ‰ to +9.4 ‰).

Based on the calculated stable isotope composition, more scenarios can be assumed. One option is that the two carbonate minerals, calcite and dawsonite, precipitated at the same time and temperature (143 °C). According to this hypothesis, the $\delta^{13}C_{CO2}$ value calculated from calcite is -3.3 ‰, whereas the $\delta^{13}C_{CO2}$ value calculated from dawsonite ranging between +6.2 and +8.3 ‰ at 143 °C (Table 24). These large differences can be explained in two ways: 1) the sources of the CO_2 from which these minerals formed, are different; 2) the $\delta^{13}C$ of CO_2 changed somehow more than 10 ‰ between the formation of the two minerals. The $\delta^{13}C_{CO2}$ values from free CO_2 of mineral water and mofettes, CO_2-rich gas pools, CO_2-rich well waters in the Eastern Carpathians region are ranging from –6.0 ‰ to +2.0 ‰ (Crăciun et al. 1989) or are characterized by even more negative isotope composition (from –24.59 ‰ to –1.40 ‰; Frunzeti, 2013; Italiano et al., 2017; Kis et al., 2019; Vaselli et al., 2002). Because these values are significantly lower than those from which dawsonite formed (in the current scenario), a CO_2 source with extraordinary $\delta^{13}C$ should be expected. In the second case, a process should be assumed which can significantly shift the $\delta^{13}C$ values of the CO_2 to positive direction. However, such process is not known. In addition, up to now, there is no data published, even from wider area, that can prove the presence of CO_2 with high $\delta^{13}C$ values (i.e. +6.2 ‰ - +8.3 ‰). The majority of the published $\delta^{13}C_{CO2}$ values are characterized by much lower values. Therefore, it can be argued that the calcite and dawsonite most likely formed at different temperatures.

Thus, this alternative scenario implies that these two minerals were formed in different processes, at different temperature levels and times. If much lower formation temperature is assumed for dawsonite (7.6 °C and 20 °C) than that determined for calcite (i.e. 143 °C), the $\delta^{13}C_{CO2}$ values calculated from dawsonite are between –4.1 ‰ and –0.6 ‰ at 7.6 °C and 20 °C. These values fall in the same range as the $\delta^{13}C_{CO2}$ values calculated from calcite (–3.3 ‰, Table 24). These data overlap with the published $\delta^{13}C$ values from CO_2 mofettas in the surrounding area from springs with associated CO_2 bubbling, CO_2-rich gas pools and well waters in Eastern Carpathians. (Fig. 34; Crăciun et al. 1989; Vaselli et al. 2002; Frunzeti, 2013; Kis et al., 2019). In addition, these values

are also close to those assumed to be mantle-derived CO_2 ($\delta^{13}C$= –8 ‰ and –4 ‰; Ohmoto and Rye, 1979) and overlap with the estimation for the European Subcontinental Lithospheric Mantle (–3.9 ‰ - –2.1 ‰; Weinlich et al., 1999). It can be concluded that dawsonite and calcite formed from an identical CO_2 source at different times and at different temperature levels.

The origin of the CO_2 in the study area and its vicinity is not straightforward, several explanations have been invoked, 1: mantle/magmatic; 2: hydrothermal metamorphism of marine carbonates; 3: vicinity of hydrocarbon field (Barnes et al., 1988; Javoy et al., 1982; Kis et al., 2019; Rollinson, 1993; Vaselli et al., 2002). Moreover, recent studies dealing with noble isotopes besides CO_2 suggest significant magmatic contributions to the CO_2 gas observed in Covasna and Eastern Carpathians (Italiano et al., 2017; Kis et al., 2019; Vaselli et al., 2002). The results of this study also support magmatic origin. In summary, it can be concluded that dawsonite and calcite probably formed from the same CO_2 source at different time; and the carbon isotope composition of this CO_2 overlaps with emanating CO_2 in Covasna and likely has a magmatic related origin.

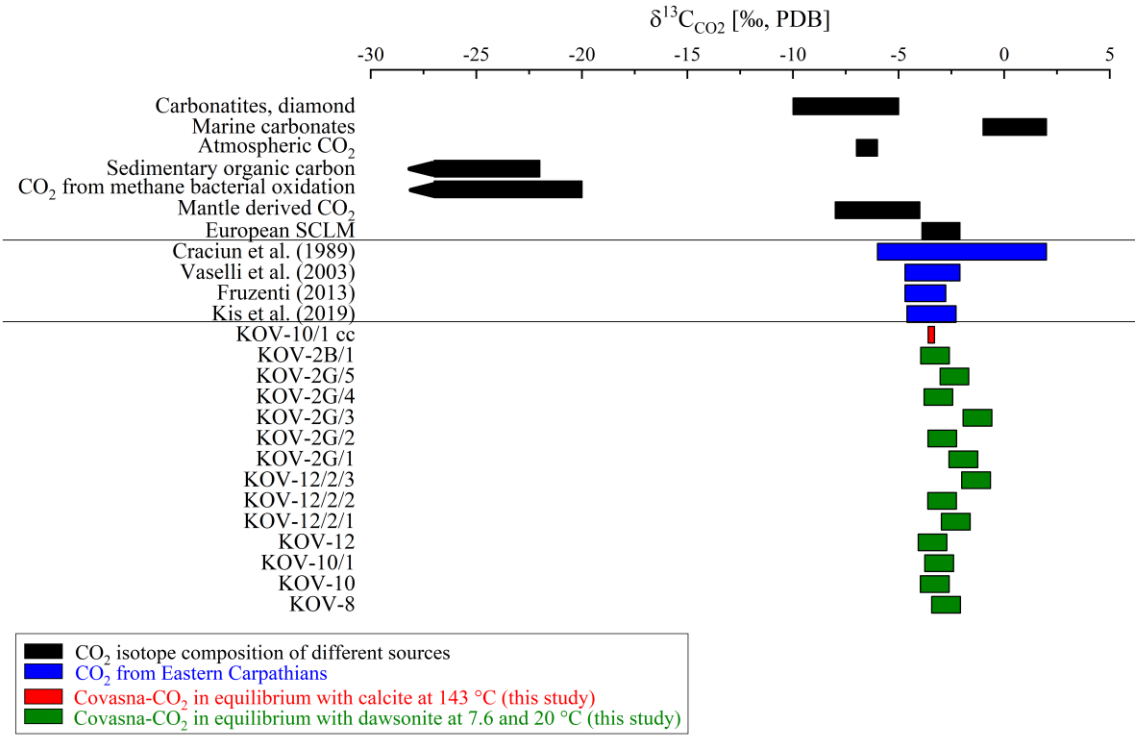

Fig. 34. Calculated $\delta^{13}C_{CO2}$ in equilibrium with separated dawsonite from Covasna compared to the carbon isotopes of local CO_2 degassing and a selection of carbonate reservoirs worldwide (Craig, 1953; Hoefs, 1997; Ohmoto and Rye, 1979; Crăciun et el., 1989; Frunzeti, 2013; Kis et al., 2020; Vaselli et al., 2002; Weinlich et al., 1999).

7.2.9.2. Origin of H_2O

In order to determine the origin of the H_2O in the fluid which was in equilibrium when dawsonite formed in the study area, it is necessary to define the mineral-water fractionation equation and the formation temperature. The gibbsite-water fractionation equation is fair approximation according to Cseresznyés et al. (2021) and can be utilized to estimate the stable isotope composition of H_2O presence during dawsonite formation. For the calculation at the two different temperatures (7.6 °C and 20 °C; see section 7.2.9.1.) the fractionation factor (0.995±0.003) of Vitali et al. (2001) for hydrogen was used, which was defined at lower temperature range (8-27 °C). The estimated hydrogen isotope composition of the water varies between –55 ‰ and –37 ‰ (Table 25). In case of the oxygen, the oxygen isotope composition of water was also estimated, which was in equilibrium with dawsonite when it was formed, using the calcite-water fractionation factor of O'Neil et al. (1969). The calculated oxygen isotope composition of the porewater ranges from +7.6 to +13.3 ‰ at 7.6 °C and from +10.5 ‰ to +16.3 ‰ at 20 °C (Table 26). The oxygen isotope composition of H_2O in equilibrium with calcite was also calculated using the calcite-water fractionation equation of O'Neil et al. (1969) for the temperature of 143 °C (obtained from clumped isotope analyses). The obtained result (+10.7 ‰, Table 26) is very similar to that of dawsonite. This suggests that not only the CO_2 but the H_2O can have also similar isotopic composition during calcite and dawsonite formation.

Table 25. Estimated δD values of porewater from separated dawsonite calculated with gibbsite-H_2O fractionation factor (0.995±0.003) at low temperature (8-27 °C) based on Vitali el al. (2001). Daw: dawsonite.

Rock sample	Separated phase	δD of porewater [‰, SMOW] at 8-27 °C
KOV-8	Daw	-49
KOV-10	Daw	-50
KOV-10/1	Daw	-46
KOV-12	Daw	-43
KOV-12/2/1	Daw	-44
KOV-12/2/2	Daw	-45
KOV-12/2/3	Daw	-42
KOV-2G/1	Daw	-39
KOV-2G/2	Daw	-37
KOV-2G/3	Daw	-38
KOV-2G/4	Daw	-40
KOV-2G/5	Daw	-43
KOV-2B/1	Daw	-42

Table 26. Calculated $\delta^{18}O$ of porewater in equilibrium with dawsonite and calcite at different temperatures (7.6, 20 and 143 °C) used O'Neil et al. (1969) fractionation equation. Daw: dawsonite, Cc: calcite, ND: not determined.

Rock sample	Separated phase	$\delta^{18}O$ of porewater [‰, SMOW]		
		T=7.6 °C	T=20 °C	T=143 °C
KOV-8	Daw	10.9	13.9	ND
KOV-10	Daw	7.6	10.5	ND
KOV-10/1	Daw	10.8	13.8	ND
KOV-12	Daw	11.3	14.2	ND
KOV-12/2/1	Daw	11.6	14.5	ND
KOV-12/2/2	Daw	9.9	12.9	ND
KOV-12/2/3	Daw	11.9	14.8	ND
KOV-2G/1	Daw	11.6	14.5	ND
KOV-2G/2	Daw	11.7	14.7	ND
KOV-2G/3	Daw	12.8	15.8	ND
KOV-2G/4	Daw	12.4	15.3	ND
KOV-2G/5	Daw	13.3	16.3	ND
KOV-2B/1	Daw	11.3	14.2	ND
KOV-10/1 cc	Cc	ND	ND	10.7

The calculated data from dawsonite are plotting in the metamorphic water field (δD: –70 to –20 ‰, $\delta^{18}O$: +5 to +25 ‰; Taylor, 1974), close to the boundary of metamorphic-magmatic waters that might indicate a contribution of metamorphic-magmatic H_2O (Fig. 31). The calculated porewater hydrogen isotope compositions from dawsonite (–55 ‰ - –37 ‰) are very close to the measured recent spring water δD values (–50.9 ‰ - –48.4 ‰) from this study (Fig. 31). In contrast, the oxygen isotope composition of water, which was calculated from dawsonite (+7.6 ‰ - +16.3 ‰) differs from the measured oxygen isotope composition of the recent studied spring waters (– 2.4 ‰ – +3.1 ‰) showing more positive delta values. The greater $\delta^{18}O$ values, beside the water rock interaction, can also be related to the enhanced isotope exchange between CO_2 and H_2O.

8. New scientific results

1. The Ölbő and Mihályi-Répcelak areas, as natural laboratories, provided the opportunity to investigate the same sandstone formation which was not flooded naturally by large amount of CO_2 (Ölbő), and compare with a flooded one (Mihályi-Répcelak). The comparison of the petrographic and geochemical features revealed which processes are a response or partially connected to the CO_2 flooding. Dawsonite is missing in the investigated Ölbő sandstone and siltstone samples based on the petrographic investigation and phase analysis (XRD, ATR-FTIR). In Mihályi-Répcelak area dawsonite formation was induced by CO_2 flooding in the sandstone reservoir and it can form in the microenvironments in conglomerates as well (Forray et al., 2021). The CO_2-flooding related dissolution process can explain the considerable difference in feldspar and calcite content of sandstones in the two areas. Moreover, the higher abundance of ankerite+siderite associations in Mihályi-Répcelak also suggest that some part of ankerite+siderite could have precipitated during/after the CO_2 inflow. The absence of a second generation of kaolinite in Ölbő field, which probably precipitated after the CO_2 flooding similarly to dawsonite in Mihály-Répcelak area, reinforces the differences between the two studied fields. Geochemical models (PHREEQC) support most of the petrographic observations of the sandstones. According to the kinetic-batch models, the majority of these reactions takes place in the early stages (first 30 years) after CO_2 injection.

2. Based on experiments the widely used sequential acid extraction method is not suitable to determine the stable C and O isotopic composition of different carbonate phases from bulk rock. After 6 hours (for calcite), 24 h (for dawsonite) and 48 h (for ankerite) reaction time, the isotopic compositions were not representative for these carbonate minerals. Isotopic analysis of separated minerals is suggested to gain meaningful data (Cseresznyés et al. 2021). For the preparation of carbonate separates, freezing-melting method is advised because it preserves the shape of the minerals, in contrast to crushing and grinding, which makes easier the hand-picking and the magnetic separation.

3. The origin of dawsonite and its parental fluid can be determined by utilizing the carbon isotope composition of dawsonite. The calculated $\delta^{13}C_{CO2}$ values (–4.8 ‰ - –2.0 ‰) in equilibrium with dawsonite in Mihályi-Répcelak overlap with those that are

characteristics for mantle/magmatic derived carbon sources and they agree well with the estimation of the European subcontinental lithospheric mantle (SCLM: – 3.9 ‰ - –2.1 ‰). The isotope values of dawsonite suggest magmatic origin for the majority of the CO_2 from which dawsonite crystallized (Cseresznyés et al., 2021).

4. Siderite appears both in the sandstones of Ölbő and Mihályi-Répcelak. It occurs in large patches in both areas, but the Mihályi-Répcelak area shows textures of simultaneous formation with dawsonite. Based on the calculated $\delta^{13}C_{CO2}$ values in equilibrium with siderite in Mihályi-Répcelak, siderites can be discriminated into two groups. In the Group-1 samples, the calculated $\delta^{13}C_{CO2}$ values in equilibrium with siderite (–6.0 ‰ - –3.9 ‰) fall closer to the calculated values from dawsonites and to the European SCLM. This means that, at least one part of the siderite has precipitated as an effect of CO_2 flooding. The inter-mixed of texture dawsonite and siderite in these sandstones also supports this scenario (Cseresznyés et al., 2021). However, in case of Group-2, the calculated $\delta^{13}C_{CO2}$ values (–8.4 ‰ - –6.1 ‰) are significantly lighter than those calculated from dawsonites and lighter than what was observed in the free CO_2 gas. The calculated $\delta^{13}C_{CO2}$ values (–10.9 ‰ - –6.5 ‰) of siderite from Ölbő overlap with these siderites in Group-2. Thus, the presence of two siderite groups (with distinct isotopic composition) in Mihályi-Répcelak area together with their textural and petrographic features indicate that some part of the siderite could have formed before CO_2 flooding, thus likely represent an early diagenetic mineral, similarly to siderite found in the unflooded Ölbő sandstones.

5. Dawsonite provided an exceptional opportunity to determine the origin of pore water during CO_2 flooding as, besides oxygen, it contains hydrogen within its structural OH^-, and the hydrogen isotope composition of dawsonite has not been determined so far. The results represent the first reported δD values of dawsonite. The estimated stable isotope composition of H_2O present during dawsonite formation in Mihályi-Répcelak (δD: –103 ‰ - –74 ‰, $\delta^{18}O_{SMOW}$: –1.4 ‰ - +4.7 ‰ at 70 °C and 98 °C, respectively) (Cseresznyés et al. 2021) indicate that the parent fluid was meteoric water modified by water-rock interaction.

6. The hydrogeochemical facies of CO_2-rich creek and spring water, along the creek of Hankó Valley in Covasna (Romania) is sodium bicarbonate type. According to the stable hydrogen and oxygen isotope analyses, the creek water has meteoric origin (δD:

–79.7 ‰ to –56.8 ‰, $\delta^{18}O_{SMOW}$: –10.9 ‰ to –7.4 ‰) meanwhile the spring water shows a mixed origin (δD: –50.9 ‰ to –48.4 ‰, $\delta^{18}O_{SMOW}$: –0.1 ‰ to +2.5 ‰). The higher $\delta^{18}O$ values of the spring water might be related to enhanced water-rock interaction and isotope exchange between CO_2 and H_2O. The detailed petrographic investigation indicates recent surface precipitation of dawsonite in a low-temperature environment (<25 °C). The $\delta^{13}C_{CO2}$ values calculated from dawsonite are between – 4.1 ‰ and –0.6 ‰, in the same range as the $\delta^{13}C_{CO2}$ values calculated for calcite (– 3.3 ‰) found in the dawsonite-bearing rocks. These values agree with the estimated $\delta^{13}C$ value of the European SCLM, implying a magmatic CO_2 source. This means that although dawsonite and calcite formed at different temperatures (environments) and times, their parental CO_2 has same magmatic origin. The calculated δD and $\delta^{18}O$ values of dawsonite show similar shift as the spring water, meaning that the formation of dawsonite is related to the spring water and the magmatic CO_2 degassing.

9. Summary

Mineral storage of CO_2 is the most promising way to the long-term underground storage of CO_2. Investigation of natural CO_2 occurrences can help to better understand what processes can take place during a CO_2 injection project. Dawsonite is [$NaAlCO_3(OH)_2$] believed to be a mineral sink of CO_2 which can precipitate as a response of large amount of CO_2 inflow. Three areas (Mihályi-Répcelak, Ölbő; Covasna) were investigated in the Pannonian Basin, which are related to either CO_2 flooding of the rocks or to a continuous CO_2 emanation. The determination of stable isotope composition of carbonates is a widely used way to reveal the origin of their source fluid. Unfortunately, the separation of carbonates from rocks containing a complex carbonate assemblage is not possible with the widely used sequential acid extraction method. However, mineral separates proved to be an excellent tool to gain reliable isotopic results for the different carbonates.

Dawsonite and siderite were separated from the sandstones of Mihályi-Répcelak and Ölbő fields for C and O isotope analyses. The CO_2 that precipitated as dawsonite seems to be magmatic in origin having also similar isotopic composition to that of European Subcontinental Lithospheric Mantle. In contrast, the isotopic signature of siderite suggests that it was partially formed as a response to CO_2 flooding, the rest being an early diagenetic mineral. The isotopic composition of siderite present in the unflooded Ölbő sandstones also supports this scenario. To better understand the processes in these sandstones, geochemical models were created. The Ölbő and Mihályi-Répcelak areas, as natural laboratories, provided an opportunity to validate these geochemical models, both before interaction with CO_2 (Ölbő samples) and after millions of years being in contact with CO_2 (Mihályi-Répcelak samples). The models shown that most observed reactions can happen just 30 years after CO_2 injection.

In the Covasna area dawsonite formation is observed in surface environment. Mineral separates (dawsonite, calcite) and surface water samples were used to determine their isotopic composition. The creek water has meteoric origin, meanwhile the spring water shows a mixed origin. Occurrence of dawsonite indicates recent surface precipitation, in a low-temperature process (<25 °C). Dawsonite precipitation is probably related to the continuous CO_2 degassing which originates from the magma. Calcite and dawsonite precipitated from the same CO_2 source, but in different processes and time. Dawsonite precipitated from the spring water and the continuous CO_2 outflow, which caused a positive shift in the oxygen isotope composition of the spring water.

9.1. Összefoglalás

A CO_2 ásványos formában történő megkötése az egyik legígéretesebb módja a CO_2 hosszú távú felszín alatti elhelyezésének. A természetes CO_2 előfordulások vizsgálata segíthet megérteni, hogy milyen folyamatok játszódhatnak le a CO_2 geológiai tárolása során. A dawsonit [$NaAlCO_3(OH)_2$], amely nagy mennyiségű CO_2 beáramlás hatására válhat ki a homokkő rezervoárokban a CO_2 egyik megkötési formája lehet. A Pannon-medencében három olyan területet (Mihályi-Répcelak, Ölbő és Kovászna) vizsgáltam, ahol a kőzeteket természetes módon CO_2 árasztotta el, vagy folyamatos CO_2 kiáramlásnak vannak kitéve. A karbonátok stabilizotóp-összetételének meghatározása széles körben alkalmazott módszer a fluidumok eredetének felfedésére. A különböző karbonátok izotópösszetételének meghatározása az elterjedten alkalmazott szakaszos feltárással nem lehetséges olyan kőzetekben, amelyek komplex karbonátegyüttest tartalmaznak. Azonban az ásványszeparátumok kiválóan használhatók, hogy megbízható izotópösszetételt kapjunk a különböző karbonátokra.

A mihályi-répcelaki és ölbői homokkövekből dawsonitot és szideritet szeparáltam stabil C- és O-izotópelemzések céljából. Az eredmények alapján a dawsonit magmás eredetű CO_2-ból származik. A dawsonit kiválása a mihályi-répcelaki természetes CO_2 előfordulásban magmás CO_2 beáramláshoz köthető. Ezzel szemben a sziderit izotópösszetétele arra utal, hogy csak részben képződött a CO_2 beáramlás hatására, egy része diagenetikus eredetű. A sziderit megjelenése és izotópösszetétele az ölbői homokkőben is ezt az eredetet támasztja alá. A tanulmányozott homokkövekben lejátszódó folyamatok jobb megértésének érdekében geokémiai modelleket is alkalmaztam. A mihályi-répcelaki és ölbői területek, mint természetes laboratóriumok lehetőséget biztosítottak a geokémiai modellek eredményeinek ellenőrzésére, hiszen a homokkövek mind a CO_2-vel való kölcsönhatás előtt (ölbői minták), mind azután több millió évvel (mihályi-répcelaki minták) tanulmányozhatók voltak.

Kovászna térségében a dawsonit felszíni körülmények között található meg. Ásványszeparátumok (dawsonit, kalcit) és felszíni vízminták izotópösszetételét meghatározva vizsgáltam ezen képződési környezetet. A patakvíz izotópösszetétele alapján meteorikus, míg a vizsgált forrásvíz kevert eredetet mutat. A kovásznai dawsonit vizsgálata a közelmúltban történt alacsony hőmérsékletű (<25 °C) felszíni képződésre utal. A dawsonit kiválása feltehetőleg a magmás eredetű folyamatos CO_2 kiáramláshoz kapcsolódik. A dawsonit és kalcit ezen CO_2-forrásból csapódott ki, de különböző folyamatok során, eltérő időben. A dawsonit a részben a forrásvízből és a folyamatos,

magmás eredetű CO_2 kiáramlás hatására vált ki, ami a forrásvíz oxigénizotóp-összetételének pozitív eltolódását is okozta.

10. Acknowledgements

First of all, I would like to say thanks to my supervisors, György Falus and György Czuppon. György Falus introduced the topic of CCS to me during my B.Sc. studies and gave the opportunity to be part of his CCS team. György Czuppon led me through the adventurous road of stable isotopes from analyses through data evaluation to interpretation. They co-supervised me together on my way since 2016 and enriched my knowledge continuously. I am very grateful for all of their advice, the consultations (often in the late evening) and that they sacrificed part of their free time for this project. I would like to say thanks to my consultants Csilla Király and Csaba Szabó who opened my mind and introduced me to the world of geochemistry, petrology and environmental geology. I also owe them a debt of gratitude for their continuous support in scientific and personal life as well.

I am very thankful for the CCS team: to Zsuzsanna Szabó-Krausz, who taught me the geochemical modelling and its secrets, to Ágnes Szamosfalvi for her kind and endless help and encouragement. I also thank Viktória Forray, with who we helped and contested each other during our studies to always be better. I am also very grateful to Domokos Györe for sharing his motivation with me, he could always show another perspective of research to enrich my knowledge and help to develop. He helped me to dream bigger and to be open to the world.

I would like to say thanks to Ágnes Gál and András Papucs for the collection of dawsonite-bearing rocks and waters in Covasna, for leading me on the field, and for their shared knowledge, geological maps and data. I am also thankful to everyone in the TopoTransylvania group, who collected further samples for me, and special thanks to István J. Kovács who taught me the basics of infrared spectroscopy.

I would like to thank to Attila Demény who sponsored the isotope analyses in the Institute for Geological and Geochemical Research, supported this project and gave great advice for my first manuscript. Special thanks for the cooperation and data to Tibor Egyházi from Linde Gas Hungary and the team of the Messer Hungarogáz Ltd.

I would like to thank all the technical support, measurements and data evaluation to Péter Kónya (XRD), Ivett Kovács, Viktória Mozgai (XRD and micro-XRD), László E. Aradi (Raman microspectroscopy), Miklósné Bátori (magnetic separation), István Hegyi

(isotope analysis), Bence Reitmeyer (isotope analysis), László Rinyu (clumped isotope analysis), István Lakos (water analysis), Martin Dietzel and Bettina Purgstaller (dawsonite synthesis and consultations).

My research was part of project no. KDP-2020-971244 has been implemented with the support provided by the Ministry of Culture and Innovation of Hungary from the National Research, Development and Innovation Fund, financed under the KDP-2020 funding scheme. I was also supported by the AAPG Foundation Grants-in-Aid, financed by the J. Elmer Thomas Memorial Grant. I was further supported by the Doctoral School of Environmental Sciences at ELTE. The study was carried out in collaboration between ELTE and SARA (contract numbers: TTK 2461/1/2013 and MBFSZ 206-114/2013). This work could not have been completed without the financial support of the OTKA program (K-131353 to György Falus) of the National Research, Development and Innovation Office of Hungary. The research was also granted by the ELTE Institutional Excellence Program (1783-3/2018/FEKUTSRAT) of the Hungarian Ministry of Human Capacities and ELTE Research and Industrial Relations Center (RIRC) (KMOP project number 4.2.1 / B-10 - 2010-002).

Thanks to Márti and Tibi who gave me the opportunity to buy a new computer in the middle of my PhD studies. I also owe a debt of gratitude for Orsi and Tomi (‘a bizottság’), Gorkhi, Thomas, Kavics, Dava, Nelson, Levike, Ábi and all the LRG members who helped me on my way and worked (like crazy) together since 2015.

I am very grateful to Laci for the continuous mental support, endless patience and help during the preparation of the thesis and for his great advice. Finally, I would like to say thank you to my Family that they supported my long study journey from the back with endless support and love.

11. References

Aikawa, N., Yoshida, M., Ichikawa, K., 1972. Discovery of Dawsonite and Alumohydrocalcite From the Cretaceous Izumi Group in Osaka Prefecture, Southwest Japan. J. Japanese Assoc. Mineral. Petrol. Econ. Geol. 67, 370–385. https://doi.org/10.2465/ganko1941.67.370

Al-Aasm, I.S., Taylor, B.E., South, B., 1990. Stable isotope analysis of multiple carbonate samples using selective acid extraction. Chem. Geol. Isot. Geosci. Sect. 80, 119–125. https://doi.org/10.1016/0168-9622(90)90020-D

Anderson, N.T., Kelson, J.R., Kele, S., Daëron, M., Bonifacie, M., Horita, J., Mackey, T.J., John, C.M., Kluge, T., Petschnig, P., Jost, A.B., Huntington, K.W., Bernasconi, S.M., Bergmann, K.D., 2021. A Unified Clumped Isotope Thermometer Calibration (0.5–1,100°C) Using Carbonate-Based Standardization. Geophys. Res. Lett. 48, 1–11. https://doi.org/10.1029/2020GL092069

Aradi, L.E., Berkesi, M., Szabó, C., 2019. Amfibol-gazdag harzburgit xenolit fluidumzárvány vizsgálata a Stájer-medencéből. Földtani Közlöny 149, 35–49. https://doi.org/10.23928/foldt.kozl.2019.149.1.35

Assonov, S.S., Brenninkmeijer, C.A.M., 2003. A redetermination of absolute values for $^{17}R_{VPDB\text{-}CO2}$ and $^{17}R_{VSMOW}$. Rapid Commun. Mass Spectrom. 17, 1017–1029. https://doi.org/10.1002/rcm.1011

Bachu, S., Bonijoly, D., Bradshaw, J., Burruss, R., Holloway, S., Christensen, N.P., Mathiassen, O.M., 2007. CO_2 storage capacity estimation: Methodology and gaps. Int. J. Greenh. Gas Control 1, 430–443. https://doi.org/10.1016/S1750-5836(07)00086-2

Baertschi, P., 1976. Absolute ^{18}O content of standard mean ocean water. Earth Planet. Sci. Lett. 31, 341–344. https://doi.org/10.1016/0012-821X(76)90115-1

Baker, J.C., Bai, G.P., Hamilton, P.J., Golding, S.D., Keene, J.B., 1995. Continental-Scale Magmatic Carbon Dioxide Seepage Recorded by Dawsonite in the Bowen-Gunnedah-Sydney Basin System, Eastern Australia. J. Sediment. Res. 65, 522–530. https://doi.org/10.1306/d4268117-2b26-11d7-8648000102c1865d

Balázs E., Nusszer A., 1987. Magyarország medenceterületeinek kunsági (pannoniai s. str.) emeletbeli vulkanizmusa. MÁFI Évk., LXIX, 95-103.

Balogh, K., Jámbor, A., Partényi, Z., Ravasz-Baranyi, L., Solti, G., 1982. K/Ar radiogenic age of Transdanubian basalts. In: Hungarian. MÁFI Évi Jel., pp. 243-259.

Balogh, K., Árva-Sós, E., Pécskay, Z., Ravasz-Baranyai L., 1986. K/Ar dating of post-Sarmatian alkali basaltic rocks in Hungary. Acta Min. et Petr. 28, 75–94.

Bányai, J., 1933. Eltűnt a kovásznai arzénes ásványlelőhely. Székelység 3/9-10, Székelyudvarhely, 88-89.

Bányai, J. 1957. A Magyar Autonóm Tartomány hasznosítható ásványi kincsei. Tudományos Könyvkiadó, Bukarest, 78-86.

Barnes, I., Evans, W.C., White, L.D., 1988. The role of mantle CO_2 in volcanism. Appl. Geochemistry 3, 281–285. https://doi.org/10.1016/0883-2927(88)90107-2

Baudrand, M., Aloisi, G., Lécuyer, C., Martineau, F., Fourel, F., Escarguel, G., Blanc-Valleron, M.M., Rouchy, J.M., Grossi, V., 2012. Semi-automatic determination of the carbon and oxygen stable isotope compositions of calcite and dolomite in natural mixtures. Appl. Geochemistry 27, 257–265. https://doi.org/10.1016/j.apgeochem.2011.11.003

Bernasconi, S.M., Daëron, M., Bergmann, K.D., Bonifacie, M., Meckler, A.N., Affek, H.P., Anderson, N., Bajnai, D., Barkan, E., Beverly, E., Blamart, D., Burgener, L., Calmels, D., Chaduteau, C., Clog, M., Davidheiser-Kroll, B., Davies, A., Dux, F., Eiler, J., Elliott, B., Fetrow, A.C., Fiebig, J., Goldberg, S., Hermoso, M., Huntington, K.W., Hyland, E., Ingalls, M., Jaggi, M., John, C.M., Jost, A.B., Katz, S., Kelson, J., Kluge, T., Kocken, I.J., Laskar, A., Leutert, T.J., Liang, D., Lucarelli, J., Mackey, T.J., Mangenot, X., Meinicke, N., Modestou, S.E., Müller, I.A., Murray, S., Neary, A., Packard, N., Passey, B.H., Pelletier, E., Petersen, S., Piasecki, A., Schauer, A., Snell, K.E., Swart, P.K., Tripati, A., Upadhyay, D., Vennemann, T., Winkelstern, I., Yarian, D., Yoshida, N., Zhang, N., Ziegler, M., 2021. InterCarb: A Community Effort to Improve Interlaboratory Standardization of the Carbonate Clumped Isotope Thermometer Using Carbonate Standards. Geochemistry, Geophys. Geosystems 22, 1–25. https://doi.org/10.1029/2020GC009588

Bernasconi, S.M., Müller, I.A., Bergmann, K.D., Breitenbach, S.F.M., Fernandez, A., Hodell, D.A., Jaggi, M., Meckler, A.N., Millan, I., Ziegler, M., 2018. Reducing Uncertainties in Carbonate Clumped Isotope Analysis Through Consistent Carbonate-Based Standardization. Geochemistry, Geophys. Geosystems 19, 2895–2914. https://doi.org/10.1029/2017GC007385

Bickle, M., Kampman, N., Wigley, M., 2013. Natural Analogues 77, 15–71.

Bielz, E.A., 1889. Die in Siebenbürgen vorkommenden Mineralien und Gesteine nach den neuesten Untersuchungen revidiert und zusammengestellt – Verh. u. Mitth. d. siebenbürg. Ver. f. Nat. wiss. z. Hermannstadt, XXXIX., 1–82. o., Hermannstadt.

Boschetti, T., Angulo, B., Cabrera, F., Vásquez, J., Montero, R.L., 2016. Hydrogeochemical characterization of oilfield waters from southeast Maracaibo Basin (Venezuela): Diagenetic effects on chemical and isotopic composition. Mar. Pet. Geol. 73, 228–248. https://doi.org/10.1016/j.marpetgeo.2016.02.020

Botos, A., 2005. Regionális térségjefleszẗési lehetőségek Kovászna megyében. Szent István Egyetem.

Bottinga, Y., 1968. Calculation of fractionation factors for carbon and oxygen isotopic exchange in the system calcite-carbon dioxide-water. J. Phys. Chem. 33, 49–64. https://doi.org/10.1016/0016-7037(69)90092-1

Boussaroque, J., Létolle, R., Maury, R. 1975. Formation de la dawsonite des Richát (Adrar de Maurutanie): Analyse isotopique ^{13}C et ^{18}O: Academie des Sciences (Paris), Comptes Rendus Hebdomadaires des Seances. Série D, v. 281, p. 1075-1078.

Brand, W.A., Assonov, S.S., Coplen, T.B., 2010. Correction for the ^{17}O interference in $\delta(^{13}C)$ measurements when analyzing CO_2 with stable isotope mass spectrometry (IUPAC Technical Report). Pure Appl. Chem. 82, 1719–1733. https://doi.org/10.1351/PAC-REP-09-01-05

Brownlow, A.H., 1996. Geochemistry. Prentice Hall, Upper Saddle River, New Jersey 07458.

Chang, L.L.Y., Howie, R.A. & Zussman, J. 1996. Rock-Forming Minerals, Volume 5B: Non-Silicates. Sulphates, Carbonates, Phosphates and Halides. Second Edition. The Geological Society, London, pp. 383.

Chen, C.H., Liu, K.K., Shieh, Y.N., 1988. Geochemical and isotopic studies of bauxitization in the Tatun volcanic area, northern Taiwan. Chem. Geol. 68, 41–56. https://doi.org/10.1016/0009-2541(88)90085-X

Cheng, J., Yu, H., Liu, N., Yu, Y., Ahmat, K., Zhao, R., 2022. Experimental investigation for the impact of chlorite dissolution on CO_2 mineral trapping in a sandstone-brine-CO_2 system. Greenh. Gases Sci. Technol. 12, 470–485. https://doi.org/10.1002/ghg.2163

Chesworth, W., 1971. Laboratory Synthesis of Dawsonite and its Natural Occurrences. Nat. Phys. Sci. 231, 40–41. https://doi.org/10.1038/physci231040a0

Clark, D., Ian; Fritz, P., 1997. Environmental Isotopes in Hídrogeology, 1st ed. Boca Raton, FL: CRC Press/Lewis Publishers, New York. https://doi.org/10.1201/9781482242911

Clayton R. N. Skinner H. C. W., Berner R. A., Rubinson M. 1968a. Isotopic compositions of recent South Australian lagoonal carbonates, Geochimica et Cosmochimica Acta, 32, 9, 983-988. https://doi.org/10.1016/0016-7037(68)90062-8

Clayton R. N., Jones B. F., Berner R. A. 1968b. Isotope studies of dolomite formation under sedimentary conditions. Geochimica et Cosmochimica Acta, 32,4,415-424, https://doi.org/10.1016/0016-7037(68)90076-8

Comerio, M., Morosi, M.E., Tunik, M., Paredes, J.M., Zalba, P.E., 2014. The role of telogenetic injection of magmatically derived CO_2 in the formation of dawsonite from the Castillo Formation, Chubut Group, Patagonia, Argentina. Can. Mineral. 52, 513–531. https://doi.org/10.3749/canmin.52.3.513

Coplen, T.B., 1996. New guidelines for reporting stable hydrogen, carbon, and oxygen isotope-ratio data. Geochim. Cosmochim. Acta 60, 3359–3360. https://doi.org/10.1016/0016-7037(96)00263-3

Cornides, I., Takaoka, N., Nagao, K., Matsuo, S., 1986. Contribution of mantle-derived gases to subsurface gases in a tectonically quiescent area, the Carpathian Basin, Hungary revealed by noble gas measurements. Geochem. J. 20, 119–125, https://doi.org/10.2343/geochemj.20.119.

Coveney, R.M., Kelly, W.C., 1971. Dawsonite as a daughter mineral in hydrothermal fluid inclusions. Contrib. to Mineral. Petrol. 32, 334–342. https://doi.org/10.1007/BF00373350

Crăciun, P., Barnes, I., Bandrabur, T., 1989. Stable isotopes in hydrogeothermal structures in Romania. Stud. Teh. Econ., Ser. E 15, 17–39.

Craig, H., 1953. The geochemistry of the stable carbon isotopes. Geochim. Cosmochim. Acta 3, 53–92. https://doi.org/10.1016/0016-7037(53)90001-5

Craig, H., 1961. Isotopic variations in meteoric waters. Science (80-.). 133, 1702–1703. https://doi.org/10.1126/science.133.3465.1702

Cseresznyés, D. 2018. Szén-dioxid felszín alatti tárolásához kapcsolódó karbonátok stabil izotóp összetételének meghatározása. MSc dolgozat, Eötvös Loránd Tudományegyetem, Budapest, pp. 50.

Cseresznyés, D., Czuppon, G., Király, C., Demény, A., Györe, D., Forray, V., Kovács, I., Szabó, C., Falus, G., 2021. Origin of dawsonite-forming fluids in the Mihályi-Répcelak field (Pannonian Basin) using stable H, C and O isotope compositions: Implication for mineral storage of carbon-dioxide. Chem. Geol. 584. https://doi.org/10.1016/j.chemgeo.2021.120536

Csizmeg, J., Márton, B., Szalay, Á., Vető, I., Peffer, M., Varga, G., Pogácsás, G., 2012. Neogene hydrocarbon potential and inert gas risk in the Hungarian part of Danube Basin, in: 29th IAS Meeting of Sedimentology, Sedimentology in the Heart of Alps, Schladming. Austria, p. 343.

Csontos L., Nagymarosy A., Horváth F., Kovaĉ M., 1992; Tertiary evolution of the Intra-Carpathian area: a model. In P. A. Ziegler (ed.): Geodynamics of riftingVol I. Case study on rifts: Europe and Asia. Tectonophysics, 208, 221-241. https://doi.org/10.1016/0040-1951(92)90346-8

Czuppon, G., Demény, A., Leél-Őssy, S., Óvari, M., Molnár, M., Stieber, J., Kiss, K., Kármán, K., Surányi, G., Haszpra, L., 2018. Cave monitoring in the Béke and Baradla caves (Northeastern Hungary): Implications for the conditions for the formation cave carbonates. Int. J. Speleol. 47, 13–28. https://doi.org/10.5038/1827-806X.47.1.2110

Czuppon, G., Ramsay, R.R., Özgenc, I., Demény, A., Gwalani, L.G., Rogers, K., Eves, A., Papp, L., Palcsu, L., Berkesi, M., Downes, P.J., 2014. Stable (H, O, C) and noble-gas (He and Ar) isotopic compositions from calcite and fluorite in the Speewah Dome, Kimberley Region, Western Australia: implications for the conditions of crystallization and evidence for the influence of crustal-mantle fluid . Mineral. Petrol. 108, 759–775. https://doi.org/10.1007/s00710-014-0333-7

De Silva, G.P.D., Ranjith, P.G., Perera, M.S.A., 2015. Geochemical aspects of CO_2 sequestration in deep saline aquifers: A review. Fuel 155, 128–143. https://doi.org/10.1016/j.fuel.2015.03.045

Demény, A., Czuppon, G., Kern, Z., Leél-Őssy, S., Németh, A., Szabó, M., Tóth, M., Wu, C.C., Shen, C.C., Molnár, M., Németh, T., Németh, P., Óvári, M., 2016. Recrystallization-induced oxygen isotope changes in inclusion-hosted water of speleothems – Paleoclimatological implications. Quat. Int. 415, 25–32. https://doi.org/10.1016/j.quaint.2015.11.137

Dénes, I., Zólya, L., Both, J., Papucs, A., 2005. Tanulmányok Erdély földtanából Védett földtani természeti értékek Székelyföldön 263–291.

Dövényi, P., Horváth, F., Liebe, P., Gálfi, J., Erki, I., 1983. Geothermal conditions of Hungary. Geophys. Trans. 29, 3–114.

Du, Y., Song, H., 2020. Refined protocol for δ13C analysis of calcite and dolomite in carbonate mixture samples. Rapid Commun. Mass Spectrom. 34, 1–8. https://doi.org/10.1002/rcm.8743

Dumitrescu, I., Sandulesci, M., Bandrabur, T. 1970. Harta geologică scara 1:200000 29. Covasna. Institutul Geologic, București.

Dunning, G.E., 2000. Chromian dawsonite and chromian alumohydrocalcite from Orestimba creek, Stanislaus county, California. Mineral. Rec. 31, 333–338.

Epstein, S., Graf, D.L. and Degens, E.T., 1964. Oxygen isotope studies on the origin of dolomites. In: Isotopic and Cosmic Chemistry. North Holland, Amsterdam, pp. 169-180.

Estep, P.A., Karr, C., 1968. The infrared spectrum of dawsonite. Am. Mineral. 53, 305–309.

Falus, Gy., Szamosfalvi, Á., Molnár, J., Barczikayné Szeiler, R., Szabadosné Sallay, E., Hegyiné Rusznyák, É., Gál, N.E., Pummer, T., Szabó Zs. 2016. 11/2016 számú MFGI jelentés, A hazai CO_2 tárolás lehetőségeinek vizsgálata, téradatbázisának építése – Mezőtúr-IV, 26-40.

Farmer, V.C. 1974. Mineralogical Society Monograph 4: The Infrared Spectra of Minerals. The Mineralogical Society, London 539 p.

Ferrini, V., Martarelli, L., De Vito, C., Çina, A., Deda, T., 2003. The Koman dawsonite and realgar-orpiment deposit, Northern Albania: Inferences on processes of formation. Can. Mineral. 41, 413–427. https://doi.org/10.2113/gscanmin.41.2.413

Fleischer, M., Pabst, A., White, J.S., 1978. New mineral names. Am. Mineral. 63, 793–796.

Flesch, G. D., Anderson, A. R., Svec, H. J., 1973. A secondary isotopic standard for $^{6}Li/^{7}Li$ determinations. Int. J. Mass Spectrom. Ion Phys. 12(3), 265–272. doi:10.1016/0020-7381(73)80043-9.

Földvári, M., 2011. Handbook of the thermogravimetric system of minerals and its use in geological practice, Central European Geology. https://doi.org/10.1556/ceugeol.56.2013.4.6

Fórizs, I., Makfalvi, Z., Deák, J., Kármán, K., Vallase, I., Süveges, M., 2011. Izotópgeokémiai vozsgálatok a Csíki-medence ásványvizeiben. Miskolci Egy. Közleménye 81, 59–67.

Forray, V., Király, C., Demény, A., Cseresznyés, D., Szabó, C., Falus, G., 2021. Mineralogical and geochemical changes in conglomerate reservoir rocks induced by CO_2 influx at Mihályi-Répcelak natural analogue, NW-Hungary. Environ. Earth Sci. 80, 1–12. https://doi.org/10.1007/s12665-021-10050-9

Friedman, I., O'Neil, J., Cebula, G., 1982. Two new carbonate stable isotope standards. Geostand. Newsl. 6, 11–12.

Frost, R.L., Bouzaid, J.M., 2007. Raman spectroscopy of dawsonite NaAl(CO3)(OH)2. J. Raman Spectrosc. 38, 873–879. https://doi.org/10.1002/jrs

Frost, R.L., López, A., Scholz, R., Sampaio, N.P., De Oliveira, F.A.N., 2015. SEM, EDS and vibrational spectroscopic study of dawsonite $NaAl(CO_3)(OH)_2$. Spectrochim. Acta - Part A Mol. Biomol. Spectrosc. 136, 918–923. https://doi.org/10.1016/j.saa.2014.09.114

Frueh, a J., Golightly, J.P., 1967. The crystal structure of dawsonite $NaAl(CO_3)(OH)_2$.

Frunzeti, N. 2013. Geogenic emissions of greenhouse gases in the Southern part of the Eastern Carpathians, (Doctoral dissertation), Retrieved from Faculty of Environmental Science and Engineering. Cluj-Napoca: Babes-Bolyai University. (In Romanian)

Fülöp J. 1990; Magyarország geológiája. Paleozoikum I. Földtani Intézet kiadványa, 325 pp.

Gao, Y., Liu, L., Hu, W., 2009. Petrology and isotopic geochemistry of dawsonite-bearing sandstones in Hailaer basin, northeastern China. Appl. Geochemistry 24, 1724–1738. https://doi.org/10.1016/j.apgeochem.2009.05.002

Gaus, I., Azaroual, M., Czernichowski-Lauriol, I., 2005. Reactive transport modelling of the impact of CO_2 injection on the clayey cap rock at Sleipner (North Sea). Chem. Geol. 217, 319–337. https://doi.org/10.1016/j.chemgeo.2004.12.016

Georgescu, M., Avram, E., Nedelcu, C., Flamind, L., Barbu, I., 1978. Harta hidrogeologica a zonei Covasna (Hydrogeological map of the Covasna area). Documentatie de exploatare a zăcămintelor de ape minerale și dioxid de carbon.

Giggenbach, W.F., 1988. Geothermal solute equilibria. Derivation of Na-K-Mg-Ca geoindicators. Geochim. Cosmochim. Acta 52, 2749–2765. https://doi.org/10.1016/0016-7037(88)90143-3

Gilfillan, S.M.V., Sherwood Lollar, B., Holland, G., Blagburn, D., Stevens, S., Schoell, M., Cassidy, M., Ding, Z., Zhou, Z., Lacrampe-Couloume, G. and Ballentine, C.J. 2009. Solubility trapping in formation water as dominant CO_2 sink in natural gas fields. Nature 458, 614-618, 10.1038/nature07852.

Glover, E.D., 1961. Addition to "Method of solution of calcareous materials using the complexing agent, EDTA." J. Sediment. Res. 33, 227–0. https://doi.org/10.2110/jsr.33.227

Golab, A.N., Carr, P.F., Palamara, D.R., 2006. Influence of localised igneous activity on cleat dawsonite formation in Late Permian coal measures, Upper Hunter Valley, Australia. Int. J. Coal Geol. 66, 296–304. https://doi.org/10.1016/j.coal.2005.08.001

Goldbery, R., Loughnan, F.C., 1977. Dawasonite, alumohydrocalcite, nordstrandite and gorceixite in Permian marine strata of the Sydney Basin, Australia. Sedimentology 24, 565–579.

Golyshev, S.I., Padalko, N.L., Pechenkin, S.A., 1981. Fractionation of stable oxygen and carbon isotopes in carbonate systems. Geochemistry Int. 18, 85–99.

Gonfiantini, R., Stichler, W., Rozanski, K., 1995. Standards and intercomparison materials distributed by the International Atomic Energy Agency for stable isotope measurements. In Reference and Intercomparison Materials for Stable Isotopes of Light Elements. IAEA-TECDOC-825, Vienna Int. At. Energy Agency 24, 13–29. https://doi.org/10.1016/0375-6505(95)00024-0

Gyore, D., Cseresznyés, D., Király, Cs., Szamosfalvi, Á., Szabó, Cs., Falus, Gy., Czuppon, Gy., Stuart, F. 2022. A nascent natural CO_2 reservoir: the Mihályi field, Pannonian Basin; Opportunitues for geological carbon storage. In 2022 Goldschmidt Conference.

Györe, D., Stuart, F.M., Gilfillan, S.M.V., Waldron, S., 2015. Tracing injected CO_2 in the Cranfield enhanced oil recovery field (MS, USA) using He, Ne and Ar isotopes. Int. J. Greenh. Gas Control 42, 554–561. https://doi.org/10.1016/j.ijggc.2015.09.009

Gysi, A.P., Stefánsson, A. 2011. Mineralogical aspects of CO_2 sequestration during hydrothermal basalt alteration – An experimental study at 75–250 ◦C and elevated pCO2. Chemical Geology 306–307, 146–159.

Harangi, S., Vaselli, O., Tonarini, S., Szabó, C., Harangi, R., Coradossi, N., 1995. Harangi et al ActaVolc 1995.pdf. Acta Vulcnologica 7, 173–187.

Hauer, V.F.R. 1860. Realgar, Schwefel und Aragon von Kovászna. - Jahrb. d.KK. Reichsanst. 11, Wien, 85

Hay, R.L., 1966. Zeolites and zeolitic reactions in sedimentary rocks. Geol. Soc. Am. 85, 129.

Heem, P.V.D., 1980. Preparation of dawsonite. U. S. Patent, No4, 221, 771.

Hellevang, H., Aagaard, P., Oelkers, E.H., Kvamme, B., 2005. Can dawsonite permanently trap CO2? Environ. Sci. Technol. 39, 8281–8287. https://doi.org/10.1021/es0504791

Hellevang, H., Declercq, J., Kvamme, B., Aagaard, P., 2010. The dissolution rates of dawsonite at pH 0.9 to 5 and temperatures of 22, 60 and 77°C. Appl. Geochemistry 25, 1575–1586. https://doi.org/10.1016/j.apgeochem.2010.08.007

Higgs, K.E., Haese, R.R., Golding, S.D., Schacht, U., Watson, M.N., 2015. The Pretty Hill Formation as a natural analogue for CO_2 storage: An investigation of mineralogical and isotopic changes associated with sandstones exposed to low, intermediate and high CO_2 concentrations over geological time. Chem. Geol. 399, 36–64. https://doi.org/10.1016/j.chemgeo.2014.10.019

Hlavay, J., Jonas, K., Elek, S., Inczedy, J. 1978. Characterization of the particle size and the crystallinity of certain minerals by IR spectrophotometry and other instrumental methods-II. Investigations on quartz and feldspar. Clays and Clay Minerals 26, 139-143.

Hoefs, J., 1997. Stable isotope geochemistry, fourth ed. Berlin, Springer Verlag, Berlin. https://doi.org/10.5860/choice.194065

Hoefs, J., 2009. Stable isotope geochemistry, sixth ed. Berlin, Springer Verlag, Berlin. ISBN: 978-3-030-77692-3

Hu, B., Radke, J., Schlüter, H.J., Heine, F.T., Zhou, L., Bernasconi, S.M., 2014. A modified procedure for gas-source isotope ratio mass spectrometry: The long-integration dual-inlet (LIDI) methodology and implications for clumped isotope measurements. Rapid Commun. Mass Spectrom. 28, 1413–1425. https://doi.org/10.1002/rcm.6909

Humphrey, J.D., 1988. Late Pleistocene mixing zone dolomitization, southeastern Barbados, West Indies. Sedimentology 35, 327–348. https://doi.org/10.1111/j.1365-3091.1988.tb00951.x

Incze, R., Papp, B., Burghele, B.D., Cosma, C., Gyila, S., 2016. Follow-up measurements to estimate the exposure of patients to the moffetes from Covasna county (Romania). Rom. Journ. Phys. 61, 7-8, 1320-1329.

Ionete, R.E., Popescu, R., Costinel, D., 2015. An isotopic survey of some mineral water resources in the Carpathian chain (Romania). Environ. Eng. Manag. J. 14, 2445–2456. https://doi.org/10.30638/eemj.2015.261

IPCC 2005. IPCC special report on carbon dioxide capture and storage. Metz, B., Davidson, O., de Coninck, H.C., Loos, M., Meyer, L.A. (Eds.), Prepared by Working Group III of the Intergovernmental Panel on Climate Change. Cambridge University Press, Cambridge, United Kingdom/New York, NY, USA.

IPCC, 2012.Climate Change 2022 Impacts, Adaptation, and Vulnerability. Contribution of Working Group II to the Sixth Assessment Report of the Intergovernmental Panel on Climate Change [H.-O. Pörtner, D.C. Roberts, M. Tignor, E.S. Poloczanska, K. Mintenbeck, A. Alegría, M. Craig, S. Langsdorf, S. Löschke, V. Möller, A. Okem, B. Rama (eds.)]. Cambridge University Press. Cambridge University Press, Cambridge, UK and New York, NY, USA, 3056 pp., doi:10.1017/9781009325844.

Italiano, F., Kis, B.M., Baciu, C., Ionescu, A., Harangi, S., Palcsu, L., 2017. Geochemistry of dissolved gases from the Eastern Carpathians - Transylvanian Basin boundary. Chem. Geol. 469, 117–128. https://doi.org/10.1016/j.chemgeo.2016.12.019

Jakab, Gy. 1998. Geológia masivului alcalin de la Ditrâu. - Miercurea Ciuc, 7-284.

Javoy, M., Pineau, F. and Allègre, C.J., 1982. Carbon geodynamic cycle. Nature, 300 (5888), pp.171-173.

John, C.M., Bowen, D., 2016. Community software for challenging isotope analysis: First applications of 'Easotope' to clumped isotopes. Rapid Commun. Mass Spectrom. 30, 2285–2300. https://doi.org/10.1002/rcm.7720

Johnson, G., Mayer, B., 2011. Oxygen isotope exchange between H2O and CO2 at elevated CO2 pressures: Implications for monitoring of geological CO_2 storage. Appl. Geochemistry 26, 1184–1191. https://doi.org/10.1016/j.apgeochem.2011.04.007

Jugovics, L., 1970. A Kisalföld bazalt és bazalttufa előfordulásai. MÁFI Évi Jel. 1970. évről.

Juhász Gy. 1994; Magyarországi neogén medencerészek pannóniai s. l. üledéksorának összehasonlító elemzése. Földtani Közlöny 124/4, 341–365. 57

Juhász Gy. 1998; A magyarországi neogén mélymedencék pannóniai képződményeinek litosztratigráfiája. In: Bérczi István – Jámbor Áron (szerk.): Magyarország geológiai képződményeinek rétegtana. Magyar Olajipari Részvénytársaság−Magyar Állami Földtani Intézet, Budapest, 469–484.

Juhász, G., 1992. A pannóniai (s.l.) formációk térképezése az Alföldön: elterjedés, fácies és üledékes környezet Pannonian (s.l.) lithostratigraphic units in the Great Hungarian Plain: distribution, fades and sedimentary environment. Földtani Közlöny 122, 133–165.

Karim, A., Pe-Piper, G. and Piper, D.J., 2010. Controls on diagenesis of Lower Cretaceous reservoir sandstones in the western Sable Subbasin, offshore Nova Scotia. Sedimentary Geology, 224(1-4), pp.65-83. https://doi.org/10.1016/j.sedgeo.2009.12.010

Kharaka, Y.K., Hanor, J.S., 2013. Deep Fluids in Sedimentary Basins, 7th ed, Treatise on Geochemistry: Second Edition. Elsevier Ltd. https://doi.org/10.1016/B978-0-08-095975-7.00516-7

Kim, S.T., Mucci, A., Taylor, B.E., 2007. Phosphoric acid fractionation factors for calcite and aragonite between 25 and 75 °C: Revisited. Chem. Geol. 246, 135–146. https://doi.org/10.1016/j.chemgeo.2007.08.005

Király, C., 2017. Mihályi-Répcelak természetes CO_2-előfordulás környezetgeokémiai vizsgálata. in Hungarian, Ph.D thesis, Department of Petrology and Geochemisrty, Eötvös Loránd Tudományegyetem, Budapest.

Király, C., Sendula, E., Szamosfalvi, Á., Káldos, R., Kónya, P., Kovács, I.J., Füri, J., Bendő, Z., Falus, G., 2016a. The relevance of dawsonite precipitation in CO_2 sequestration in the Mihályi-Répcelak area, NW Hungary. Geol. Soc. London, Spec. Publ. 435, 405–418. https://doi.org/10.1144/sp435.15

Király, C., Szabó, Z., Szamosfalvi, Á., Kónya, P., Szabó, C., Falus, G., 2017. How much CO2 is trapped in carbonate minerals of a natural CO_2 occurrence? Energy Procedia 125, 527–534. https://doi.org/10.1016/j.egypro.2017.08.180

Király, C., Szamosfalvi, Á., Zilahi-Sebess, L., Kónya, P., Kovács, I.J., Sendula, E., Szabó, C., Falus, G., 2016b. Caprock analysis from the Mihályi-Répcelak natural CO2 occurrence, Western Hungary. Environ. Earth Sci. 75, 2–11. https://doi.org/10.1007/s12665-016-5399-6

Kis, B.M., Baciu, C., Zsigmond, A.R., Kékedy-Nagy, L., Kármán, K., Palcsu, L., Máthé, I., Harangi, S., 2020. Constraints on the hydrogeochemistry and origin of the CO_2-rich mineral waters from the Eastern Carpathians – Transylvanian Basin boundary (Romania). J. Hydrol. 591. https://doi.org/10.1016/j.jhydrol.2020.125311

Kis, B.M., Caracausi, A., Palcsu, L., Baciu, C., Ionescu, A., Futó, I., Sciarra, A., Harangi, S., 2019. Noble Gas and Carbon Isotope Systematics at the Seemingly Inactive Ciomadul Volcano (Eastern-Central Europe, Romania): Evidence for Volcanic Degassing. Geochemistry, Geophys. Geosystems 20, 3019–3043. https://doi.org/10.1029/2018GC008153

Koch, A., 1885. Erdély ásványainak kritikai átnézete.

Koenen, M., ter Heege, J., Peeters, R. 2014. Transport properties of intact caprocks and effects of CO2-water-rock interaction: CO_2-induced mineral reactions in sandstone reservoirs (CATO2-WP3.03-D12). CATO-2 project public report.

Koncz, I., 1983. The stable carbon isotope composition of the hydrocarbon and carbon dioxide components of Hungarian natural gases. Acta Mineralogica-Petrographica, Szeged XXVIjl, 33-49. 1983 2, 33-49.

Koncz, I., Etler, O., 1994. Origin of oil and gas occurrences in the Pliocene sediment of the Pannonian basin, Hungary. Org. Geochem. 21, 1069–1080.

Kőrössy, L., 1987. A Kisalföld kőolaj- és földgázkutatás földtani eredményei. Általános Földtani Szle. 22, 99–174.

Kovaĉ, M., Andreyeva-Grigorovich, A., Bajraktarevic, Z., Brzobohaty, R., Filipescu, S., Fodor L., Harzhauser, M., Nagymarosy A., Oszczypko, N., Pavelic, D., Rögl, F., Saftic, B., Slive, L., Studencka, B. 2007; Badenian evolution of the Central Paratethys Sea: paleogeography, climate and eustatic sea-level changes. Geologica Carpathica 58, 6, 579-606.

Kovács, I., Németh, T., Kiss, G.B., Benkó, Z., 2021. Application of the capillary method in micro xray diffractometry (m-xrd): A useful technique for the characterization of small amounts of clay minerals. Cent. Eur. Geol. 64, 1–6. https://doi.org/10.1556/24.2020.00005

Kristály, F., Szakáll, S., Bonazzi, P., Bindi, L., Papucs, A., 2006. Neogene volcanism related arsenic sulphide paragenesis from Lazaresti and Bodoc (Ciomadu area, Harghite Mts.), and Covasna. Rom. J. Mineral. 82, 192–195.

Kristmannsdottir, H., 1979. Alteration of basaltic rocks by hydrothermal-activity at 100-300°C. Dev. Sedimentol. 27, 359–367. https://doi.org/10.1016/S0070-4571(08)70732-5

Laczkó, A., Szakáll, S., Botár, M., Zólya, L., 2007. Tanulmányok Erdély földtanából A Kelemen-Görgényi-Hargita neogén-kvarter vulkáni ívhez kötődő ásványelőfordulások (Keleti-Kárpátok , Románia). Földtani Közlöny 137, 261–285.

Landis, G.P., 1983. Harding Iceland Spar: a new $\delta^{18}O$-$\delta^{13}C$ carbonate standard for hydrothermal minerals. Isotope Geoscience 1, 91-94, https://doi.org/10.1016/S0009-2541(83)80008-4

Lange, T.P., Palcsu, L., Szakács, A., Kővágó, Á., Gelencsér, O., Gál, Á., Gyila, Szabó, Cs., Kovács, I.J., 2022. Origin and evolution of the emanating gases in Covasna, Transylvania. 17th Carpathian Basin Conference for Environmental Science, 58-59.

Lenkey, L., Dövényi, P., Horváth, F., Cloetingh, S., 2002. Geothermics of the Pannonian Basin and its bearing on the neotectonics. EGU Stephan Mueller Special Publications Series, 3, 29–40.

Li, F., Li, W., 2017. Petrological record of CO_2 influx in the Dongying Sag, Bohai Bay Basin, NE China. Appl. Geochemistry 84, 373–386. https://doi.org/10.1016/j.apgeochem.2017.07.015

Liu, N., Liu, L., Qu, X., Yang, H., Wang, L., Zhao, S., 2011. Genesis of authigene carbonate minerals in the Upper Cretaceous reservoir, Honggang Anticline, Songliao Basin: A natural analog for mineral trapping of natural CO_2 storage. Sediment. Geol. 237, 166–178. https://doi.org/10.1016/j.sedgeo.2011.02.012

Liu, X., Deng, W., Wei, G., 2019. Carbon and oxygen isotopic analyses of calcite in calcite–dolomite mixtures: Optimization of selective acid extraction. Rapid Commun. Mass Spectrom. 33, 411–418. https://doi.org/10.1002/rcm.8365

Łodziana, Z., Stoica, G., Pérez-Ramírez, J., 2011. Reevaluation of the structure and fundamental physical properties of dawsonites by DFT studies. Inorg. Chem. 50, 2590–2598, https://doi.org/10.1021/ic102443h.

Loughnan, F.C., See, G.T., 1967. Dawsonite in the Greta Coal Measures at Muswellbrook, New South Wales. Am. Mineral. 52, 1216–1219.

Lu, P., Zhang, G., Huang, Y., Apps, J., Zhu, C., 2022. Dawsonite as a Temporary but Effective Sink for Geological Carbon Storage. Int. J. Greenh. Gas Control 119, 103733. https://doi.org/10.1016/j.ijggc.2022.103733

Magyar I., Geary H., D., Müller P. 1999; Paleogeograpic evolution of the Late Miocene Lake Pannon in Central Europe, Palaeogeography, Palaeoclimatology, Palaeoecology, 147, 151–167.
Magyar, I., Radivojević, D., Sztanó, O., Synak, R., Ujszászi, K., Pócsik, M., 2013. Progradation of the paleo-Danube shelf margin across the Pannonian Basin during the Late Miocene and Early Pliocene. Glob. Planet. Change 103, 168–173. https://doi.org/10.1016/j.gloplacha.2012.06.007
Mamyrin, B.A., Anufrijev, G.S., Kamenskii, I.L. and Tolstikhin, I.N. 1970. Determination of the isotopic composition of atmospheric helium. Geochem. Int. 7, 498-505.
Matenco, L., Bertotti, G., Leever, K., Cloetingh, S., Schmid, S.M., Tărăpoancă, M., Dinu, C., 2007. Large-scale deformation in a locked collisional boundary: Interplay between subsidence and uplift, intraplate stress, and inherited lithospheric structure in the late stage of the SE Carpathians evolution. Tectonics 26. https://doi.org/10.1029/2006TC001951
Matter, J.M., Stute, M., Snæbjörnsdóttir, S.Ó., Oelkers, E.H., Gislason, S.R., Aradottir, E.S., Sigfusson, B., Gunnarsson, I., Sigurdardottir, H., Gunnlaugsson, E., Axelsson, G., Alfredsson, H.A., Wolff-Boenisch, D., Mesfin, K., Fernandez de la Reguera Taya, D., Hall, J., Dideriksen, K. and Broecker, W.S. 2016. Rapid carbon mineralization for permanent disposal of anthropogenic carbon dioxide emissions. Science 352.
Mátyás, J., Matter, A., 1997. Diagenetic indicators of meteoric flow in the Pannonian Basin, southeast Hungary 281–296.
McBride, E.F., 1963. A classification of common sandstones. J. Sediment. Petrol. 33, 664–669.
McCrea, J.M., 1950. On the isotopic chemistry of carbonates and a paleotemperature scale. J. Chem. Phys. 18, 849–857. https://doi.org/10.1063/1.1747785
Méheut, M., Lazzeri, M., Balan, E., Mauri, F., 2010. First-principles calculation of H/D isotopic fractionation between hydrous minerals and water. Geochim. Cosmochim. Acta 74, 3874–3882. https://doi.org/10.1016/j.gca.2010.04.020
Meijer, H.A.J., Li, W.J., 1998. Isotopes in environmental and health studies the use of electrolysis for accurate $\delta^{18}O$ and $\delta^{17}O$ isotope measurements in water. Isotopes Environ. Health Stud. 34, 349–369.
Melinte-Dobrinescu M.C., Roban R.D. 2011. Cretaceous anoxic–oxic changes in the Moldavids (Carpathians, Romania). Sediment. Geol. 235:79–90.
Mészáros, L., Dallos, E., Vágó, L., Czupik, J., Paulik, D., Darabos, A., Marton, T., Simán, G., Ferenczy, Z., 1979. A Mihályi kutatási terület lehatároló fázisú zárójelentése, a szén-dioxid- és a „nem éghető" kevert gáztelepek vagyonszámítása.
Ming, X.R., Liu, L., Yu, L., Bai, H.G., Yu, Z.C., Liu, N., Yang, H.X., Wang, F.G., Li, B.X., 2017. Thin-film dawsonite in Jurassic coal measure strata of the Yaojie coalfield, Minhe Basin, China: A natural analogue for mineral carbon storage in wet supercritical CO_2. Int. J. Coal Geol. 180, 83–99. https://doi.org/10.1016/j.coal.2017.07.007
Morera-Chavarría, A., Griffioen, J., Behrends, T., 2016. Optimized sequential extraction for carbonates: Quantification and δ13C analysis of calcite, dolomite and siderite. Chem. Geol. 443, 146–157. https://doi.org/10.1016/j.chemgeo.2016.09.025
Nádor, A., 2002. Natural Analogues to the storage of CO_2 in the geological environment.
Nagymarosy A., Hámor G., 2012. Genesis and evolution of Pannonian Basin. In: Haas J., (ed.), Geology of Hungary, Regional Geology Review, Springer, 149-200. https://doi.org/10.1007/978-3-642-21910-8_3
Nagymarosy A., Müller P., 1988. Some Aspects of Neogene Biostratigraphy in the Pannonian Basin. In: Royden, L.H. & Horváth, F. (Eds.): The Pannonian Basin. AAPG Memoir, 45, 69–78.
Néda, T., Szakács, A., Cosma, C., Mócsy, I., 2008. Radon concentration measurements in mofettes from Harghita and Covasna Counties, Romania. J. Environ. Radioact. 99, 1819–1824. https://doi.org/10.1016/j.jenvrad.2008.07.007
O'Neil, J.R., Clayton, R.N., Mayeda, T.K., 1969. Oxygen isotope fractionation in divalent metal carbonates. J. Chem. Phys. 51, 5547–5558. https://doi.org/10.1063/1.1671982
Oelkers, E.H., Cole, D.R., 2008. Carbon dioxide sequestration: A solution to a global problem. Elements 4, 305–310. https://doi.org/10.2113/gselements.4.5.305
Ohmoto, H., Rye, R.O., 1979. Isotopes of sulfur and carbon. Geochemistry hydrothermal ore Depos. 509–567.
Palandri, J.L., Kharaka, Y.K., 2004. A compilation of rate parameters of water-mineral interaction kinetics for application to geochemical modeling. USGS Open File Rep. 2004–1068, 71.
Palcsu, L., Vető, I., Futó, I., Volida, G., Papp, L., Major, Z., 2014. In-reservoir mixing of mantle-derived CO_2 and metasedimentary CH_4-N_2 fluids - Noble gas and stable isotope study of two multistacked fields (Pannonian Basin System, W-Hungary). Mar. Pet. Geol. 54, 216–227. https://doi.org/10.1016/j.marpetgeo.2014.03.013
Pálfy M. 1905. A kovásznai Pokolsár-fürdő, Term. tud. közl., XXXVII., 274–279, Budapest.

Palkó M., Deák, J. 1974. Az ölbői szén-dioxid előfordulás – Előzetes fázisú kutatási zárójelentés. Országos Földtani és Geofizikai Adattár, Budapest, T.18579

Papucs A. 2004. A kovásznai Hankó-völgy ásványtársulásai. Imre József Emlékkonferencia, Kolozsvár, 19.

Papucs, A., 2000. Arsenic containing minerals in the Hankó Valley (Covasna, Romania). Historical background. Dawsonite: a new mineral for Romania, in: Acta Mineralogica-Petrographica. Szeged, p. 86.

Papucs, A., 2016. Kovásznai arzénásványok és dawsonit. XVIII. Székelyföldi Geológus Találkozó, Kovászna.

Parfenoff, A., Pomerol, C. and Tourenq, J. (1970) Les minéraux en grains: Méthodes d'études et détermination. Masson et Cie, Paris, 578 p.

Parkhurst, D.L., Apelllo, C.A.J. 2013. Description input and examples for PHREEQC version 3 – A computer program for speciation, batch-reaction, one-dimensional transport, and inverse geochemical calculations: U.S. Geological Survey Techniques and Methods, book 6, chap. A43, 497.

Pearce, J., Holloway, S., Wacker, H., Nelis, M., Rochelle, C., Bateman, K., 1996. Natural occurrences as analogues for the geological disposal of carbon dioxide. Energy Convers. Manag. 37, 1123–1128.

Pham, V.T.H, Lu, P., Aagaard, P., Zhu, C., Hellevang, H. 2011. On the potential of CO_2-water-rock interactions for CO_2 storage using a modified kinetic model. Int. J. Greenh. Gas Control 5, 1002-1015. https://doi.org/10.1016/j.ijggc.2010.12.002

Pierre, C., Rouchy, J.M., 1990. Sedimentary and diagenetic evolution of Messinian evaporites in the Tyrrhenian Sea (ODP Leg 107, sites 652, 653, and 654): petrographic, mineralogical, and stable isotope records. Proc., Sci. results, ODP, Leg 107, Tyrrhenian Sea 107, 187–210. https://doi.org/10.2973/odp.proc.sr.107.131.1990

Piper, A.M., 1944. A graphic procedure in the geochemical interpretation of water-analyses. Transactions. Am. Geophys. union 25, 914–928.

Pogácsás Gy. 1984; Seismic stratigraphic features of the Neogene Sediments in the Pannonian Basin. Geophysical Transactions, 30, 373–410.

Pogge von Strandmann, P.A.E., Burton, K.W., Snaebjornsdottir, S.O., Sigfusson, B., Aradottir, E.S., Gunnarsson, I., Alfredsson, H.A., Mesfin, K.G., Oelkers, E.H. and Gislason, S.R. 2019. Rapid CO_2 mineralisation into calcite at the CarbFix storage site quantified using calcium isotopes. Nat Commun 10, 1983, 10.1038/s41467-019-10003-8.

Qu, X., Zhang, Y., Li, Q., Du, T., Li, Y., 2022. Geological features and occurrence conditions of dawsonite as a main Carbon-Fixing mineral: Geological features and occurrence conditions. Alexandria Eng. J. 61, 2997–3011. https://doi.org/10.1016/j.aej.2021.08.022

Ray, J.S., Ramesh, R., 1998. Stable carbon and oxygen isotope analysis of natural calcite and dolomite mixtures using selective acid extraction. J. Geol. Soc. India 52, 323–332.

Rice, D.D., 1993. Composition and origins of coalbed gas, in: In: Law, B.E., Rice, D.D. (Eds.), Hydrocarbons from Coal: AAPG Studies in Geology, Vol. 38. pp. 159–184.

Rollinson, H., 1993. Using Geochemical Data. Longman, London, UK, 352 pp.

Rosenbaum, J., Sheppard, S.M.F., 1986. An isotopic study of siderites dolomites and ankerites at high temperatures 50, 1147–1150.

Rumsey, M.S., Welch, M.D., Spratt, J., Kleppe, A.K., 2020. Grguricite, $CaCr_2(CO_3)_2(OH)_4 \cdot 4H_2O$, a new alumohydrocalcite analogue . Mineral. Mag. 84, 778–784. https://doi.org/10.1180/mgm.2020.66

Sacchi, M., Horváth, F., 2002. Towards a new time scale for the Upper Miocene continental series of the Pannonian basin (Central Paratethys). EGU Stephan Mueller Special Publication Series, 3, pp.79-94.

Seghedi, I., Maţenco, L., Downes, H., Mason, P.R.D., Szakács, A., Pécskay, Z., 2011. Tectonic significance of changes in post-subduction Pliocene-Quaternary magmatism in the south east part of the Carpathian-Pannonian Region. Tectonophysics 502, 146–157. https://doi.org/10.1016/j.tecto.2009.12.003

Selmeczi, I. (2018) Magyarország szénhidrogén-kutatási területei — Észak-Dunántúl–Kisalföld részmedence. In: Szénhidrogének Magyarországon, Szerkesztette: Kovács Zsolt, Budapest, Magyar Energetikai és Közmű- szabályozási Hivatal. ISBN: 978-615-00-1393-0

Sendula, E. 2015. Ipari CO_2 tárolásra alkalmas hazai üledékes kőzetek petrográfiai vizsgálata és a rendszerben várható geokémiai változások modellezése. MSc dolgozat, Eötvös Loránd Tudományegyetem, Budapest, pp.111.

Serna, C.J., García-Ramos, J. V., Peña, M.J., 1985. Vibrational study of dawsonite type compounds $MAl(OH)_2CO_3$ (M = Na, K, NH_4). Spectrochim. Acta Part A Mol. Spectrosc. 41, 697–702. https://doi.org/10.1016/0584-8539(85)80177-X

Sharp, Z., 2017. Principles of Stable Isotope Geochemistry, 2nd ed.

Sheppard, S.M.F., 1986. Characterization and isotope variations in natural waters. Rev. Miner. 16, 165–183.

Smith, J.W., Milton, C., 1966. Dawsonite in the green river formation of Colorado. Econ. Geol. 61, 1029–1042. https://doi.org/10.2113/gsecongeo.61.6.1029

Snæbjörnsdóttir, S.Ó., Sigfússon, B., Marieni, C., Goldberg, D., Gislason, S.R. and Oelkers, E.H. 2020. Carbon dioxide storage through mineral carbonation. Nat. Rev. Earth & Environment 1, 90-102, 10.1038/s43017-019-0011-8.

Spötl, C., Vennemann, T.W., 2003. Continuous-flow isotope ratio mass spectrometric analysis of carbonate minerals. Rapid Commun. Mass Spectrom. 17, 1004–1006. https://doi.org/10.1002/rcm.1010

Srebrodol'skiy, B.I., 1976. Alumohydrocalcites. Int. Geol. Rev. 18, 321–328.

Stevens, S.H., Tye, B.S., 2007. NACS-Natural CO_2 Analogs for Carbon Sequestration. https://doi.org/10.2172/902517

Stroescu, C. 1982. Farmacodinamica apelor minerale de cura interna din Romania (Editura Academiei Republicii Socialiste Romania, Bucuresti pp. 64.

Swart, P.K., Melim, L.A., 2000. The origin of dolomites in tertiary sediments from the margin of Great Bahama Bank. J. Sediment. Res. 70, 738–748. https://doi.org/10.1306/2DC40934-0E47-11D7-8643000102C1865D

Szabó, Z., Gál, N.E., Kun, É., Szőcs, T., Falus, G., 2018. Accessing effects and signals of leakage from a CO_2 reservoir to a shallow freshwater aquifer by reactive transport modelling. Environ. Earth Sci. 77, 1–12. https://doi.org/10.1007/s12665-018-7637-6

Szabó, Z., Hellevang, H., Király, C., Sendula, E., Kónya, P., Falus, G., Török, S., Szabó, C., 2016. Experimental-modelling geochemical study of potential CCS caprocks in brine and CO_2-saturated brine. Int. J. Greenh. Gas Control 44, 262–275. https://doi.org/10.1016/j.ijggc.2015.11.027

Szakács, A., 2010. Post-volcanic Phenomena in the East Carpathians. Nat. Herit. from East to West Case Stud. from 6 EU Ctries. 1–384. https://doi.org/10.1007/978-3-642-01577-9

Szamosfalvi, Á., 2014. Mihályi-Répcelak természetes szén-dioxid tároló mélyfúrás-geofizikai adatainak újraértelmezése a szén-dioxid föld alatti tárolás feltételrendszerének kiemelt figyelembevételével. Doktori értekezés, Miskolci Egyete, pp. 202, DOI: 10.14750/ME

Tari G., Horváth F., 2010; A Dunántúli-középhegység helyzete és eoalpi fejlődéstörténete a Keleti-Alpok takarós rendszerében: egy másfél évtizedes tektonikai modell időszerűsége. Földtani Közlöny 140, 483-510.

Tari, G., 1994. Apline tectonics of the Pannonian Basin. Rice University, Houston, Texas.

Taylor, H.P.J., 1974. The Application of Oxygen and Hydrogen Isotope Studies to Problems of Hydrothermal Alteration and Ore Deposition. Econ. Geol. 69, 843–883.

Tesfay, T., 2006. Modeling Groundwater Denitrification by Ferrous Iron Using PHREEQC. Theses Diss.

Tóth, G., Rman, N., Rotár-Szalkai, Á., Kerékgyártó, T., Szőcs, T., Lapanje, A., Černák, R., Remsík, A., Schubert, G., Nádor, A., 2016. Transboundary fresh and thermal groundwater flows in the west part of the Pannonian Basin. Renew. Sustain. Energy Rev. 57, 439–454. https://doi.org/10.1016/j.rser.2015.12.021

Tóth, J., Udvardi, B., Kovács, I.J., Falus, G., Szabó, C., Troskot-Čorbić, T., Slavković, R., 2012. Analytical development in FTIR analysis of clay minerals. MOL Sci. Mag. 1, 52–61.

Túri, M., Palcsu, L., Papp, L., Horváth, A., Futó, I., Molnár, J., Rinyu, L., Janovics, R., Braun, M., Hubay, K., Kis, B., Koltay, G., 2016. Isotope Characteristics of the water and sediment in volcanic lake Saint Ana, East-Carpathians, Romania. Carpathian J. Earth Environ. Sci. 11, 475–484.

Udvardi, B., Kovács, I.J., Kónya, P., Földvári, M., Füri, J., Budai, F., Falus, G., Fancsik, T., Szabó, C., Szalai, Z., Mihály, J., 2014. Application of attenuated total reflectance Fourier transform infrared spectroscopy in the mineralogical study of a landslide area, Hungary. Sediment. Geol. 313, 1–14. https://doi.org/10.1016/j.sedgeo.2014.08.005

Uysal, I.T., Golding, S.D., Bolhar, R., Zhao, J. xin, Feng, Y. xing, Baublys, K.A., Greig, A., 2011. CO2 degassing and trapping during hydrothermal cycles related to Gondwana rifting in eastern Australia. Geochim. Cosmochim. Acta 75, 5444–5466. https://doi.org/10.1016/j.gca.2011.07.018

Vaculíková, L., Plevová, E., 2005. Identification of clay minerals and micas in sedimentary rocks. Acta Geodyn. Geomater 2, 167–175.

Vakarcs G., Vail, P., Tari G., Pogácsás Gy., Mattick, R., Szabó A. 1994; Third-order Middle Miocene-Pliocene depositional sequences in the prograding delta complex of the Pannonian Basin. Tectonophysics, 240, 81–106.s.

Van der Marel, H.W. Beutelspacher H. 1976. Atlas of Infrared Spectroscopy of Clay Minerals and their Admixtures. Amsterdam-Oxford-New York: Elsevier Scientific Publishing Company, 396 p.

Vaselli, O., Minissale, A., Tassi, F., Magro, G., Seghedi, I., Ioane, D., Szakacs, A., 2002. A geochemical traverse across the Eastern Carpathians (Romania): Constraints on the origin and evolution of the mineral water and gas discharges. Chem. Geol. 182, 637–654. https://doi.org/10.1016/S0009-2541(01)00348-5

Vető, I., Csizmeg, J., Sajgó, C., 2014. Mantle-related CO_2 , metasedimentary HC-N2 gas and oil traces in the Répcelak and Mihályi accumulations, W-Hungary — mixing of three fluids of very different origin.

Cent. Eur. Geol. 57, 53–69. https://doi.org/10.1556/ceugeol.57.2014.1.3
Vitali, F., Longstaffe, F.J., Bird, M.I., Gage, K.L., Caldwell, W.G.E., 2001. Hydrogen-isotope fractionation in aluminum hydroxides: Synthesis products versus natural samples from bauxites. Geochim. Cosmochim. Acta 65, 1391–1398. https://doi.org/10.1016/S0016-7037(00)00604-9
Voigt, M., Marieni, C., Clark, D.E., Gíslason, S.R., Oelkers, E.H., 2018. Evaluation and refinement of thermodynamic databases for mineral carbonation. Energy Procedia 146, 81–91. https://doi.org/10.1016/j.egypro.2018.07.012
Walters, L.J., Claypool, G.E., Choquette, P.W., 1972. Reaction rates and $\delta^{18}O$ variation for the carbonate-phosphoric acid preparation method. Geochim. Cosmochim. Acta 36, 129–140. https://doi.org/10.1016/0016-7037(72)90002-6
Wanek, F., 2000. Ásványvízkutatás és szénhidrogének a Keleti-Kárpátokban 1908 előtt*. Kőolaj és Földgáz 33. 133, 74–80.
Wanek, F., 2006. Arsenic mineral occurrences of Hankó-patak. 8th Mining, Metallurgy and Geology Conference, Hungarian Technical Scientific Society of Transylvania, Sepsiszentgyörgy.
Weinlich, F.H., Bräuer, K., Kämpf, H., Strauch, G., Tesař, J., Weise, S.M., 1999. An active subcontinental mantle volatile system in the western Eger rift, Central Europe: Gas flux, isotopic (He, C, and N) and compositional fingerprints. Geochim. Cosmochim. Acta 63, 3653–3671. https://doi.org/10.1016/S0016-7037(99)00187-8
Wijbrans, J., K. Nemeth, U. Martin, K. Balogh 2007. $^{40}Ar/^{39}Ar$ geochronology of Neogene phreatomagmatic volcanism in the western Pannonian Basin, Hungary. J. Volcanol. Geoth. Res. 164, 193–204. https://doi.org/10.1016/j.jvolgeores.2007.05.009
Wopfner, H., Höcker, C.F.W., 1987. The Permian Groeden Sandstone between Bozen and Meran (northern Italy), a habitat of Dawsonite and Nordstrandite. Neues Jahrb. für Geol. und Paläontologie - Monatshefte 1987, 161–176. https://doi.org/10.1127/njgpm/1987/1987/161
Worden, R.H., 2006. Dawsonite cement in the Triassic Lam Formation, Shabwa Basin, Yemen: A natural analogue for a potential mineral product of subsurface CO_2 storage for greenhouse gas reduction. Mar. Pet. Geol. 23, 61–77. https://doi.org/10.1016/j.marpetgeo.2005.07.001
Xu, T., Apps, J.A., Pruess, K., 2003. Reactive geochemical transport simulation to study mineral trapping for CO_2 disposal in deep arenaceous formations. J. Geophys. Res. Solid Earth 108, 2071. https://doi.org/10.1029/2002jb001979
Xu, T., Apps, J.A., Pruess, K., 2005. Mineral sequestration of carbon dioxide in a sandstone-shale system. Chem. Geol. 217, 295–318. https://doi.org/10.1016/j.chemgeo.2004.12.015
Yu, M., Liu, L., Yu, Z., Liu, N., Yang, H., Qu, X., 2014. Dawsonite fixation of mantle CO_2 in the cretaceous Songliao Basin, Northeast China: A natural analogue for CO_2 mineral trapping in oilfields. Int. Geol. Rev. 56, 1792–1812. https://doi.org/10.1080/00206814.2014.958765
Yui, T.F., Gong, S.Y., 2003. Stoichiometry effect on stable isotope analysis of dolomite. Chem. Geol. 201, 359–368. https://doi.org/10.1016/j.chemgeo.2003.08.007
Zalba, P.E., Conconi, M.S., Morosi, M., Manassero, M., Comerio, M., 2011. Dawsonite in tuffs and litharenites of the Cerro Castaño Member, Cerro Barcino Formation, Chubut Group (Cenomanian), Los Altares, Patagonia, Argentina. Can. Mineral. 49, 503–520. https://doi.org/10.3749/canmin.49.2.503
Zhao, S., Liu, L., Liu, N., 2018. Petrographic and stable isotopic evidences of CO2-induced alterations in sandstones in the Lishui sag, East China Sea Basin, China. Appl. Geochemistry 90, 115–128. https://doi.org/10.1016/j.apgeochem.2018.01.004
Zhou, B., Liu, L., Zhao, S., Ming, X.R., Oelkers, E.H., Yu, Z.C., Zhu, D.F., 2014. Dawsonite formation in the Beier Sag, Hailar Basin, NE China tuff: A natural analog for mineral carbon storage. Appl. Geochemistry 48, 155–167. https://doi.org/10.1016/j.apgeochem.2014.07.015
Zilahi-Sebess, L., 2013. Országos geotermikus potenciál-felmérés. Országos Kőolajipari Tröszt.
Zuber, A., Chowaniec, J., 2009. Diagenetic and other highly mineralized waters in the Polish Carpathians. Appl. Geochemistry 24, 1889–1900. https://doi.org/10.1016/j.apgeochem.2009.07.002

12. Supplementary

Table S1. Selection of the dawsonite-bearing sandstones worldwide showing stable isotope composition of dawsonite, formation temperature and the origin of the CO_2.

Area	Sample	Depth [m]	$\delta^{13}C$ [‰, PDB]	$\delta^{18}O$ [‰, SMOW]	Temperature [°C]	Origin of CO_2	References
Bowen-Gunnadah-Sydney Basin, Australia	dawsonite-bearing sandstone	160-1424	-4.0 – +4.0	+9.8 – +19.8	25-75	magmatic	Baker et al. 1995
Koman area, Albania	dawsonite and realgar-orpiment deposit	-	+5.6 – +6.2	+42.5 – +43.9	<75-85	hydrothermal	Ferrini et al. 2003
Dartbrook, Sydney Basin, Australia	cleat dawsonite	-	-1.7 – +2.4	+13.6 – +19.8	-	magmatic	Golab et al. 2006
Hailaer Basin, China	dawsonite bearing sandstone	1284-1774	-5.3 – -1.5	+5.2 – +10.8	-	magmatic	Gao et al. 2009
Honggang, Songliao Basin, China	dawsonite bearing sandstone	1256-1556	-3.4 – +3.3	+10.7 – +18.0	110-130	inorganic and magmatic	Liu et al. 2011
Gondwana rift, Australia	dawsonite bearing sandstone	-	+0.2 – +2.3	+9.9 – +16.5	-	magmatic and marine	Uysal et al. 2011
Beier Sag, Hailaer Basin, China	dawsonite-bearing tuffaceous sandstone	882-941	-4.1 – - 2.2	+10.7 – +14.1	71-74	magmatic	Zhou et al. 2014
Golfo San Jorge Basin, Patagonia, Argentina	dawsonite-bearing volcaniclastic rocks	-	-0.1 – +1.5	+15.7 – +20.9	70-80	magmatic	Comerio et al. 2014
Dongying Sag, Bohai-Bay Basin, China	dawsonite-bearing sandstone	1469-1615	-2.2 – +3.5	+17.2 – +19.8	79-85	magmatic	Li & Li, 2017
Minhe Basin, China	cleat-filling dawsonite in coal, sandstone fracture-filling dawsonite	600-1000	-0.1 – +7	+26.2 – +28.8	31-44	magmatic and decomposition of basement marble	Ming et al. 2017
Lishui Sag, East China Sea Basin, China	dawsonite-bearing sandstone	2235-2295	-7.9 – -0.9	+19.1 – +21.2	110-123	magmatic	Zhao et al. 2018

12.1. Clumped isotope measurement of calcite (KOV-10/1 Cc)

The phosphoric acid digestion of the sample was performed at 70 °C with a Thermo Scientific Kiel IV automatic carbonate device, which is coupled by inert silica coated capillary to the IRMS. To eliminate the organic contamination from the extracted carbon-dioxide gas, an additional Thermo Scientific PoraPak trap was installed between the two cold fingers of the Kiel device. The operation temperature of this trap was -30 °C. After the cryogenic purification the carbon-dioxide gas was measured against a working CO_2 gas (Linde AG, $\delta^{13}C_{VPDB}$ = -3.9 ‰, $\delta^{18}O_{VPDB}$ = -12.5 ‰, purity = 99.998 %) for m/z 44-49 in micro-volume inlet mode and with long integration dual inlet (LIDI) method (Hu et al., 2014). Sample measurement consisted of 14 replicate analyses of 100 µg aliquots that were measured alongside with ETH1, ETH2 and ETH3 normalization standards and IAEA-C2 monitoring sample with assigned values (Bernasconi et al., 2018, 2021). The 253 Plus IRMS has 7 Faraday cups with resistors $3x10^8\Omega$, $3x10^{10}\Omega$ and $1x10^{11}\Omega$ for masses 44, 45 and 46 and $1x10^{13}\Omega$ for masses 47, 47.5, 48 and 49. The signal collection of one replicate consists of 50 cycles with 10 seconds integration period. Secondary electrons caused negative background effect was corrected by application of the pressure-sensitive baseline correction (Bernasconi et al., 2013) on all the raw beam signals. Data evaluation was carried out with Easotope application (John and Bowen, 2016) using CO_2 clumped ETH PBL replicate analyses method and "IUPAC" parameters (Baertschi, 1976, Gonfiantini et al., 1995, Meijer and Li, 1998, Assonov and Brenninkmeijer, 2003, Brand et al., 2010). Results of Δ_{47} are given in the I-CDES90 scale (Bernasconi et al., 2021), and apparent temperatures in °C were calculated based on the Δ_{47}-temperature calibration from Anderson et al. (2021) with temperature uncertainties given as 1σ standard error (SE).

12.2. Analyses of water samples

12.2.1. pH

The pH meter was calibrated with WTW buffers pH-4 and pH-7, then it was checked with buffer pH-10. After calibration, the electrode was put into the vessel to measure conductivity and measure the pH.

12.2.2. Conductivity

The calibration of the conductivity meter was checked by 0.01 mol/l KCl solution. Then, 50 ml beaker was filled with the sample, then the conductivity was measured.

12.2.3. Ammonium

Filtrations on 0.45 µm pore size filter into a PE vessel were used, followed acidic preservation (0.2 ml 1:1 H_2SO_4 to 100 ml filtered sample). The components without preservation were measured as soon as possible, but not later than 24 hours after sample reception.

4.00 ml sample was neutralized with 90 µl 2 mol/l NaOH solution, then 400 µl colouring reagent (containing sodium salicylate, trisodium citrate and sodium pentacyanido(nitroso)ferrate(II)) and 400 µl oxidizing reagent (containing sodium dichloroisocyanurate) was added. The absorbance belonging the evolving blue colour was measured by spectrophotometer at 655 nm. On every measuring day a Quality Control (QC) sample was measured as quality check at concentration 0.1-0.25-0.5-1.0 mg/l according to the concentration measured in the samples.

12.2.4. Anions (Cl^-, NO_3^-, NO_2^-)

20 ml sample was filtrated on 0.45 µm pore size filter. The anions were measured by ion chromatography from the filtrate. Spectrophotometric detector was used for the nitrite and nitrate, and conductivity detector for the chloride (from the same run, the detectors were in-line on the ion chromatograph). On every measuring day a QC sample was measured as quality check at concentration 1.0-10-20-50-100 mg/l according to the concentration measured in the samples.

12.2.5. Alkalinity (p- and m-alkalinity)

50.0 ml sample was put into a 100 ml Erlenmeyer flask and few drops of Phenolphthalein indicator solution was added. When pink colour occurred, it was titrated with 0.1 mol/l HCl until the colour disappeared. The p-alkalinity was calculated from this volume. Few drops of Bromocresol green/Methyl red indicator solution were added to the colourless solution and it was titrated with 0.1 mol/l HCl until the gendarme colour become green. The m-alkalinity was calculated from this volume. The concentration of OH^-, CO_3^{2-} and HCO_3^- was calculated from the p- and m-alkalinity.

12.2.6. Metals and trace elements and other elements measured by ICP-OES

Inductively Coupled Plasma - Optical Emission Spectrometry (ICP-OES) was applied for the quantitative analysis of major and trace elements in the water samples. A Jobin Yvon ULTIMA 2C ICP-OES was used. In radial configuration, the operation conditions were achieved with RF power of 1000W, plasma gas flow of 12 L/min, sheath gas flow of 0.2 L/min, nebulizing gas flow of 1.19 L/min, nebulizing pressure of 3 bar and observation height of 15 mm. Filtration on 0.45 µm pore size filter into a 50 ml PP centrifuge tube was used, followed acidic preservation (0.5 ml HNO_3 to 50 ml filtered sample).

Calibration solutions: In the case of the major elements, the multi-element calibration solutions were made from single element stock solutions (1000 or 10,000 mg/l) at the following concentrations for the different elements: Ca: 10 mg/L, 125 mg/L, 250 mg/L; Mg: 4 mg/L, 50 mg/L, 100 mg/L; Na: 10 mg/L, 125 mg/L, 250 mg/L; K: 2 mg/L, 25 mg/L, 50 mg/L; S: 8 mg/L, 100 mg/L, 200 mg/L; P: 0.2 mg/L, 2.5 mg/L, 5 mg/L; Si: 1 mg/L, 10 mg/L, 25 mg/L.

In the case of the trace elements (Al, As, B, Ba, Cd, Co, Cr, Cu, Mo, Ni, Li, Pb, Sr, V, Zn) the calibration solutions were made from 100 mg/l multi-element stock solution (containing 28 elements) at the concentrations: 10-100-1000 µg/l. 500 µl HNO_3 was added to 50 ml calibration blank and calibration standard solutions. 1 % HCl and 1 % HNO_3 containing rinse solution was used between the samples. If the concentration of one component exceeds the highest calibration standard, this element was measured again from sufficient dilution. The SO_4^{2-} concentration was calculated based on the measured S concentration. The H_2SiO_3 concentration was calculated based on the measured Si concentration.

For confirming the correct calibration, we measured before the first and after the last samples 500 µg/l multielement QC-sample (prepared from 10 mg/l high-purity standards stock solutions: HPS ICP-MS-68A and -68B). The results of the QC-sample should be between 450 and 550 µg/l for all of the elements. As additional quality check we measured before the water samples some samples left from previous proficiency tests. The results should be within the range 90-110 % of the assigned values.

Table S2. Measured $\delta^{13}C$, $\delta^{18}O$ and $\Delta47$ values of separated calcite (KOV-10/1 Cc). SD: standard deviation, SE: 1σ standard error, CI: confidence interval.

Rock sample	$\delta^{13}C$ [PDB, ‰]	$\delta^{18}O$ [PDB, ‰]	$\delta^{18}O$ [SMOW, ‰]	$\Delta47$ [I-CDES90°C, ‰]
KOV-10/1 cc	-1.49	-6.52	24.14	0.338
	-1.45	-6.47	24.19	0.374
	-1.48	-6.52	24.14	0.369
	-1.47	-6.52	24.14	0.392
	-1.50	-6.66	23.99	0.389
	-1.50	-6.62	24.04	0.361
	-1.57	-6.82	23.83	0.396
	-1.62	-6.94	23.71	0.375
	-1.46	-6.59	24.07	0.309
	-1.57	-6.68	23.97	0.414
	-1.53	-6.63	24.03	0.394
	-1.50	-6.59	24.07	0.396
	-1.44	-6.54	24.12	0.418
	-1.42	-6.48	24.18	0.377
Number of replicate measurements	14	14	14	14
Average	-1.50	-6.61	24.04	0.3787
±1SD	0.06	0.13	0.14	0.0289
±1SE	0.015	0.035	0.036	0.0077
95 % CI	0.032	0.076	0.079	0.0167

Table S3. Recommended grain size and reaction time for calcite-dolomite selective acid extraction in the literature. *discarded.

References	Grain size [μm]	Reaction temperature [°C]	Strength of H_3PO_4	Calcite-dolomite content	Recommendations
Epstein et al. (1964)	<75	25	100 %	50-50 %	0-1 h: calcite-CO_2 1-4 h: mixed-CO_2* 4-72 h: dolomite-CO_2
Walters et al (1972)	5-44	25	100 %	50-50 %	0-1 h: calcite-CO_2 1-3 h: mixed-CO_2* 3 h - completion: dolomite-CO_2
	0.5-5				0-7 min: calcite-CO_2 7-20 min: mixed-CO_2* 20 min - completion: dolomite-CO_2
Al-Aasm et al. (1990)	<75	25 50	100 %		0-2 h: calcite-CO_2 2-24 h: mixed CO_2* 24-28 h: dolomite-CO_2
Ray and Ramesh (1998)	37-45	25	100 %	calcite >50 % dolomite >50 %	30 min: calcite-CO_2 30 min-10 h: mixed CO_2* 10-72 h: dolomite-CO_2 15 min: calcite-CO_2 15 min-10 h: mixed-CO_2* 10-72 h: dolomite-CO_2
Yui and Gong (2003)	38-63	25	100 %		7 min: calcite-CO_2 7 min-2 h: mixed CO_2* 2-4 h: dolomite-CO_2
Baudrand et al. (2012)	50-100	40 90	100 %		20 min: calcite-CO_2 45 min bulk: isotopic mass balance calculation of dolomite
Morera-Chavarría et al. (2016)	<63 (clay-size particles were removed)	70	102 %		90 min
Liu et al. (2019)	75-80	25 50	100 %	calcite <30 % calcite >50 % calcite 30-50 %	45 min: calcite-CO_2 10-15 min: calcite-CO_2 6 min: calcite-CO_2
Du and Song (2020)	53-75	2 45	99 %		100 min: calcite-CO_2 10 h: dolomite-CO_2

Table S4. Chemical composition (CaO, MgO, MnO, FeO in %) of carbonates from Ölbő field. The composition was determined by Hitachi TM4000 Plus SEM equipped with AztecOne EDS.

Sample name	Mineral	CaO [%]	MgO[%]	MnO [%]	FeO [%]
Öl 1-8-1	dolomite	58.84	41.14	0.00	0.03
Öl 1-8-1	dolomite	59.76	40.07	0.12	0.05
Öl 1-8-1	dolomite	60.82	38.97	0.13	0.07
Öl 1-8-1	dolomite	58.83	41.06	0.00	0.11
Öl 1-8-1	dolomite	60.63	39.12	0.09	0.17
Öl 1-8-1	dolomite	59.22	40.58	0.03	0.17
Öl 1-8-1	dolomite	60.67	39.15	0.00	0.18
Öl 1-8-1	dolomite	59.41	40.41	0.00	0.18
Öl 1-8-1	dolomite	61.19	38.56	0.05	0.20
Öl 1-8-1	dolomite	59.26	40.53	0.01	0.20
Öl 1-8-1	dolomite	60.15	39.60	0.00	0.26
Öl 1-8-1	dolomite	61.47	38.25	0.00	0.28
Öl 1-8-1	dolomite	60.00	39.65	0.06	0.29
Öl 1-8-1	dolomite	61.47	38.24	0.00	0.29
Öl 1-8-1	dolomite	59.40	40.23	0.06	0.31
Öl 1-8-1	dolomite	59.13	40.55	0.00	0.32
Öl 1-8-1	dolomite	59.19	40.48	0.01	0.32
Öl 1-8-1	dolomite	59.54	40.12	0.00	0.33
Öl 1-8-1	dolomite	58.31	41.23	0.13	0.33
Öl 1-8-1	dolomite	58.74	40.84	0.00	0.42
Öl 1-8-1	dolomite	58.71	40.79	0.05	0.45
Öl 1-8-1	dolomite	58.65	40.87	0.00	0.48
Öl 1-8-1	dolomite	58.52	40.82	0.00	0.65
Öl 1-8-1	dolomite	58.80	40.50	0.04	0.66
Öl 1-8-1	dolomite	58.35	40.63	0.20	0.81
Öl 1-8-1	dolomite	58.31	40.67	0.10	0.92
Öl 1-8-1	dolomite	58.38	40.34	0.29	0.99
Öl 1-8-1	dolomite	58.61	39.91	0.47	1.01
Öl 1-8-1	dolomite	58.83	39.83	0.26	1.07
Öl 1-8-1	dolomite	60.98	37.73	0.10	1.19
Öl 1-8-1	calcite	97.39	1.03	0.16	1.43
Öl 1-8-1	calcite	97.44	0.98	0.01	1.58
Öl 1-8-1	calcite	96.94	0.95	0.23	1.88
Öl 1-8-1	calcite	96.87	0.91	0.18	2.04
Öl 1-8-1	calcite	96.78	1.10	0.05	2.07
Öl 1-8-1	calcite	96.81	1.03	0.05	2.11
Öl 1-8-1	dolomite	58.65	39.04	0.07	2.24
Öl 1-8-1	calcite	95.98	1.68	0.08	2.26
Öl 1-8-1	calcite	96.22	1.37	0.06	2.35
Öl 1-8-1	calcite	96.69	0.87	0.05	2.38
Öl 1-8-1	calcite	95.23	2.36	0.00	2.42
Öl 1-8-1	calcite	96.72	0.46	0.39	2.44
Öl 1-8-1	calcite	95.45	1.05	0.20	3.29
Öl 1-8-1	dolomite	57.61	38.27	0.34	3.78
Öl 1-8-1	dolomite	57.37	38.41	0.31	3.92
Öl 1-8-1	dolomite	55.38	40.45	0.12	4.05
Öl 1-8-1	Fe-dolomite	53.95	27.95	0.73	17.37
Öl 1-8-1	ankerite	58.38	20.49	0.29	20.84
Öl 1-8-1	ankerite	58.15	20.39	0.35	21.10
Öl 1-8-1	ankerite	58.38	19.99	0.18	21.45
Öl 1-8-1	ankerite	58.46	19.75	0.26	21.53
Öl 1-8-1	ankerite	58.17	19.90	0.28	21.65
Öl 1-8-1	ankerite	58.62	19.35	0.37	21.66
Öl 1-8-1	ankerite	57.63	20.38	0.19	21.81
Öl 1-8-1	ankerite	58.12	19.65	0.40	21.82
Öl 1-8-1	ankerite	59.22	18.54	0.30	21.94
Öl 1-8-1	ankerite	58.57	19.24	0.25	21.94
Öl 1-8-1	ankerite	58.42	19.19	0.39	22.00
Öl 1-8-1	ankerite	58.54	19.13	0.32	22.02
Öl 1-8-1	ankerite	57.82	19.84	0.32	22.02
Öl 1-8-1	ankerite	58.20	19.34	0.42	22.04
Öl 1-8-1	ankerite	58.62	18.75	0.56	22.07
Öl 1-8-1	ankerite	58.54	18.91	0.38	22.16
Öl 1-8-1	ankerite	58.19	19.14	0.39	22.28
Öl 1-8-1	ankerite	58.03	19.28	0.30	22.38
Öl 1-8-1	ankerite	58.74	18.19	0.60	22.47
Öl 1-8-1	ankerite	58.62	18.57	0.34	22.47
Öl 1-8-1	ankerite	59.02	18.12	0.28	22.57

Table S4. Continued.

Sample name	Mineral	CaO [%]	MgO[%]	MnO [%]	FeO [%]
Öl 1-8-1	ankerite	58.31	18.51	0.51	22.66
Öl 1-8-1	ankerite	58.30	18.55	0.41	22.74
Öl 1-8-1	ankerite	58.38	18.30	0.56	22.76
Öl 1-8-1	ankerite	56.59	20.38	0.25	22.78
Öl 1-8-1	ankerite	56.39	20.12	0.44	23.04
Öl 1-8-1	ankerite	57.53	18.97	0.41	23.09
Öl 1-8-1	ankerite	58.60	17.59	0.57	23.25
Öl 1-8-1	ankerite	58.10	18.16	0.49	23.26
Öl 1-8-1	ankerite	58.26	17.84	0.53	23.36
Öl 1-8-1	ankerite	55.34	20.20	0.91	23.56
Öl 1-8-1	ankerite	57.30	18.47	0.56	23.67
Öl 1-8-1	ankerite	57.84	17.93	0.51	23.73
Öl 1-8-1	ankerite	57.64	17.88	0.71	23.77
Öl 1-8-1	ankerite	57.01	18.08	0.65	24.26
Öl 1-8-1	ankerite	57.06	18.05	0.64	24.26
Öl 1-8-1	ankerite	56.38	18.64	0.65	24.33
Öl 1-8-1	ankerite	57.30	17.40	0.92	24.38
Öl 1-8-1	ankerite	56.55	18.27	0.68	24.50
Öl 1-8-1	ankerite	56.86	18.10	0.51	24.52
Öl 1-8-1	ankerite	56.33	18.04	0.69	24.95
Öl 1-8-1	ankerite	58.77	15.32	0.94	24.96
Öl 1-8-1	ankerite	55.85	18.41	0.68	25.07
Öl 1-8-1	ankerite	55.80	18.40	0.69	25.11
Öl 1-8-1	ankerite	55.56	18.93	0.36	25.15
Öl 1-8-1	ankerite	56.38	17.84	0.49	25.30
Öl 1-8-1	ankerite	55.59	18.27	0.56	25.59
Öl 1-8-1	ankerite	55.26	18.29	0.70	25.74
Öl 1-8-1	ankerite	56.30	16.41	1.08	26.21
Öl 1-8-1	ankerite	56.86	15.90	0.94	26.30
Öl 1-8-1	ankerite	56.68	16.01	0.92	26.39
Öl 1-8-1	ankerite	56.79	15.83	0.85	26.53
Öl 1-8-1	ankerite	54.78	17.82	0.73	26.67
Öl 1-8-1	ankerite	56.37	16.01	0.83	26.79
Öl 1-8-1	ankerite	55.79	16.32	0.89	27.00
Öl 1-8-1	ankerite	55.40	16.27	1.05	27.29
Öl 1-8-1	Mg-siderite	9.62	19.74	0.80	69.84
Öl 1-8-1	Mg-siderite	9.44	18.98	1.20	70.38
Öl 1-8-1	siderite	11.00	17.08	1.19	70.74
Öl 1-8-1	siderite	11.00	17.00	1.03	70.97
Öl 1-8-1	siderite	10.37	17.57	1.01	71.05
Öl 1-8-1	siderite	9.98	17.30	1.08	71.64
Öl 1-8-1	siderite	9.03	17.59	0.86	72.52
Öl 1-8-1	siderite	9.76	16.72	0.70	72.82
Öl 1-8-1	siderite	9.09	17.26	0.55	73.11
Öl 1-8-1	siderite	8.60	17.31	0.97	73.12
Öl 1-8-1	siderite	8.69	16.76	1.12	73.43
Öl 1-8-1	siderite	7.87	16.71	0.85	74.58
Öl 1-8-1	siderite	7.81	16.71	0.79	74.69
Öl 1-8-1	siderite	9.27	14.54	0.77	75.42
Öl 1-8-1	siderite	6.98	16.01	0.77	76.23
Öl 1-8-1	siderite	6.81	15.16	1.06	76.98
Öl 1-8-1	siderite	5.14	16.93	0.50	77.43
Öl 1-8-1	siderite	5.87	15.48	0.89	77.76
Öl 1-8-1	siderite	8.06	12.39	1.08	78.48
Öl 1-8-1	siderite	4.17	15.90	1.34	78.59
Öl 1-8-1	siderite	6.53	13.59	0.80	79.08
Öl 1-8-1	siderite	5.63	13.69	0.86	79.82
Öl 1-8-1	siderite	10.46	5.30	1.05	83.19
Öl 1-8-1	siderite	9.18	6.60	0.79	83.43
Öl 1-8-1	siderite	7.69	7.75	0.96	83.60
Öl 1-8-1	siderite	7.94	7.30	0.85	83.92
Öl 1-8-1	siderite	10.40	4.71	0.79	84.10
Öl 1-8-1	siderite	8.47	4.80	1.00	85.72
Öl 1-8-1	siderite	7.73	4.70	0.85	86.71
Öl 1-8-1	siderite	7.79	4.71	0.75	86.75
Öl 1-8-1	siderite	6.51	6.08	0.56	86.84
Öl 1-8-1	siderite	6.15	5.61	0.50	87.74
Öl 1-8-1	siderite	7.77	3.09	1.14	88.00
Öl 1-8-1	siderite	5.51	5.11	0.63	88.76
Öl 1-8-1	siderite	4.67	4.70	0.49	90.14

Table S4. Continued.

Sample name	Mineral	CaO [%]	MgO[%]	MnO [%]	FeO [%]
Öl 1-8-1	siderite	4.04	3.97	0.76	91.23
Öl 1-8-1	siderite	4.48	1.32	0.57	93.64
Öl 1-9B1	dolomite	60.32	39.64	0.03	0.01
Öl 1-9B1	dolomite	59.58	40.31	0.00	0.11
Öl 1-9B1	dolomite	59.58	40.24	0.03	0.15
Öl 1-9B1	dolomite	60.85	38.87	0.12	0.16
Öl 1-9B1	dolomite	59.78	39.91	0.13	0.19
Öl 1-9B1	dolomite	60.33	39.43	0.01	0.23
Öl 1-9B1	dolomite	60.91	38.80	0.04	0.25
Öl 1-9B1	dolomite	61.38	38.38	0.00	0.25
Öl 1-9B1	dolomite	59.52	40.22	0.00	0.26
Öl 1-9B1	dolomite	60.39	39.28	0.00	0.32
Öl 1-9B1	calcite	99.36	0.31	0.01	0.32
Öl 1-9B1	dolomite	59.96	39.70	0.00	0.33
Öl 1-9B1	calcite	99.25	0.42	0.00	0.33
Öl 1-9B1	dolomite	59.68	39.80	0.17	0.35
Öl 1-9B1	dolomite	60.64	39.00	0.00	0.36
Öl 1-9B1	dolomite	60.62	39.01	0.00	0.36
Öl 1-9B1	dolomite	60.74	38.85	0.00	0.41
Öl 1-9B1	dolomite	59.84	39.64	0.09	0.42
Öl 1-9B1	dolomite	60.96	38.52	0.08	0.43
Öl 1-9B1	dolomite	59.55	39.94	0.06	0.45
Öl 1-9B1	calcite	99.07	0.33	0.16	0.45
Öl 1-9B1	dolomite	59.60	39.93	0.00	0.47
Öl 1-9B1	dolomite	60.23	39.22	0.00	0.56
Öl 1-9B1	dolomite	59.95	39.17	0.04	0.83
Öl 1-9B1	calcite	96.54	2.63	0.00	0.83
Öl 1-9B1	calcite	96.07	2.93	0.06	0.94
Öl 1-9B1	calcite	98.07	0.72	0.22	0.99
Öl 1-9B1	calcite	96.68	0.70	1.44	1.19
Öl 1-9B1	calcite	96.29	2.16	0.20	1.35
Öl 1-9B1	calcite	95.78	2.55	0.29	1.38
Öl 1-9B1	dolomite	61.29	37.29	0.00	1.42
Öl 1-9B1	calcite	96.20	2.22	0.16	1.42
Öl 1-9B1	calcite	95.12	2.94	0.35	1.59
Öl 1-9B1	calcite	93.73	0.81	3.84	1.62
Öl 1-9B1	dolomite	58.43	39.87	0.00	1.71
Öl 1-9B1	calcite	96.92	1.07	0.13	1.88
Öl 1-9B1	calcite	95.33	2.42	0.32	1.93
Öl 1-9B1	dolomite	58.53	39.42	0.00	2.05
Öl 1-9B1	dolomite	58.21	39.72	0.00	2.07
Öl 1-9B1	dolomite	58.18	39.67	0.05	2.10
Öl 1-9B1	dolomite	58.64	38.94	0.17	2.24
Öl 1-9B1	calcite	94.35	3.29	0.00	2.36
Öl 1-9B1	calcite	94.41	3.09	0.03	2.47
Öl 1-9B1	calcite	94.10	1.65	1.18	3.07
Öl 1-9B1	calcite	92.98	3.52	0.16	3.35
Öl 1-9B1	calcite	93.07	3.36	0.15	3.42
Öl 1-9B1	dolomite	58.86	37.02	0.00	4.11
Öl 1-9B1	Fe-calcite	89.56	3.01	3.16	4.27
Öl 1-9B1	Fe-calcite	89.57	2.90	3.03	4.50
Öl 1-9B1	dolomite	56.35	35.47	2.53	5.65
Öl 1-9B1	Fe-calcite	83.41	1.81	0.95	13.84
Öl 1-9B1	Fe-dolomite	52.06	28.26	0.96	18.72
Öl 1-9B1	Fe-dolomite	52.30	27.58	1.12	19.00
Öl 1-9B1	ankerite	60.04	20.52	0.44	19.00
Öl 1-9B1	ankerite	52.61	27.94	0.30	19.15
Öl 1-9B1	ankerite	59.42	20.70	0.57	19.31
Öl 1-9B1	ankerite	59.19	20.63	0.67	19.51
Öl 1-9B1	ankerite	59.81	19.54	0.48	20.17
Öl 1-9B1	ankerite	59.63	19.66	0.51	20.21
Öl 1-9B1	ankerite	59.86	19.34	0.42	20.38
Öl 1-9B1	ankerite	59.39	19.45	0.55	20.61
Öl 1-9B1	ankerite	58.59	20.16	0.58	20.67
Öl 1-9B1	ankerite	58.80	19.56	0.66	20.97
Öl 1-9B1	ankerite	58.88	19.50	0.62	20.99
Öl 1-9B1	ankerite	58.83	19.55	0.59	21.04
Öl 1-9B1	ankerite	59.19	19.16	0.57	21.09
Öl 1-9B1	ankerite	58.79	19.57	0.38	21.26
Öl 1-9B1	ankerite	58.92	19.31	0.40	21.37

Table S4. Continued.

Sample name	Mineral	CaO [%]	MgO[%]	MnO [%]	FeO [%]
Öl 1-9B1	ankerite	59.02	19.25	0.36	21.38
Öl 1-9B1	ankerite	59.02	19.25	0.36	21.38
Öl 1-9B1	ankerite	55.04	22.51	0.95	21.50
Öl 1-9B1	ankerite	60.04	17.93	0.43	21.59
Öl 1-9B1	ankerite	59.09	18.44	0.65	21.82
Öl 1-9B1	ankerite	57.40	19.97	0.72	21.91
Öl 1-9B1	ankerite	56.52	20.94	0.56	21.98
Öl 1-9B1	ankerite	57.71	19.78	0.51	22.00
Öl 1-9B1	ankerite	55.16	22.22	0.41	22.21
Öl 1-9B1	ankerite	56.88	20.48	0.42	22.22
Öl 1-9B1	ankerite	57.61	19.28	0.59	22.52
Öl 1-9B1	ankerite	56.87	20.02	0.51	22.60
Öl 1-9B1	ankerite	57.79	18.83	0.73	22.65
Öl 1-9B1	ankerite	54.65	21.83	0.72	22.80
Öl 1-9B1	ankerite	56.25	18.17	2.47	23.10
Öl 1-9B1	ankerite	56.65	19.26	0.90	23.19
Öl 1-9B1	ankerite	56.92	19.05	0.74	23.29
Öl 1-9B1	ankerite	56.81	18.78	0.68	23.73
Öl 1-9B1	ankerite	55.22	20.08	0.69	24.01
Öl 1-9B1	ankerite	55.83	19.65	0.50	24.02
Öl 1-9B1	ankerite	56.67	17.97	0.66	24.70
Öl 1-9B1	ankerite	56.13	18.29	0.66	24.91
Öl 1-9B1	ankerite	56.51	17.55	0.99	24.95
Öl 1-9B1	ankerite	55.49	18.65	0.60	25.26
Öl 1-9B1	ankerite	55.70	18.17	0.85	25.27
Öl 1-9B1	ankerite	56.48	17.37	0.88	25.27
Öl 1-9B1	ankerite	54.82	17.93	1.02	26.24
Öl 1-9B1	ankerite	55.38	16.34	1.28	27.01
Öl 1-9B1	ankerite	53.71	16.67	1.20	28.42
Öl 1-9B1	Mg-siderite	13.98	20.47	0.77	64.78
Öl 1-9B1	Mg-siderite	13.25	20.64	0.87	65.24
Öl 1-9B1	siderite	6.17	16.79	1.28	75.76
Öl 1-9B1	siderite	6.00	16.17	1.48	76.35
Öl 1-9B1	siderite	5.28	15.84	1.44	77.45
Öl 1-9B1	siderite	4.91	15.63	1.65	77.81
Öl 1-9B1	siderite	6.62	13.99	1.24	78.15
Öl 1-9B1	siderite	3.40	14.94	1.69	79.98
Öl 1-9B1	siderite	5.07	12.76	1.10	81.07
Öl 1-9B1	siderite	2.86	14.00	1.45	81.70
Öl 1-9B1	siderite	2.45	13.85	1.59	82.10
Öl 1-9B1	siderite	3.26	12.97	1.64	82.13
Öl 1-9B1	siderite	3.32	12.20	0.98	83.50
Öl 1-9B1	siderite	5.68	9.37	1.04	83.91
Öl 1-9B1	siderite	5.14	9.49	1.46	83.91
Öl 1-9B1	siderite	3.94	10.72	1.01	84.32
Öl 1-9B1	siderite	5.02	9.40	0.97	84.60
Öl 1-9B1	siderite	4.33	9.45	1.13	85.09
Öl 1-9B1	siderite	7.71	6.63	0.52	85.15
Öl 1-9B1	siderite	3.11	10.31	1.38	85.21
Öl 1-9B1	siderite	3.23	8.99	1.28	86.49
Öl 1-9B1	siderite	4.95	7.36	1.07	86.61
Öl 1-9B1	siderite	5.49	6.66	1.07	86.78
Öl 1-9B1	siderite	4.30	7.68	0.91	87.11
Öl 1-9B1	siderite	2.91	8.12	1.21	87.76
Öl 1-9B1	siderite	2.58	8.07	0.93	88.42
Öl 1-9B1	siderite	3.02	7.20	1.33	88.45
Öl 1-9B1	siderite	3.89	6.10	0.98	89.03
Öl 1-9B1	siderite	3.59	6.21	1.16	89.04
Öl 1-9B1	siderite	5.28	4.47	0.73	89.53
Öl 1-9B1	siderite	2.99	6.07	1.37	89.57
Öl 3-5-1	dolomite	61.01	38.84	0.06	0.09
Öl 3-5-1	dolomite	62.58	37.20	0.01	0.21
Öl 3-5-1	dolomite	63.78	35.96	0.04	0.22
Öl 3-5-1	dolomite	59.88	39.77	0.00	0.36
Öl 3-5-1	dolomite	59.82	39.77	0.00	0.41
Öl 3-5-1	dolomite	60.49	38.98	0.10	0.43
Öl 3-5-1	dolomite	60.85	38.59	0.08	0.48
Öl 3-5-1	dolomite	61.33	38.15	0.00	0.52
Öl 3-5-1	dolomite	61.07	38.41	0.00	0.52
Öl 3-5-1	dolomite	64.78	34.57	0.04	0.60

Table S4. Continued.

Sample name	Mineral	CaO [%]	MgO[%]	MnO [%]	FeO [%]
Öl 3-5-1	dolomite	59.93	39.34	0.10	0.63
Öl 3-5-1	dolomite	60.22	38.98	0.10	0.70
Öl 3-5-1	dolomite	60.84	38.32	0.09	0.75
Öl 3-5-1	dolomite	60.15	38.91	0.04	0.90
Öl 3-5-1	Fe-dolomite	56.05	30.74	0.29	12.93
Öl 3-5-1	Fe-dolomite	55.06	31.29	0.31	13.34
Öl 3-5-1	Fe-dolomite	54.84	31.21	0.25	13.69
Öl 3-5-1	Fe-dolomite	55.24	30.28	0.49	13.99
Öl 3-5-1	ankerite	59.36	18.88	0.40	21.36
Öl 3-5-1	ankerite	58.15	20.23	0.21	21.41
Öl 3-5-1	ankerite	57.41	20.70	0.45	21.44
Öl 3-5-1	ankerite	58.77	19.31	0.45	21.47
Öl 3-5-1	ankerite	58.78	19.30	0.40	21.51
Öl 3-5-1	ankerite	57.09	20.97	0.36	21.58
Öl 3-5-1	ankerite	57.69	20.27	0.45	21.59
Öl 3-5-1	ankerite	58.93	19.14	0.35	21.59
Öl 3-5-1	ankerite	58.67	19.47	0.25	21.62
Öl 3-5-1	ankerite	58.42	19.60	0.33	21.65
Öl 3-5-1	ankerite	59.18	18.64	0.48	21.70
Öl 3-5-1	ankerite	58.13	19.81	0.32	21.74
Öl 3-5-1	ankerite	58.85	18.94	0.39	21.81
Öl 3-5-1	ankerite	58.64	18.80	0.48	22.08
Öl 3-5-1	ankerite	58.22	18.92	0.65	22.20
Öl 3-5-1	ankerite	58.19	19.22	0.37	22.23
Öl 3-5-1	ankerite	58.46	18.87	0.32	22.35
Öl 3-5-1	ankerite	57.51	19.60	0.40	22.49
Öl 3-5-1	ankerite	56.10	20.82	0.42	22.66
Öl 3-5-1	ankerite	56.38	20.29	0.38	22.95
Öl 3-5-1	ankerite	58.30	18.18	0.33	23.18
Öl 3-5-1	ankerite	54.98	20.99	0.53	23.50
Öl 3-5-1	ankerite	56.79	19.02	0.63	23.56
Öl 3-5-1	ankerite	56.53	18.43	0.67	24.37
Öl 3-5-1	ankerite	56.87	18.29	0.39	24.45
Öl 3-5-1	ankerite	50.71	23.10	0.74	25.45
Öl 3-5-1	ankerite	50.69	22.67	0.63	26.02
Öl 3-5-1	ankerite	50.18	22.91	0.76	26.15
Öl 3-5-1	ankerite	50.52	21.94	0.76	26.79
Öl 3-5-1	ankerite	53.87	18.20	0.80	27.13
Öl 3-5-1	ankerite	54.32	17.72	0.78	27.18
Öl 3-5-1	ankerite	50.58	21.64	0.58	27.19
Öl 3-5-1	ankerite	54.45	17.36	0.98	27.22
Öl 3-5-1	ankerite	55.00	16.86	0.87	27.27
Öl 3-5-1	ankerite	54.15	17.54	0.98	27.33
Öl 3-5-1	ankerite	53.45	18.18	0.69	27.68
Öl 3-5-1	ankerite	52.96	18.34	0.88	27.82
Öl 3-5-1	ankerite	53.50	17.69	0.72	28.09
Öl 3-5-1	ankerite	52.97	18.14	0.66	28.23
Öl 3-5-1	ankerite	53.18	17.99	0.54	28.30
Öl 3-5-1	ankerite	52.86	18.13	0.62	28.40
Öl 3-5-1	ankerite	54.04	16.55	0.84	28.57
Öl 3-5-1	ankerite	52.68	18.08	0.66	28.58
Öl 3-5-1	ankerite	53.68	16.96	0.75	28.61
Öl 3-5-1	ankerite	54.46	16.18	0.74	28.62
Öl 3-5-1	ankerite	53.74	16.73	0.84	28.69
Öl 3-5-1	ankerite	53.98	16.54	0.64	28.84
Öl 3-5-1	ankerite	53.21	17.30	0.64	28.86
Öl 3-5-1	ankerite	54.02	16.31	0.68	28.99
Öl 3-5-1	ankerite	53.45	16.62	0.86	29.07
Öl 3-5-1	ankerite	52.15	18.02	0.74	29.09
Öl 3-5-1	ankerite	53.58	16.68	0.54	29.21
Öl 3-5-1	ankerite	53.88	16.00	0.82	29.30
Öl 3-5-1	ankerite	53.26	16.58	0.83	29.32
Öl 3-5-1	ankerite	53.71	16.15	0.80	29.33
Öl 3-5-1	ankerite	53.19	16.68	0.70	29.43
Öl 3-5-1	ankerite	53.19	16.67	0.69	29.44
Öl 3-5-1	ankerite	52.76	16.97	0.81	29.46
Öl 3-5-1	ankerite	53.35	16.43	0.74	29.49
Öl 3-5-1	ankerite	53.28	16.43	0.74	29.55
Öl 3-5-1	ankerite	53.57	16.10	0.71	29.62
Öl 3-5-1	ankerite	53.54	16.07	0.58	29.80

Table S4. Continued.

Sample name	Mineral	CaO [%]	MgO[%]	MnO [%]	FeO [%]
Öl 3-5-1	ankerite	52.54	16.85	0.66	29.95
Öl 3-5-1	ankerite	52.78	16.53	0.70	30.00
Öl 3-5-1	ankerite	53.43	15.51	0.75	30.30
Öl 3-5-1	ankerite	53.21	14.09	1.59	31.11
Öl 3-5-1	ankerite	51.30	16.40	0.61	31.69
Öl 3-5-1	siderite	0.91	21.39	1.41	76.28
Öl 3-5-1	siderite	0.51	20.48	1.33	77.68
Öl 3-5-1	siderite	2.75	15.05	1.02	81.18
Öl 3-5-1	siderite	1.74	14.15	1.11	83.00
Öl 3-5-1	siderite	4.12	8.21	1.00	86.66
Öl 3-5-1	siderite	5.29	3.10	1.03	90.58
Öl 3-5-1	siderite	4.44	3.45	0.78	91.33

Equation S1.

Calculation of $\delta^{13}C$ values of CO_2 from the carbon isotope composition of dawsonite using calcite-CO_2 fractionation equations by Ohmoto & Rye (1979) where T=K:

$$1000ln\frac{1000+\delta\,(\text{calcite})}{1000+\delta\,(CO_2)} = \frac{(-8.914*10^8)}{T^3} + \frac{(8.557*10^6)}{T^2} - \frac{(18.11*10^3)}{T} + 8.24$$

Equation S2.

Calculation of $\delta^{13}C$ values of CO_2 from the carbon isotope composition of dawsonite using calcite-CO_2 fractionation equations by Bottinga (1968) where T=K:

$$1000ln\frac{1000+\delta\,(CO_2)}{1000+\delta\,(\text{calcite})} = \frac{(-2.988*10^6)}{T^2} + \frac{(7.666*10^3)}{T} - 2.461$$

Equation S3.

Calculation of $\delta^{13}C$ values of CO_2 from the carbon isotope composition of siderite using the siderite-CO_2 fractionation equation by Golyshev et al. (1981) where T=K:

$$1000ln\frac{1000+\delta\,(\text{siderite})}{1000+\delta\,(CO_2)} = \frac{(0.0771*10^{18})}{T^6} + \frac{(-5.8544*10^{12})}{T^4} + \frac{(31.8155*10^9)}{T^3} + \frac{(-63.556*10^6)}{T^2} + \frac{(51.467*10^3)}{T} - 12.360$$

Equation S4.

Calculation of δD values of H_2O from the hydrogen isotope composition of dawsonite using gibbsite-H_2O fractionation equation by Méheut et al. (2010) where T=K:

$$1000\,ln\frac{1000+\delta\,(gibbsite)}{1000+\delta\,(H_2O)} = \frac{(25.550*10^6)}{T^2} + \frac{(-34.250*10^3)}{T} - 51.700$$

Equation S5.

Calculation of $\delta^{18}O$ values of CO_2 from the oxygen isotope composition of dawsonite using calcite-H_2O fractionation equations by O'Neil et al. (1969) where T=K:

$$1000ln\frac{1000 + \delta\,(\text{calcite})}{1000 + \delta\,(\text{H}_2\text{O})} = \frac{(2.78 * 10^6)}{T^2} - 2.89$$

Table S5. Covasna well waters physical and chemical compositions (Georgescu, 1976). NM: not measured.

	Unit	F1 Oana	F2 Diana	F3 Anca	F5 Gabriela	F6 Minerva	F7 Isabela	F17
Air temperature	°C	28	29	29	31	31	15	NM
Water temperature	°C	14	13	14	9	11.5	11	NM
pH		6.4	7.3	6.3	7.4	6.5	7.5	6.55
EC	µS/cm	541	3978	758	3780	3016	8046	NM
Na^+	mg/L	100.92	1115.89	121.582	1029.75	769.399	2628.2	1881.2
K^+	mg/L	8.4	50.1	15.7	13	61	1578.8	101.8
Ca^{2+}	mg/L	54.1	96.2	109	183.3	108.2	109	96.2
Mg^{2+}	mg/L	7.3	131.3	15	144.8	63.2	37.9	77.3
NH^{4+}	mg/L	0.5	7.5	5	3.5	5	NM	3
Cl^-	mg/L	4.25	638.3	156.0	971.6	581.5	1312	1160
HCO_3^-	mg/L	396.5	3050	488	2257	1830	7654	3843
SO_4^{2-}	mg/L	42	20.1	45.7	8.2	25.6	124.8	12.3